LUMINESCENT PROPERTIES OF COMBUSTION SYNTHESIZED BaAl$_2$O$_4$:Eu^{2+} AND (Ba$_{1-x}$Sr$_x$)Al$_2$O$_4$:Eu^{2+} PHOSPHORS CO-DOPED WITH DIFFERENT RARE EARTH IONS

By

Lephoto Mantwa Annah

(**BSc Hons**)

A dissertation presented in fulfillment of the requirements for the degree

MAGISTER SCIENTIAE

in the

Faculty of Natural and Agricultural Sciences

Department of Physics

at the

University of the Free State

Republic of South Africa

Supervisors: Prof. O.M. Ntwaeaborwa

Dr. B.M. Mothudi

Co-supervisor: Prof. H.C. Swart

UNIVERSITY OF THE
FREE STATE
UNIVERSITEIT VAN DIE
VRYSTAAT
YUNIVESITHI YA
FREISTATA

UFS
UV

November 2011

Dedicated to my son

Lephoto Sibusiso Oratilwe Ndabezitha

Born: 08 November 2011

Acknowledgements

I would like to give thanks to God Almighty for making it all possible for me to complete this study.

All thanks to people who assisted me during the course of this study, without them this would not have been possible.

ABSTRACT

A Combustion method was used to prepare all the alkaline earth aluminates (rare-earths doped $BaAl_2O_4$, $BaSrAl_2O_4$ and $BaZnAl_2O_4$) phosphor powders in this study. Measurements of these phosphor powders were carried out using various characterization techniques such as X-ray diffraction (XRD), Scanning Electron Microcopy (SEM), X-ray energy dispersive spectroscopy (EDS), X-ray Photoelectron Spectroscopy (XPS) and Fourier Transform Infrared Spectroscopy (FT-IR). The XRD data were collected using a D8 advance powder X-ray diffractometer with CuKα radiation. Morphology and elemental composition were done using JEOL- JSM 7500F Scanning Electron Microscope. The stretching mode frequencies data were collected using Perkin Elmer Spectrum 100 FTIR spectrometer and the elemental composition on the surfaces of the phosphor powders were monitored by the PHI 5400 Versaprobe scanning X-ray photoelectron spectrometer. Photoluminescence (PL) data were collected using 325nm He-Cd laser and decay data were collected using Varian Cary Eclipse Fluorescence Spectrophotometer coupled with a monochromatized Xenon lamp (60-75 W) as excitation source and measurements were carried out in air at room temperature. The thermoluminescence (TL) data were collected using a Thermoluminescence Reader (Integral-Pc Based) Nucleonix TL 1009I.

$BaAl_2O_4$:Eu^{2+} phosphor powders co-doped with different trivalent rare-earth (RE= Dy^{3+}, Nd^{3+}, Gd^{3+}, Sm^{3+}, Ce^{3+}, Er^{3+}, Pr^{3+} and Tb^{3+}) ions were prepared at an initiating temperature of $600^{o}C$ and annealed at $1000^{o}C$ for 3 hours. The X-ray diffraction (XRD) data shows hexagonal structure of $BaAl_2O_4$ for both as prepared and post annealed samples. All samples exhibited bluish-green emission associated with the $4f^65d^1 \rightarrow 4f^7$ transitions of Eu^{2+} at ~504 nm. The longest afterglow was observed from the $BaAl_2O_4$:Eu^{2+} co-doped with Nd^{3+}.

$BaAl_2O_4$:Eu^{2+}, Nd^{3+}, Gd^{3+} phosphor powders were prepared at different initiating temperatures of $400-1200^{o}C$. X-ray diffraction data show the formation of the hexagonal $BaAl_2O_4$ structure at the temperatures of $500^{o}C$-$1200^{o}C$. The crystal size calculated from the phosphor powder prepared at $1200^{o}C$ was found to be 63 nm. Blue-green photoluminescence with persistent/long afterglow, was observed at 502 nm and the highest PL intensity was observed from the sample prepared at $600^{o}C$. The phosphorescence decay curves showed that the rate of decay was faster in the case of the sample prepared at $600^{o}C$ compared to that prepared at $1200^{o}C$. The TL glow

peaks of the samples prepared at 600°C and 1200°C were both stable at ~72°C suggesting that the traps responsible for the long afterglow were not affected by the temperature.

Barium-substituted phosphor powders of $(Ba_{1-x}Sr_x)Al_2O_4:Eu^{2+};Nd^{3+}$ composition were prepared at an initiating temperature of 500°C. The X-ray diffraction with the composition of x = 0 shows the hexagonal phase of $BaAl_2O_4$ and the one for x = 1 shows the monoclinic phase of $SrAl_2O_4$. The XRD with the composition of x = 0.4, 0.5 and 0.6 shows the admixture of $BaAl_2O_4$ and $SrAl_2O_4$ structures. SEM investigations showed some changes on the surface morphology for different compositions. Photoluminescence (PL) studies showed the $(Ba_{1-x}Sr_x)Al_2O_4:Eu^{2+};Nd^{3+}$ (x = 0) and $(Ba_{1-x}Sr_x)Al_2O_4:Eu^{2+};Nd^{3+}$ (x = 1) with blue-green to bright-green emissions with peaks at 505 nm and 520 nm respectively. The mixed composition with x = 0.4, 0.5 and 0.6 showed two peaks at 447 nm and 517 nm. Phosphorescence showed higher luminescence for $(Ba_{1-x}Sr_x)Al_2O_4:Eu^{2+};Nd^{3+}$ at (x = 0) compared to other compositions.

$(Ba_{1-x}Zn_x)Al_2O_4:Eu^{2+};Nd^{3+}$ phosphor powders with the compositions x = 0.2, 0.4, 0.5, 0.6, 0.8 and 1 were prepared at an initiating temperature of 500°C. The X-ray diffraction showed the cubic structure for the compositions of x = 0 and x = 1. The SEM images of the phosphor samples showed different kinds of morphologies for the compositions x = 0, 0.5 and 1. The PL emission of the phosphor powder clearly showed a shift from green to blue regions. The highest PL emission and the long afterglow ascribed to trapping and detrapping of charge carriers were observed from $(Ba_{1-x}Zn_x)Al_2O_4:Eu^{2+};Nd^{3+}$ with x = 0.2.

KEYWORDS: Combustion method, Photoluminescence, Thermoluminescence, Long afterglow, Alkaline earth aluminates and Rare earth ions.

ACRONYMS:

- EDS -Energy dispersive spectroscopy
- He- Cd -Helium Cadmium Laser
- PL - Photoluminescence
- SEM- Scanning Electron Microcopy
- TL- Thermoluminescence
- XRD - X-ray Diffraction
- XPS - X-ray photoelectron spectroscopy

TABLE OF CONTENTS

CHAPTER 1: PHOSPHORS

CHAPTER 2: SYNTHESIS AND CHARACTERIZATION TECHNIQUES

CHAPTER 3: SYNTHESIS AND CHARACTERIZATION OF $BaAl_2O_4:Eu^{2+}$ CO-DOPED WITH DIFFERENT RARE EARTH IONS

CHAPTER 4: EFFECT OF THE INITIATING TEMPERATURE ON THE STRUCTURAL AND LUMINESCENT PROPERTIES OF $BaAl_2O_4:Eu^{2+};Nd^{3+};Gd^{3+}$

CHAPTER 5: SYNTHESIS AND PHOTOLUMINESCENCE STUDIES OF $(Ba_{1-x}Sr_x)Al_2O_4:Eu^{2+};Nd^{3+}$ PREPARED BY COMBUSTION METHOD

CHAPTER 6: Effects of Ba^{2+} and Zn^{2+} concentrations on the structure and luminescent properties of $(Ba_{1-x}Zn_x)Al_2O_4:Eu^{2+};Nd^{3+}$

CHAPTER 7: Summary and conclusions

LIST OF FIGURES

8

LIST OF TABLES

CHAPTER 1

PHOSPHORS

Introduction

This chapter is about the historical background of phosphors. It also gives an understanding of different luminescence processes and the mechanism behind the long afterglow phosphors is explained in details. Applications of phosphorescence materials are also given with their examples.

1.1 Historical background

The word phosphor comes from the Greek language and it means light bearer [1]. A phosphor can be defined as any material that emits light when exposed to an external excitation source. The source can include photons, electrons, x-rays, etc. The phosphor materials can either be in powder or thin film forms. Phosphors are mostly solid inorganic materials consisting of a host lattice, usually intentionally doped with impurities. The impurity concentrations are generally low due to the fact that at higher concentrations the efficiency of their luminescence emission usually decreases (due to concentration quenching effects) [3]. Either the host or the activator can determine the luminescent properties of a phosphor. For example, in Zinc sulphide/ Cadmium sulphide: silver (ZnS: Ag/ CdS: Ag) the emitted colours range from blue at zero cadmium through green, to yellow and into red as the CdS content is increased [1].

A phosphor is usually identified by its chemical formula, e.g. $MAl_2O_4:Eu^{2+}$ (M= Ba, Ca, Sr), where MAl_2O_4 is the host matrix and Eu^{2+} is the activator. If more than one activator is used, commas are used to separate them (e.g. $MAl_2O_4:Eu^{2+}, Nd^{3+}, Dy^{3+}$), and these additional activators (Nd^{3+} and Dy^{3+}) are called co-activators. These types of phosphors are called the

alkaline earth aluminate phosphors and they are well studied recently because of their high quantum efficiency in the visible region [4]. In these types of phosphors, the Eu^{2+} ion is the luminescent center and the Re^{3+} ions (Nd^{3+}, Dy^{3+}, etc…) are charge carriers (holes and electrons) traps [5].

ZnS: Cu was a well-studied long afterglow phosphor for nearly a century. The emission from this phosphor is not bright enough and the afterglow is not sustained for more than few hours. Its afterglow can only be improved by the addition of radioisotopes such as tritium and promethium. However, addition of radioisotopes is environmentally unsafe and this made it necessary to find alternative afterglow phosphors that do not need radioisotopes and with better optical properties than ZnS: Cu [6].

MAl_2O_4:Eu^{2+}; Dy^{3+} (M= Ca, Sr, Ba) phosphors were found to be the potential materials with persistent phosphorescent to replace ZnS:Cu based phosphors. Compared to ZnS:Cu, MAl_2O_4:Eu^{2+}; Dy^{3+} (M= Ca, Sr, Ba) phosphors are safe, chemically stable and they exhibit good photoluminescent properties without addition of radioactive isotopes [7, 8]. Their luminescence is characterized by a rapid decay from the Eu^{2+} ion followed by a long afterglow due to the Dy^{3+} or other trivalent rare-earth ions which acts as auxiliary activator [9]. The Eu^{2+} doped solid state material usually shows strong broad band luminescence with a short decay time, of the order of some tens of nanoseconds. The characteristic broad band luminescence originates from transition between $^8S_{7/2}$ (4f) ground state and the crystal field components of the $4f^65d^1$ excited state configuration [10]. Since it is said that there are different alkaline earth aluminates, in this study the main focus was on $BaAl_2O_4$.

1.2 Long Persistence Phosphors

Long persistent phosphors are phosphors that have very long afterglow emission or phosphorescence. In some cases, their phosphorescence can even last for days. Afterglow is caused by trapped electrons or holes produced during the excitation. Long persistent (phosphorescent) phosphors are also called long lasting or long afterglow phosphors. The mechanism of long persistent phosphorescence can be explained in terms of three level energy diagrams including a ground state, an excited state and a metastable trapping state for the active electron [11]. In persistence luminescence, the electrons/holes can be released from the traps at

near room temperature. In the simplest model, electrons and holes are distributed evenly in the matrix and the distance between the different charge carriers is rather long [12].

There are different mechanisms proposed to explain persistence luminescence, but recently, the most accepted mechanism is on electron trapping. This mechanism considers that (i) under irradiation of the material some electrons escape from the $4f^6 5d^1$ levels of Eu^{2+} to the conduction band, (ii) some of these electrons are trapped from the conduction band to defects such as oxygen vacancies, and possibly to the R^{3+} co-dopant, too and (iii) the reverse process of freeing the electrons from the traps to the $4f^6 5d^1$ levels of Eu^{2+} via the conduction band precedes the radiative relaxation of the electron back to the $4f^7$ ($^8S_{7/2}$) ground state of Eu^{2+} and the generation of the persistent luminescence [10]. Shown in figure 1.1, is the schematic diagram of the proposed mechanism similar to that explained by Claubau et al [13]. This mechanism involves the electron capture by traps and a subsequent thermally induced detrapping of the electron resulting in persistent emission of photons (long afterglow luminescence/phosphorescent luminescence).
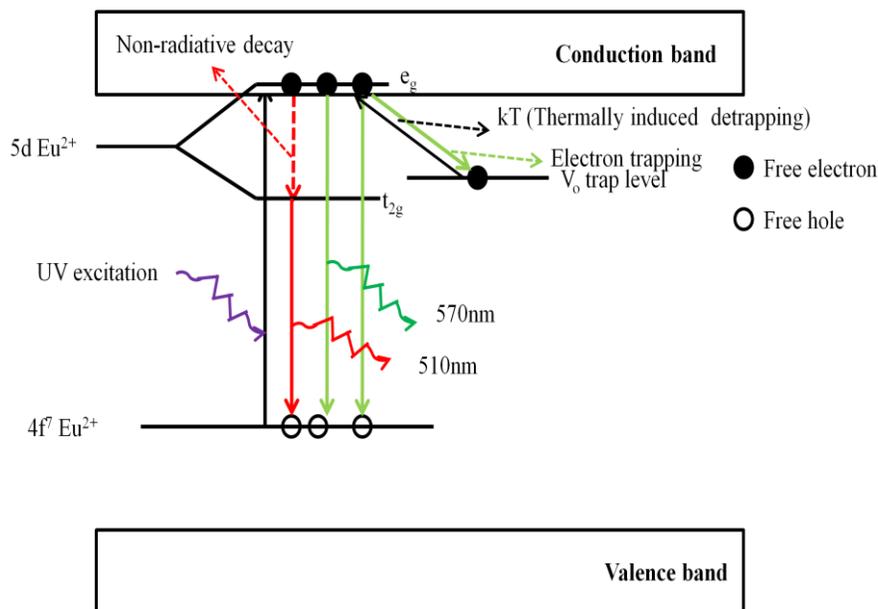
Figure 1.1: Possible phosphorescence mechanism.

The alkaline earth aluminates can be used as an example for the long persistence phosphors. $CaAl_2O_4:Eu^{2+}$, Nd^{3+}, $SrAl_2O_4:Eu^{2+}$, Dy^{3+} and $BaAl_2O_4:Eu^{2+}$, Dy^{3+} are considered to be the useful blue and green phosphors by their long phosphorescence characteristics [14]. Katsumata et al[15] reported that the mechanism of their prolonged phosphorescence from Eu^{2+} is based on the hole trapping due to the $Nd^{3+}$and/or Dy^{3+} ions whose trap level(s) are/is deep enough to release trapped holes thermally. Shown in figure 1.2 is the schematic diagram to show the long persistence of $CaAl_2O_4:Eu^{2+}$, Nd^{3+} phosphor.
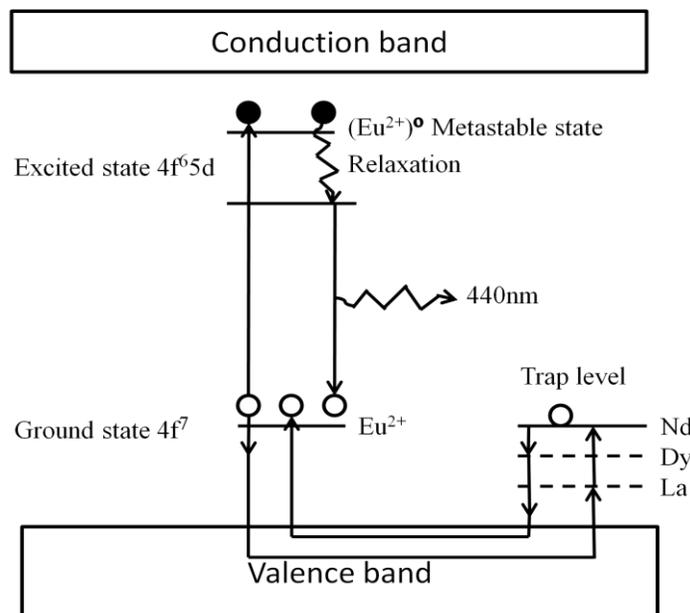
Figure 1.2: Proposed mechanism of long afterglow photoluminescence of CaAl₂O₄-based phosphors [16].

The mechanism shown in figure 1.2 can be interpreted based on hole trapping. When Eu^{2+} ions are excited by lights, the direct excitation of Eu^{2+} due to 4f $\rightarrow$ 4f5d transition occurs, and a great deal of holes are generated. Some free holes are released thermally to the valence band, and some of the released holes are trapped by the co-doped rare earth ions. When the excitation source is removed, the trapped holes are released thermally to the valence band, and the holes migrate and recombine with some of free electrons, which lead to the long afterglow [16].

13

1.3 Luminescence processes

Light is a form of energy. There are two principal processes, which can cause the emission of light, namely incandescent and luminescence. Incandescent is defined as the light from heat energy, which means heating an object to such a high temperature that the atoms become highly agitated leading to the glowing of the body [17]. Luminescence can be defined as the luminous emission which is not thermal in origin i.e. luminescence is "cold light", from sources of energy, which takes place at normal and lower temperature [18]. In luminescence process, usually incident excitation energy is absorbed, causing an electron to jump from its ground state to a higher, excited energy state. Around 10^{-8} seconds later, the electron returns to the ground state resulting in emission of a photon with different wavelength from that of the incident photon. This return to the ground state also results in an excited vibrational state and reaches equilibrium in about 10^{-12} [19].
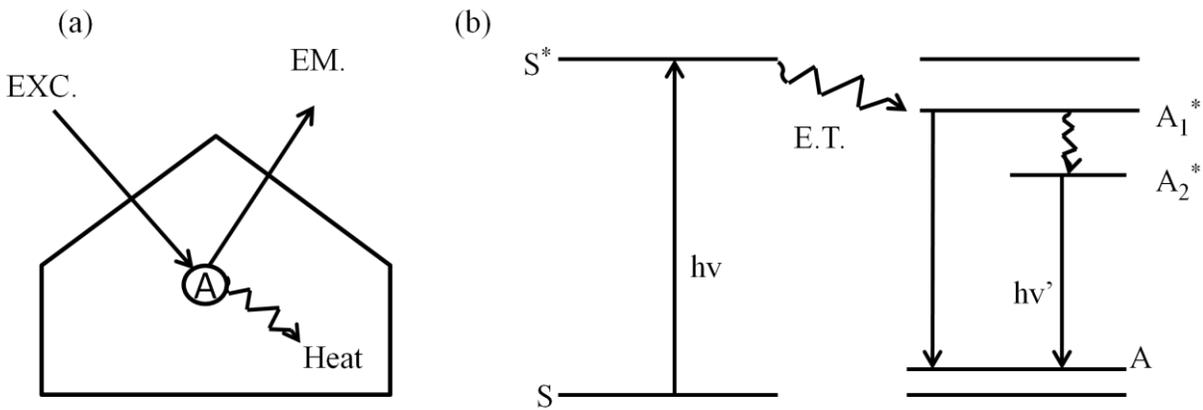
Figure 1.3: (a) Luminescent ion A in the host lattice, EXC: excitation, EM: emission, Heat and (b) Schematic energy level diagram of the luminescent ion A in the host lattice [11].

Figure 1.3 represents a simple luminescence system. Figure 1.3a shows that the exciting radiation (EXC) is absorbed by the activator ion (A) which gives out emission (EM) and loss of some heat as phonons. Figure 1.3b shows the transfer of energy (hv) from S to S^* and the subsequent trapping at trap level A_1^* before it is released to the ground state by the emission of

the radiation, called luminescence or detrapping at trap level A_2^* and return to the ground state by transferring energy to excite the vibrations of the host lattice, *i.e.* transfer heat as phonons to the host lattice [11].

There are different types of luminescence, and each type of luminescence may be referred to by a name according to the method of excitation. There are several processes by which electrons can be excited in luminescent materials. Shown in table 1.1 is a list of some important types of luminescence processes and the corresponding excitation mechanism. In this study, only thermoluminescence and photoluminescence processes will be discussed in detail.

Table 1.1: Various types of luminescence [1].

Type of luminescence	Excitation source
Thermoluminescence	Heating
Photoluminescence	Light (photons)
Cathodoluminescence	Electrons
Electroluminescence	Electric field or Current
Radioluminescence	X-rays

1.3.1 Thermoluminescence

Thermoluminescence (TL) is defined as the luminescence phenomenon of an insulator or semiconductor which can be observed when a solid material is thermally stimulated [20]. The light energy released in this type of luminescence is derived from electron displacements within crystal lattice of a material caused by previous exposure of the material to high-energy radiation

[21]. The process of thermoluminescence can be understood in terms of the band structure model of insulators.

In a pure insulator there are two relevant energy bands: (i) an almost completely filled valence band and (ii) an almost empty conduction band. The two energy bands are said to be separated by a forbidden gap, meaning between these two bands there are no electronic energy levels.
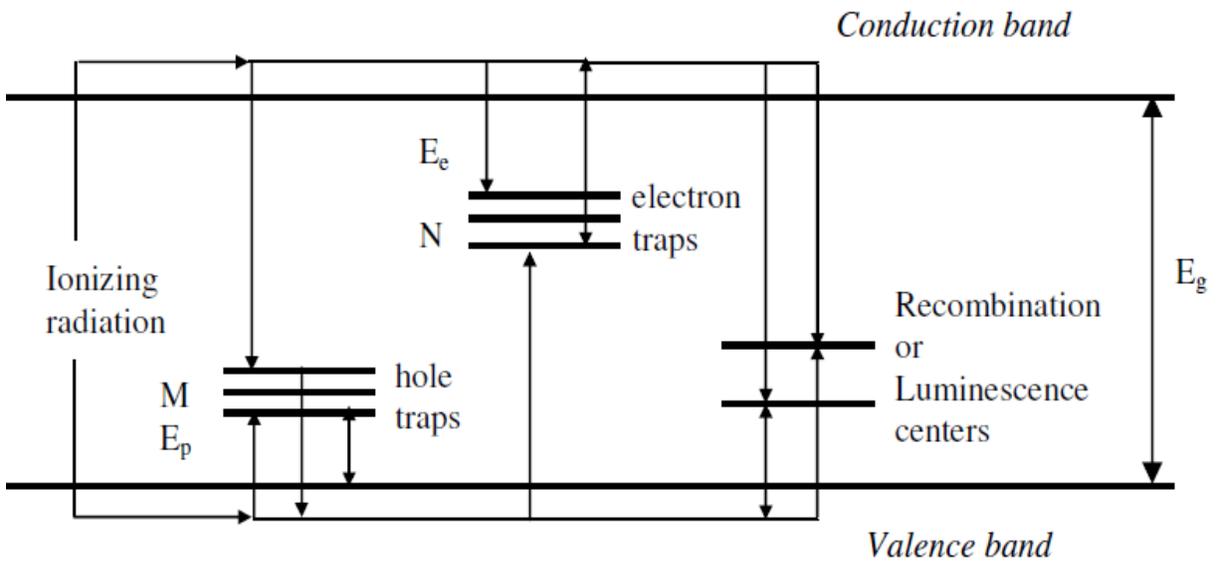
Figure 1.4: Energy-level presentation of the thermoluminescence process, showing the filling process of the electron and hole traps and the mechanism, which is responsible for thermally activated luminescence (TL). N = the total concentration of electron traps with energy E_e, M = the total concentration of hole traps with energy E_p [22].

Transitions of electrons between the valence band and the conduction band are allowed and they produce "free" electrons in the conduction band and "free" holes in the valence band. The energy difference between the two bands is denoted by the band-gap energy E_g. In the crystal, associated with impurities and/or lattice defects may create new localized energy levels in the forbidden band gap. The positions of the energy levels depend on the nature of the defects and the host lattice. Some of these defects are capable to trap an electron or a hole. Therefore the centers are referred to as electron or hole traps and after trapping an electron or hole the new defects are

called trapped electron or trapped hole centers, respectively. A trap is characterized by the energy E that a trapped electron (or hole) must acquire from lattice vibrations to escape to the conduction band (or valence band). Electrons in the conduction band can move freely in the crystal. Holes which were removed from traps are free to move in the crystal, when they are excited to energy levels in the valence band. There is a characteristic temperature at which the thermal vibrations of the crystal lattice are sufficient to cause the release of trapped electrons. Some of the released electrons reach luminescence centers, which are filled with holes, and light is emitted in the recombination process (figure 1.4) [22].

1.3.1.1 Glow-curve

TL is usually generated by heating a sample at a constant rate to some temperature (e.g. $500^{o}C$) and recording the luminescence emitted as a function of temperature. The TL signal is characterised by the so-called "glow curve", with distinct peaks occurring at different temperatures, which relate to the electron traps present in the sample. Defects in the lattice structure are responsible for these traps. A typical defect may be created by the dislocation of a negative ion, providing a negative ion vacancy that acts as an electron trap. Once trapped, an electron will eventually be evicted by thermal vibrations of the lattice. As the temperature is raised these vibrations get stronger, and the probability of eviction increases so rapidly that within a narrow temperature range trapped electrons can be liberated quickly. Some electrons then give rise to radiative recombination with trapped "holes", resulting in emission of light by thermoluminescence (TL) process [23].

1.3.1.2 Glow-curve deconvolution

Computerized glow-curve deconvolution (CGCD) analysis has been widely applied to resolve a complex thermoluminescence glow curve into individual peak components. Once each component is determined, the trapping parameters, activation energy, and the frequency factor, can be evaluated. CGCD is based on the chi-square minimization procedure [25]. S. Sharma et al, reported that the first order GCD function using the glow fit software can be used to calculate the glow-curve parameters. Example of the deconvoluted glow-curve is shown in figure 1.5 [24].

17
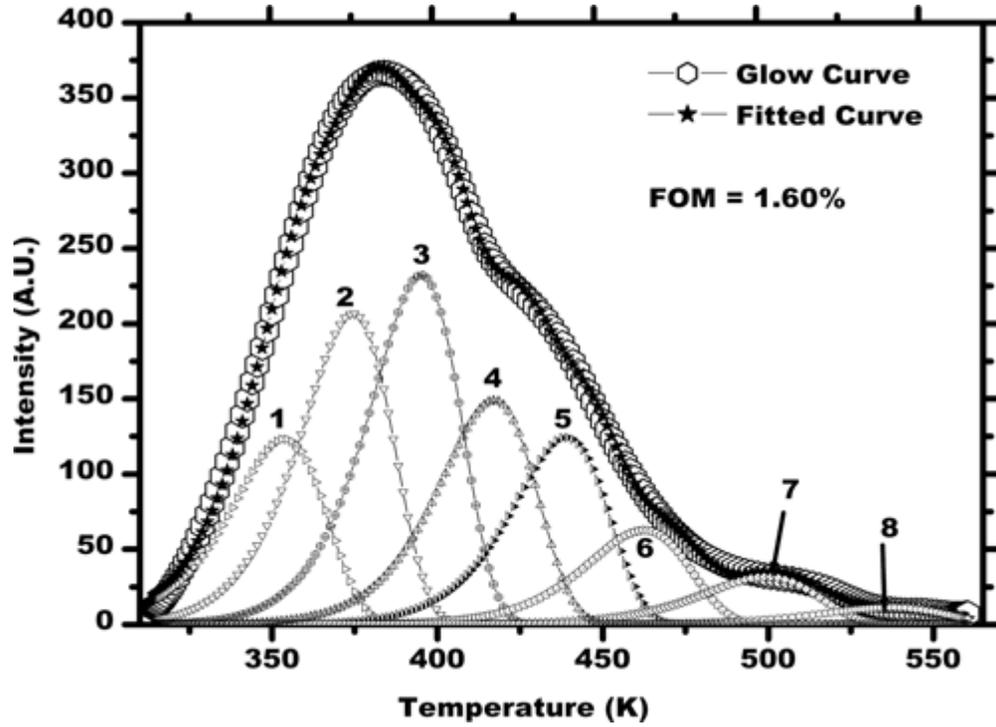
Figure 1.5: A deconvoluted TL glow curve using the CGCD technique recorded [24].

The equation that was used in the software can be written as follows:

$$I(T) = I_M \ \exp\left[1 + \frac{E}{kT} \times \frac{T - T_M}{T_M} - \frac{T^2}{T_M^2} \times (1 - \Delta_M) \exp\left(\frac{E}{kT} \times \frac{T - T_M}{T_M}\right) - \Delta_M\right]$$

Where, $\Delta_M = \dfrac{2kT_M}{E}$, T_M and I_M are the TL intensity and temperature at the glow peak maximum, respectively, E is the activation energy (eV), and k is the Boltzmann's contant. For determining the frequency factor(s), the following equation can be used:

$$s = \frac{\beta E}{kT_M^{\,2}} \exp\left(\frac{E}{kT_M}\right)$$

where β is defined as the heating rate.

1.3.2 Photoluminescence

Photoluminescence can be defined as the emission of light which is caused by the irradiation of a substance with other light. The term embraces both fluorescence and phosphorescence, which differ in the time after irradiating over with the luminescence occurs [25]. Photoluminescence is divided into two major types, namely, intrinsic and extrinsic luminescence. Intrinsic luminescence is then sub-divided into three kinds, band-to-band luminescence, exciton luminescence, and cross-luminescence. Extrinsic luminescence is divided into unlocalized and localized types, depending on whether excited electrons and holes of the host lattice participate in luminescence processes or whether the luminescence excitation and emission processes are confined to localized centers [26].

1.3.2.1 Intrinsic luminescence

1.3.2.1.1 Band-to-band luminescence

Band-to-band luminescence is due to the band to band transition, i.e, recombination of an electron in the conduction band with a hole in the valence band and can be observed in the very pure crystals at relatively high temperatures. This luminescence is transformed into exciton luminescence at the very low temperatures [26].

1.3.2.1.2 Exciton luminescence

An exciton is a composite particle of an excited electron and a hole interacting with each other. It moves in a crystal conveying energy and produces luminescence due to recombination of the electron and the hole [26].

1.3.2.1.3 Cross luminescence

Cross-luminescence can be produced by the recombination of an electron in the valence band with a hole created in the outermost core band. This type of luminescence can take place only when the energy difference between the top of the valence band and that of the outermost core band is smaller than the band gap energy, i.e. $E_{c\text{-}v} < E_g$ [26].

1.3.2.1.4 Extrinsic luminescence

The extrinsic luminescence is caused by intentionally incorporated impurities, in most cases metal impurities, or defects impurities. Intentionally incorporated impurities are called activators and materials made luminescent in this way are called phosphors. Extrinsic luminescence in ionic crystals and semiconductors is classified into two types, the unlocalized and the localized types. In the unlocalized type, the electrons and holes of the host lattice, i.e. free electrons in the conduction band and free holes in the valence band, participate in the luminescence process, while in case of the localized type, the luminescence excitation and emission processes are confined in a localized luminescence center [26].

1.4 Classification of phosphors: Fluorescence vs phosphorescence

The term photoluminescence embraces both fluorescence and phosphorescence processes, which differ in the time after irradiating over which the luminescence occurs [27].

1.4.1 Fluorescence

Fluorescence can be defined as the emission of light by a substance that has absorbed light or other electromagnetic radiation of a different wavelength [28]. The process of fluorescence can be explained as shown in figure 1.6. Figure 1.6(a) shows a pair of electrons occupying the same electronic ground state having opposite spins and are said to be in a single spin state. If a photon is absorbed, one of the electrons is then excited to the singlet excited state (Figure 1.6(b)). This phenomenon is then called excitation. The excited states are not stable and will not stay indefinitely. In some cases an electron in a singlet excited state is transformed to a triplet excited state (Figure 1.6(c)) in which its spin is no longer paired with that of the ground state [29].
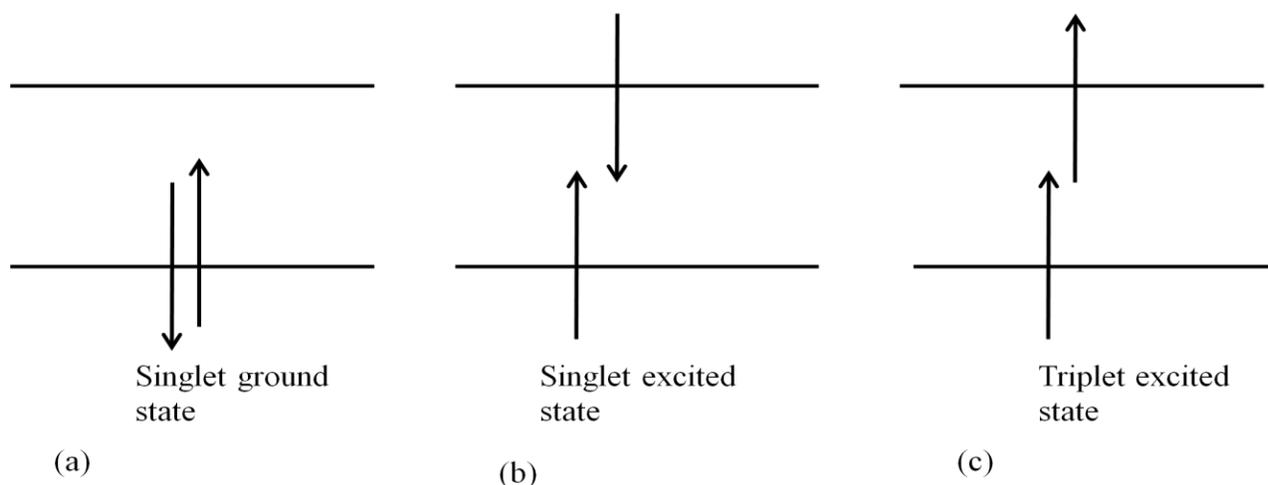
Figure 1.6: Spin in the ground and excited states [29].

In this case the molecule in an excited state will spontaneously return to the ground state after some time and this return process is called decay, deactivation or relaxation. The energy absorbed during the excitation process is released during the relaxation in the form of a photon and this type of relaxation is called emission. The emission of a photon from singlet excited to singlet ground state, or in between any two energy levels with the same spin is called fluorescence. Fluorescence process decays rapidly after the excitation source is removed since the average life time of an electron in the excited state is only 10^{-5} to 10^{-8}s [29].

1.4.2 Phosphorescence

Phosphorescent substances are said to be having the ability to store up light and release it gradually after removing excitation. The notion of a metastable state explains the process of phosphorescence. In this case, if the molecules of the substance are excited from the ground state to a metastable state, and the metastable state can slowly decay back to the ground state via photon emission, then we have phosphorescence [30].

Typically, the metastable state is a triplet state, and the ground state is a singlet state. Ground state molecules absorb photons and go to excited singlet states (see figure 1.7). Most of them immediately return to the ground state, emitting a photon, but non-radiative processes take a few to a less energetic triplet state. Once these molecules get to the lowest triplet state, they stay there

for a while. Some low probability process accomplishes the triplet-singlet conversion, and the molecules slowly give out light [30].
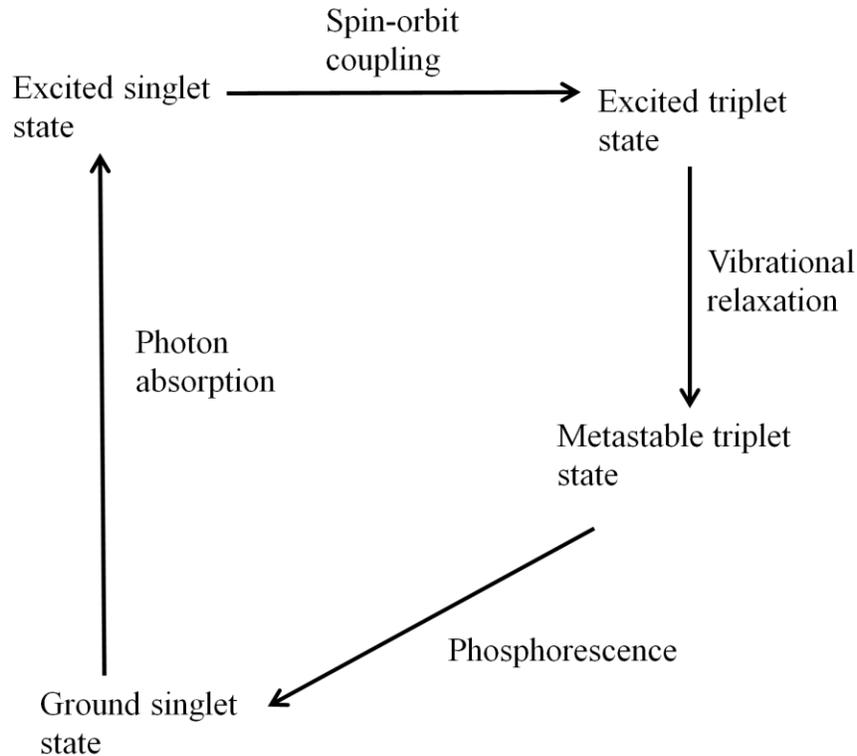
Figure 1.7: Schematic diagram showing Phosphorescence [30].

1.5 Application of phosphors

Persistence luminescence materials, especially those activated with rare earth ions, are widely used in large field of applications, such as fluorescent lamps, plasma display, cathode ray tubes, field emission display, plasma display panels (PDP's) and fiber amplifiers. In addition, their applications are being expanded to optoelectronics of image storage and detectors of energy radiation [31, 32, 33]. They can also be used in other simple applications, such as luminous paints with long persistent phosphorescence [34], phosphorescence pigments for luminous watches and clocks [35] and emergency lighting, safe traffic and wall paintings [36].

The persistence luminescent phosphors have been developed and have been in the commercial market since the mid-1990s. These phosphors include the Eu^{2+} doped alkaline earth aluminates $MAl_2O_4{:}Eu^{2+}$ (M= Ca and Sr). Shown in table 1.2 are some applications of rare earths luminescence that are already in commercial markets [37].

Table 1.2: Applications of rare earth luminescence [37]

Application	R's used	Excitation	Critical features
Lighting	$Eu^{2+}, Eu^{3+}, Tb^{3+}$	UV-radiation	chemical stability, UV-absorption
TV/cathode ray tubes	Eu^{2+}, Eu^{3+}	Electrons	chemical stability, fast luminescence
Scintillators	Ce^{3+}	X-rays	Absorption of radiation, fast luminescence
Electroluminescence	$Ce^{3+}, Eu^{3+}, Tb^{3+}$	Electric field	Energy conversion, fast luminescence
IR-vis conversion	$Yb^{3+}, Er^{3+}, Tm^{3+}$	IR-radiation	Energy transfer
Laser	Nd^{3+}, Yb^{3+}	(UV-)radiation	Chemical stability, laser action
Fiber optics	Er^{3+}	IR-radiation	Transparency
Persistent luminescence	$Eu^{2+}; Nd^{3+}/Dy^{3+}$	Thermal energy	Depth traps

1.5.1 Examples of phosphorescent materials

Luminous paint or luminescent paint is a paint that exhibits luminescence. In other words, it gives off visible light through fluorescence and phosphorescence. Phosphorescent paint is commonly called "glow-in-the-dark" paint. It is made from phosphors such as silver-activated zinc sulfide or, more recently, doped strontium aluminate, and typically glows a pale green to greenish blue color. Phosphorescent paints have a sustained glow which lasts for some minutes or hours after exposure to light, but will eventually fade over time [38]. Some examples of glow in the dark are shown in figure 1.8. These applications consist of different colors of luminous

paints, glow in the dark watch, different kinds of warning signs and luminous watch [39, 40, 41, 42].
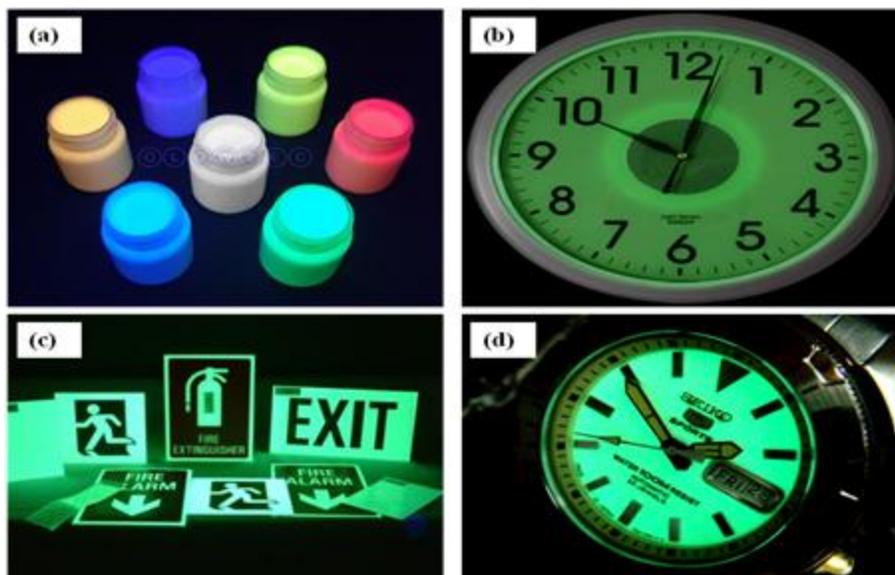
Figure 1.8: Various examples of application of phosphors: (a) different colors of luminous paints, (b) glow in the dark watch, (c) different kinds of warning signs and (d) luminous clocks [39, 40, 41, 42].

1.6 Rare earth ions (Lanthanides)

In this study, different rare earth ions were used to prepare the phosphor powders. The lanthanide elements (or rare earth elements) correspond to a series of elements with a related electronic structure (Table 1.3) [43]. These ions play an important role in modern technology as the active constituents of many optical materials. There are a vast number of applications for these rare-earth-activated materials and much of today's cutting-edge optical technology and emerging innovations are enabled by their unique properties. Specific applications may employ the rare earths' atomic-like $4f^N$ to $4f^N$ optical transitions when long lifetimes, sharp absorption lines, and excellent coherence properties are required, while others may employ the $4f^N$ to $4f^{N-1}5d$ transitions when large oscillator strengths, broad absorption bands, and shorter lifetimes are desirable. They are commonly used for application as phosphors, lasers and amplifiers [44].

Lanthanide ions are formed by ionization of a number of atoms located in a periodic table after lanthanum: from the cerium atom (atomic number 58), which has an outer electronic configuration $5s^2 5p^6 5d^1 4f^1 6s^2$, to the ytterbium atom (atomic number 70), with an outer electronic configuration $5s^2 5p^6 4f^{14} 6s^2$. These atoms are usually incorporated in crystals as divalent or trivalent cations. In trivalent ions 5d, 6s, and some 4f electrons are removed and so $(RE)^{3+}$ ions deal with transitions between electronic energy sublevels of the $4f^n$ electronic configuration. Divalent lanthanide ions contain one more f electron, but at variance with trivalent ion, they show $f \rightarrow d$ interconfigurational optical transitions [45].

Table 1.3: Electronic ground state and ion size of lanthanide elements [43].

Element	Atomic Number	Electronic Ground State	$r(Ln^{3+})$ / pm	
La	57	$5d^1 6s^2$	122	
Ce	58	$4f^1 5d^1 6s^2$	107	Ce^{4+} ($r = 94$ pm)
Pr	59	$4f^3 6s^2$	106	
Nd	60	$4f^4 6s^2$	104	
Pm	61	$4f^5 6s^2$	106	$t^{1/2}(^{147}Pm) = 2.62$ yr
Sm	62	$4f^6 6s^2$	100	
Eu	63	$4f^7 6s^2$	98	Eu^{2+} ($r = 112$ pm)
Gd	64	$4f^7 5d^1 6s^2$	97	
Tb	65	$4f^9 6s^2$	93	
Dy	66	$4f^{10} 6s^2$	91	
Ho	67	$4f^{11} 6s^2$	89	
Er	68	$4f^{12} 6s^2$	89	
Tm	69	$4f^{13} 6s^2$	87	
Yb	70	$4f^{14} 6s^2$	86	
(Lu)	71	$4f^{14} 5d^1 6s^2$	85	

1.7 Crystal structure of BaAl$_2$O$_4$

$BaAl_2O_4$, which belong to the family of stuffed tridymite, is a high melting-point material with a good dielectric, pyroelectric and hydraulic-hardening properties [46]. The stuffed tridymite are derived from the structure of SiO_2 β-tridymite. As Al^{3+} replaces Si^{4+} in tetrahedral of SiO_2 tridymite, Ba will occupy sites in the channels parallel to the c-axis. At room temperature, $BaAl_2O_4$ is hexagonal with space group P6$_3$ and has a superstructure having unit cell parameters 2a, c where a and c are the lattice parameters of hexagonal tridymite. Each oxygen ion is shared

by two aluminium ions so that each tetrahedron has one net negative charge. The charge balance is achieved by the divalent cation like Ba^{2+}, which occupy interstitial site within the tetrahedral frame-work. The tetrahedral frame-work is isostructural within the tridymite structure [47].

There are two Ba^{2+} sites in the $BaAl_2O_4$ structure. According to the crystal structure, the first Ba^{2+} site (2a) has the multiplicity of two and site symmetry of C_3 while the second one (6c) has the multiplicity of six and site symmetry of C_1. Both Ba^{2+} sites have nine-coordination and the sites are similar in average size (d $(Ba-O)_{Ave}$) = 2.86 Å and 2.87 Å). However, the lower symmetry site has also shorter Ba-O distance (2.69 Å) [5]. Figure 1.9 shows three-dimensional sketch of hexagonal $BaAl_2O_4$ crystal structure.
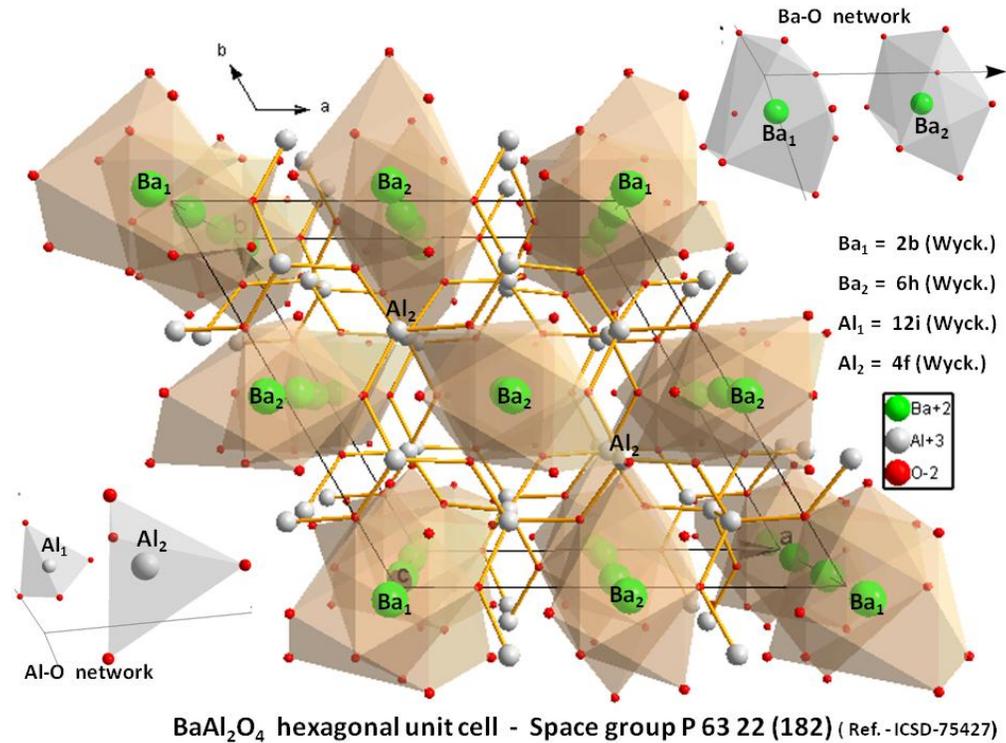
Figure 1.9: Two-dimensional sketch of hexagonal BaAl₂O₄ crystal structure.

1.8 Statement of the problem

In the beginning of this century, ZnS:Cu phosphor was well known as a long phosphorescence phosphor and it was used in a variety of applications. There remains, however practically

important problem with ZnS:Cu phosphor. This phosphor was considered to be environmentally unsafe since, in order for it to sustain it phosphorescence, radioisotopes elements (e.g. Pm^{3+}) were introduced to it [48]. These phosphors also, extremely sensitive to moisture [37] and become more unstable and non-luminescent in the presence of residual gases such as oxygen [1].

In recent years, the alternate afterglow phosphors that are free from radioisotopes and with better properties than ZnS:Cu were invented. The phosphors are the Eu^{2+} activated aluminates such as, $SrAl_2O_4:Eu^{2+};Dy^{3+}$, $BaAl_2O_4:Eu^{2+};Dy^{3+}$, $CaAl_2O_4:Eu^{2+};Nd^{3+}$, etc. These phosphors do exhibit valuable properties such as: high intensity, long lasting photoluminescence, color purity and good chemical stability, thermal and radiation resistance [4]. The crystal structure and luminescent properties of phosphors doped with different rare earth ions and prepared at different initiating temperature were investigated.

1.9 Research objectives

To investigate:

(i)   The effect of different rare earth ions on the structural and luminescent properties of $BaAl_2O_4:Eu^{2+}$ phosphor powders prepared by combustion method

(ii)   The effect of different initiating temperatures on the structural and luminescent properties of $BaAl_2O_4:Eu^{2+}$ co-doped Nd^{3+} and Gd^{3+} ions phosphor powders prepared by combustion method

(iii)   The effect of Zn^{2+} and Ba^{2+} concentrations on the luminescent properties of $(Ba_{1-x}Zn_x)Al_2O_4:Eu^{2+};Nd^{3+}$ phosphor powders prepared by combustion method

(iv)   The effect of Sr^{2+} and Ba^{2+} concentrations on the luminescent properties of $(Ba_{1-x}Sr_x)Al_2O_4:Eu^{2+};Nd^{3+}$ phosphor powders prepared by combustion method

1.10 Thesis Layout

- **Chapter 2** gives a brief explanation of the experimental techniques used to synthesize and characterize the alkaline earth aluminates phosphor powders. The combustion method used to synthesize this phosphor powders is explained in details. Detailed information on how the research techniques used to investigate the luminescent and structural properties of the phosphor powder is also given.

- **Chapter 3** gives the detailed information on the luminescence (PL and TL), structural (XRD and FT-IR) properties and morphology (SEM) of the synthesized $BaAl_2O_4:Eu^{2+}$ co-doped with different rare earth ions.

- **Chapter 4** gives the effect of the initiating temperatures (400^oC-1200^oC) in $BaAl_2O_4:Eu^{2+}:Nd^{3+};Gd^{3+}$ phosphor powders on its luminescence and structural properties.

- **Chapter 5** discusses the effect of Sr^{2+} and Ba^{2+} concentrations on the luminescent (PL) properties of $(Ba_{1-x}Sr_x)Al_2O_4:Eu^{2+};Nd^{3+}$ phosphor powders

- **Chapter 6** discusses the effect of Zn^{2+} and Ba^{2+} concentrations on the luminescent properties of $(Ba_{1-x}Zn_x)Al_2O_4:Eu^{2+};Nd^{3+}$ phosphor powders prepared by combustion method.

- **Chapter 7** gives a summary of the thesis, brief conclusion and possible suggestions for future studies.

References

[1] B.M. Mothudi, O.M. Ntwaeaborwa and H.C. Swart, PhD thesis, University of the Free State, RSA, (2009)

[2] M.M. Biggs, O.M. Ntwaeaborwa and H.C. Swart, MSc. Dissertation, University of the Free State, RSA, (2009).

[3] C. Ronda, Luminescence from theory to application, Wiley-VCH publishers, ISBN: 978-3-527-31402-7 (2008)

[4] H. Song and D. Chen, Luminescence **22** 554-558 (2007)

[5] R. Sefani, L.V.C. Rodrigues, C.A.A. Carvalho, M.C.F.C. Felinto, H.F. Brito, M. Lastusaari and J. Holsa, Optical Materials **31** 1815-1818 (2009)

[6] N. Lakshminarasimhan, U.V. Varadaraju, Materials Research Bulletin **43** 2946 – 2953 (2008)

[7] Z. Qui, Y. Zhou, M. Lu, A. Zhang and Q. Ma, Acta Materialia **55** 2615-2620 (2007)

[8] H. Ryu and K.S. Bartwals, Physica B **404** 1714-1718 (2009)

[9] B.M. Mothudi, O.M. Ntwaeaborwa, J.R. Botha, and H.C. Swart, Physica B **404** 4440-4444 (2009)

[10] J. Holsa, H. Jungner, M. Lastusaari and J. Niittykoski, Journal of Alloys and compounds **323-324** 326-330 (2001)

[11] H. N Luitel, T. Watari and C.T. Williams, PhD Dissertation, Saga University, Japan, (2010)

[12] L.C.V. Rodrigues, R.Stefani, H.F.Brito, M.C.F.C.Felinto, J.Holsa, M.Lastusaari, T. Laamanen, M.Malkamaki, Journal of Solid State Chemistry **183** 2365–2371 (2010)

[13] J.M. Ngaruiya, S. Nieuwoudt, O.M. Ntwaeaborwa, J.J. Terblans, H.C. Swart, Materials Letters **62** 3192–3194 (2008)

[14] T. Katsumata, S. Toyomane, R. Sakai, S. Komuro and T. Morikawa, Journal of the American Ceramic Society **89** 932-936 (2006)

[15] T. Katsumata, S. Toyomane, A. Tonegawa, Y. Kanai, U. Kaneyama, K. Shakuno, R. Sakai, S. Komuro, T. Morikawa, Journal of Crystal Growth, 237-239 361-366 (2002)

[16] Y. Lin, Z. Tang, Z. Zhang, and C. Nan, Journal of the European Ceramic Society 23 175–178 (2003)

[17] K. Vishwakarma, M. Ramrakhiani and B.P Chandra, International Journal of Nanotechnology and Applications 1 29-34 (2007)

[18] K.V.R. Murthy and J.N Reddy, Thermoluminescence Basic Theory Application and Experiments, Pbu. No. Nu. Hyd.1/2008, February, (2008)

[29] http://www.asdi.com/general-applications/faq/what-is-luminescence [15 Sep 2011]

[20] A.J.J. Bos, Radiation Measurements 41 45-56 (2007)

[21] http://www.britannica.com/EBchecked/topic/591643/thermoluminescence [15 Sep 2011]

[22] H.J. Van Es, H.W. den Hartog, R.J. de Meijer and D.I. Vainshtein, PhD Dissertation, University of Groningen, Netherlands, (2008)

[23] http://shodhganga.inflibnet.ac.in/bitstream/10603/1926/8/08_chapter%202.pdf [15 Sep 2011]

[24] S.K. Sharma, S.S. Pitale. M.M. Malik, R.N. Dubey and M.S Qureshi, Physica Status Solidi 205 2695-2703 (2008)

[25] http://www.rp-photonics.com/photoluminescence.html [15 Sep 2011]

[26] S. Shionoya, Luminescence of solids, Plenum Press, New York, p95-96 (1998)

[27] http://www.rp-photonics.com/photoluminescence.html [14 Sep 2011]

[28] http://en.wikipedia.org/wiki/Fluorescence [14 Sep 2011]

[39] http://einstein.sc.mahidol.ac.th/~jose/pdf/photoluminescence.pdf [15 Sep 2011]

[30] http://math.ucr.edu/home/baez/spin/node17.html [15 Sep 2011]

[31] S. Feilong and Z. Junwu, Journal of rare earths, 29 326-329 (2011)

[32] H.C Swart, E. Coetsee, J. J Terblans, O. M Ntwaeaborwa, P. D Msimama, F. B, Dejene, J. J Dolo, Applied Physics A 101 633-638 (2010)

[33] M. Peng and G. Hong, Journal of Luminescence 127 735-740 (2007)

[34] B. Yang and J. Wu, Materials Letters 61 4851-4853 (2007)

[35] H. Ryu, B. K. Singh and K. S. Bartwals, Journal of the Korean Ceramic Society **45** 146-149 (2008)

[36] A.S Maia, R. Stefani, C.A. Kodaira, M.C.F.C. Felinto, E.E.S. Teotonio and H.F. Brito, Optical Materials **31** 440-444 (2008)

[37] T. Aitasalo, P. Deren, J. Holsa, H. Jungner, J. -C. Krupa, M. Lastusaari, J. Legendziewics J. Niittykoski and W. Strek, Journal of Solid State Chemistry **171** 114-122 (2003)

[38] http://en.wikipedia.org/wiki/Luminous_paint [15 Sep 2011]

[39] http://glowpaints.co.uk/glow-paints.htm] [15 Sep 2011]

[40] http://www.bodyingcare.com/kb_cat.php?id=9 [15 Sep 2011]

[41] http://emmybella.wordpress.com/production-of-light/ [15 Sep 2011]

[42] http://www.latestbuy.com.au/glow-in-the-dark-clock.html [15 Sep 2011]

[43] http://andrew.ucsd.edu/courses/sio263/ClassNotes/7.pdf [15 Sep 2011]

[44] C. W. Thiel, Y. Sun and R. L. Cone, Journal of Modern Optics **49** 2399-2411 (2002)

[45] J. Garcia Sole, L. E. Bausa, D. Jaque, An Introduction to the Optical Spectroscopy of Inorganic Solids, John Wiley and Sons, p200-201(2005)

[46] L. Zhang, L. Wang and Y. Zhu, Advanced Functional Materials **17** 3781-3790 (2007)

[47] H. Ryu and K. S. Bartwal, Crystal Research and Technology **44** 69-73 (2009)

[48] T. Matsuzawa, Y. Aoki, N. Takeuchi and Y. Murayama, Journal of the Electrochemical Society **143** 2670-2673 (1996)

CHAPTER 2

SYNTHESIS AND CHARACTERIZATION TECHNIQUES

Introduction

The method used to synthesize phosphor powders and a wide variety of experimental techniques used to characterize the phosphors are presented in this chapter. The combustion method was used to synthesize the alkaline earth aluminate phosphors. X-ray diffraction (XRD) and scanning electron microscopy (SEM) coupled with the energy dispersive X-ray (EDS) spectrometer were used to investigate the crystalline structure, particle morphology and elemental composition of the phosphor powders, respectively.

Fourier transform infrared (FTIR) spectroscopy was used to determine the stretching mode frequencies. The X-ray Photoelectron Spectroscopy (XPS) was used to monitor the elemental composition on the surfaces of the phosphor powders. A 325 nm He-Cd laser fitted with a SPEX 1870 0.5m spectrometer and a photomultiplier tube detector was used to collect photoluminescence data in air at room temperature. A Cary Eclipse fluorescence spectrometer fitted with a monochromatized xenon lamp was also used to record photoluminescence as well as decay characteristics data of the phosphor powders. Thermoluminescence Reader (Integral-Pc Based) Nucleonix TL 1009I was used to study the different trap depths of the phosphors.

2.1. Synthesis Techniques

2.1.1. Combustion method

The combustion method has emerged as an important synthetic route for the synthesis and processing of advanced ceramics (structural and functional), catalysts, composites, alloys, intermetallics and nanomaterials. The combustion process has generated more interest in the study of the synthesis of luminescent inorganic nanomaterials (phosphors) and ceramic materials, because fine particle sizes, multicomponent, crystalline and homogenous materials can be achieved at relatively low temperature and short reaction time. The combustion process involves a redox (reduction- oxidation) reaction between an oxidizer such as metal nitrates and an organic fuel such as urea (CH_4N_2O), carbonhydrazide (CH_6N_4O), citric acid ($C_6H_8O_7$) or glycerine ($C_2H_5NO_2$). In general, good fuels should react non-violently, produce nontoxic gases, and act as chelating agents for metal cations. Among the well-known fuels, urea and glycerine have demonstrated the versatility for combustion synthesis method by the successful preparation of large number of single phase and well crystallized multicomponent oxides [1].

The combustion process involves an exothermic reaction that occurs with evolution of heat. Once the precursors are ignited the energy necessary for the combustion reaction is supplied from the reaction itself, and hence this process is sometimes called self-propagating low temperature synthesis. The luminescent materials (phosphors) prepared by the combustion method have low density and have a fluffy texture. Ultra-fine particles produced during the combustion reaction are accompanied by the evolution of gases. As more gases are released, either agglomerates are formed or disintegrated into fine particles. Furthermore, compared to other conventional ceramic processing techniques, the combustion method has shown several advantages such as [1]:

(i) Short reaction times.
(ii) Inexpensive processing equipment.
(iii) Production of final product in one step using the chemical energy of the reactants.
(iv) Liberation of volatile impurities and thus higher purity products.

2.2. Characterization Techniques

2.2.1. X-ray Diffractometer (XRD)

X-ray diffraction (XRD) is a powerful non-destructive technique used to investigate structural properties of crystalline materials. It can be used in application such as phase identification, determination of grain size, composition of solid solution, lattice constants and degree of crystallinity in the mixture of amorphous and crystalline substances [2].

X-ray diffractometry falls broadly into two classes: single crystal and powder. The powder diffractometry is routinely used for phase identification and quantitative phase analysis. X-ray diffractometer consists of three basic elements: an X-ray tube, a sample holder and an X-ray detector. The X-rays are produced in a cathode ray tube by heating a filament to produce electrons. When the voltage is applied, the electrons will accelerate towards the target material. When electrons have sufficient energy to dislodge the inner shell electrons of the target material, characteristic X-ray spectra will be produced [1].

In order to generate the required monochromatic X-ray needed for diffraction, a filter such as a foil or crystal monochromter is usually used. Copper is the most commonly used target for single-crystal diffraction with Cu K_α radiation = 1.5418 Å. The resulting X-ray are collimated and directed onto the sample. As the sample and detector are rotated, the intensity of the reflected X-ray is recorded. When the geometry of the incident X-rays impinging on the sample satisfies the Bragg law, constructive interference occurs and characteristic diffraction peak of the sample will be observed [1].

2.2.1.1 Bragg's law

Bragg's law is in the form of an equation: $n\lambda = 2d\sin\theta$, derived by English Physicist Sir W.H Bragg and his son Sir W.L. Bragg in 1913 to explain why the cleavage faces of crystals appear to reflect X-ray beams at certain angles of incidence (θ, λ). The variable d is the distance between atomic layers in a crystal, λ is the wavelength of the incident X-ray and n is an integer. This

observation of Bragg's law is an example of X-ray wave interference, commonly known as X-ray diffraction (XRD), and was direct evidence for the periodic atomic structure of crystals postulated for several centuries. Although Bragg's law was used to explain the interference pattern of X-rays scattered by crystals, diffraction has been developed to study the structure of all states of matter with any beam, e.g, ions, electrons, neutrons and protons, with a wavelength similar to the distance between the atomic or molecular structures of interest [3].

2.2.1.2. Bragg's condition

Bragg diffraction occurs when electromagnetic radiation or subatomic particle waves with wavelength comparable to atomic spacing are incident upon a crystalline sample, are scattered in a specular fashion by the atoms in the system, and undergo constructive interference in accordance with Bragg's law. For a crystalline solid, the waves are scattered from lattice planes separated by the interplanar distance d. Where the scattered waves interfere constructively, they remain in phase since the path length of each wave is equal to an integer multiple of the wavelength. The path difference between two waves undergoing constructive interference is given by $2dsin\theta$, where θ is the scattering angle. This leads to Bragg's law, which describes the condition for constructive interference from successive crystallographic planes (h, k, and l, as given in Miller Notation) of the crystalline lattice:

$$n\lambda = 2dsin\theta$$

A diffraction pattern is obtained by measuring the intensity of scattered waves as a function of scattering angle. Very strong intensities known as Bragg peaks are obtained in the diffraction pattern when scattered waves satisfy the Bragg condition [4]. Figure 2.1 shows the formation of Bragg's diffraction. In this case, two beams with identical wavelength and phase approach a crystalline solid and are scattered off two different atoms within it. The lower beam traverses an extra length of $2dsin\theta$. The constructive interference occurs when this length is equal to an integer multiple of the wavelength of the radiation.
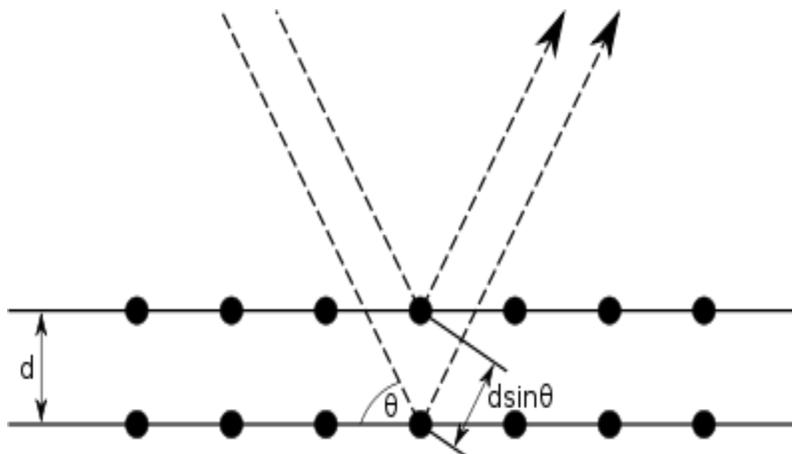
Figure 2.1: Formation of Bragg diffraction.

Shown in figure 2.2 is D8 Advanced AXS GmbH X-ray diffractometer from University of the Free State Physics Department which was used to analyze the phosphor powders in this study.

Figure 2.2: D8 Advanced AXS GmbH X-ray diffractometer.

2.2.2. Scanning Electron Microscope (SEM)

The Scanning Electron Microscope (SEM) uses a focused beam of high-energy electrons to generate a variety of signals at the surface of solid specimens. Figure 2.3 is the diagram showing the inside view of the SEM. The signals derived from electron-sample interactions reveal information about the sample including external morphology (texture and particle size), chemical composition, and crystalline structure and orientation of materials making up the sample.

 In most applications, the data is collected over a selected area of the surface of the sample, and a 2-dimensional image is generated which displays spatial variations in these properties. Areas ranging from approximately 1 cm to 5 microns in width can be imaged in a scanning mode using conventional SEM techniques (magnification ranging from 20X to approximately 30,000X, spatial resolution of 50 to 100 nm). The SEM is also capable of performing analyses of selected point locations on the sample; this approach is useful especially in qualitatively or semi-quantitatively determining chemical compositions (using EDS), crystalline structure, and crystal orientations (using Electron Backscatter diffraction)[5].

Accelerated electrons in an SEM carry significant amounts of kinetic energy, and this energy is dissipated as a variety of signals produced by electron-sample interactions when the incident electrons are decelerated in the solid sample. These signals include secondary electrons (that produce SEM images), backscattered electrons (BSE), diffracted backscattered electrons (EBSD that are used to determine crystal structures and orientations of minerals), photons (characteristic X-rays that are used for elemental analysis and continuum X-rays), visible light (cathodoluminescence) and heat. Secondary electrons and backscattered electrons are commonly used for imaging samples: secondary electrons are most valuable for showing morphology and topography on samples and backscattered electrons are most valuable for illustrating contrasts in composition in multiphase samples (i.e. for rapid phase discrimination). X-ray generation is produced by inelastic collisions of the incident electrons with electrons in discrete orbitals (shells) of atoms in the sample. As the excited electrons return to lower energy states, they yield X-rays of a fixed wavelength (that is related to the difference in energy levels of electrons in different shells for a given element). Thus, characteristic X-rays are produced for each element in a sample that is "excited" by the electron beam. SEM analysis is considered to be "non-

destructive"; that is, x-rays generated by electron interactions do not lead to volume loss of the sample, so it is possible to analyze the same materials repeatedly [5].
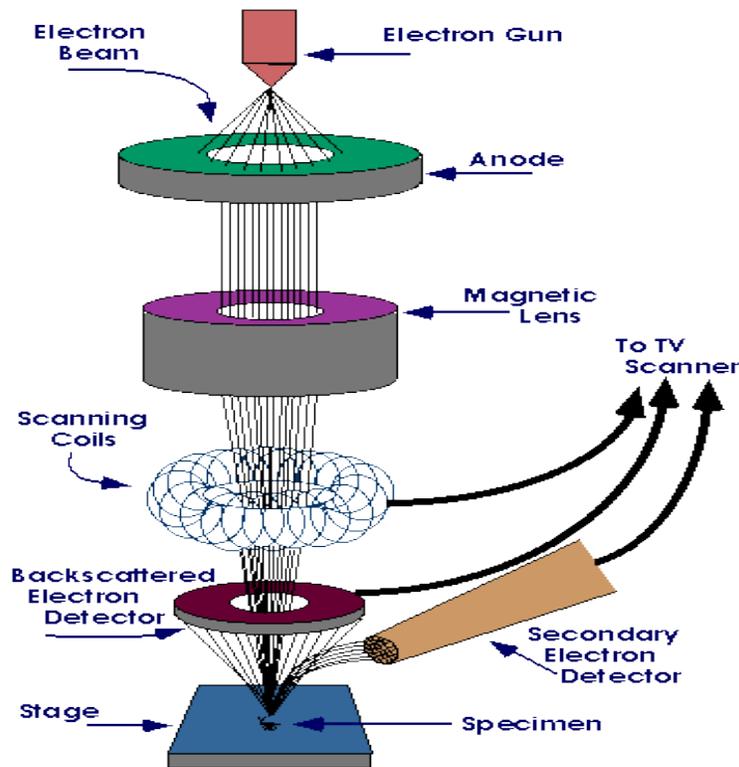
Figure 2.3: Schematic representation of a SEM [6].

2.2.2.1. How does Scanning Electron Microscope work?

The SEM is an instrument that produces a largely magnified image by using electrons instead of light to form an image. A beam of electrons is produced at the top of the microscope by an electron gun. The electron beam follows a vertical path through the microscope, kept in vacuum. The beam travels through electromagnetic fields and lenses, which focus the beam down toward the sample. Once the beam hits the sample (figure 2.4), electrons and X-rays are ejected from the sample [6].

Incident beam

X-rays

Primary backscattered
electrons

Auger electrons

Secondary electrons
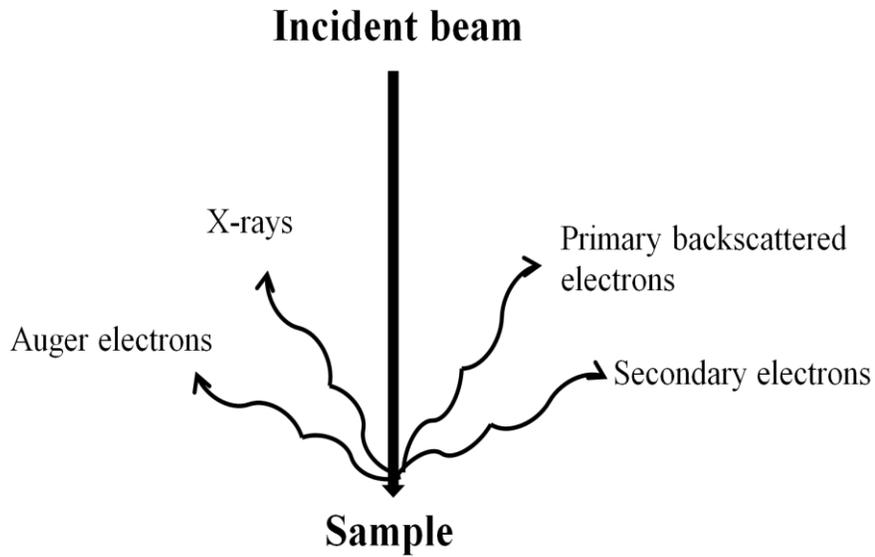
Sample

Figure 2.4: Schematic diagram showing the ejection of electrons and X-rays when beam hits the sample.

Detectors collect these X-rays, backscattered electrons, and secondary electrons and convert them into a signal that is sent to a screen similar to a television screen. This produces the final image. In this study, the morphologies of the phosphor powders were obtained by using a high resolution SEM technique at the University of Pretoria (Figure 2.5).

Figure 2.5: High resolution Scanning Electron Microscope.

2.2.3. Fourier transform infrared spectroscopy (FT-IR)

Fourier Transform Infrared (FTIR) spectroscopy is a failure analysis technique that provides information about the chemical bonding or molecular structure of materials, whether organic or inorganic. It is used in failure analysis to identify unknown materials present in a specimen, and is usually conducted to complement EDX analysis [7].

In infrared spectroscopy, IR radiation is passed through a sample. Some of the infrared radiation is absorbed by the sample and some of it is passed through (transmitted). The resulting spectrum represents the molecular absorption or transmission, creating a molecular fingerprint of the sample. Like a fingerprint no two unique molecular structures produce the same infrared spectrum. This makes Infrared spectroscopy useful for several types of analyses [8].

A molecule that is exposed to infrared rays absorbs infrared energy at frequencies which are characteristic to that molecule resulting in vibration of the bonds. During FTIR analysis, a spot

on the specimen is subjected to a modulated IR beam. The specimen's transmittance and reflectance of the infrared rays at different frequencies is translated into an IR absorption plot consisting of reverse peaks. The resulting FTIR spectral pattern is then analyzed and matched with known signatures of identified materials in the FTIR library [7].

Unlike SEM inspection or EDX analysis, FTIR spectroscopy does not require a vacuum, since neither oxygen nor nitrogen absorbs infrared rays. FTIR analysis can be applied to minute quantities of materials, whether solid, liquid, or gaseous. When the library of FTIR spectral patterns does not provide an acceptable match, individual peaks in the FTIR plot may be used to yield partial information about the specimen [7]. Simplified layout of a FTIR spectrometer is shown in figure 2.6.

2.2.3.1. The Sample Analysis Process

The normal instrumental process is as follows:

1. **The Source:** Infrared energy is emitted from a glowing black-body source. This beam passes through an aperture which controls the amount of energy presented to the sample (andultimatelyto the detector).

2. **The Interferometer:** The beam enters the interferometer where the "spectral encoding" takes place. The resulting interferogram signal then exits the interferometer.

3. **The Sample:** The beam enters the sample compartment where it is transmitted through or reflected off the surface of the sample, depending on the type of analysis being accomplished. This is where specific frequencies of energy, which are uniquely characteristic of the sample, are absorbed.

4. **The Detector:** The beam finally passes to the detector for final measurement. The detectors used are specially designed to measure the special interferogram signal.

5. **The Computer:** The measured signal is digitized and sent to the computer where the Fourier transformation takes place. The final infrared spectrum is then presented to the user for interpretation and any further manipulation.
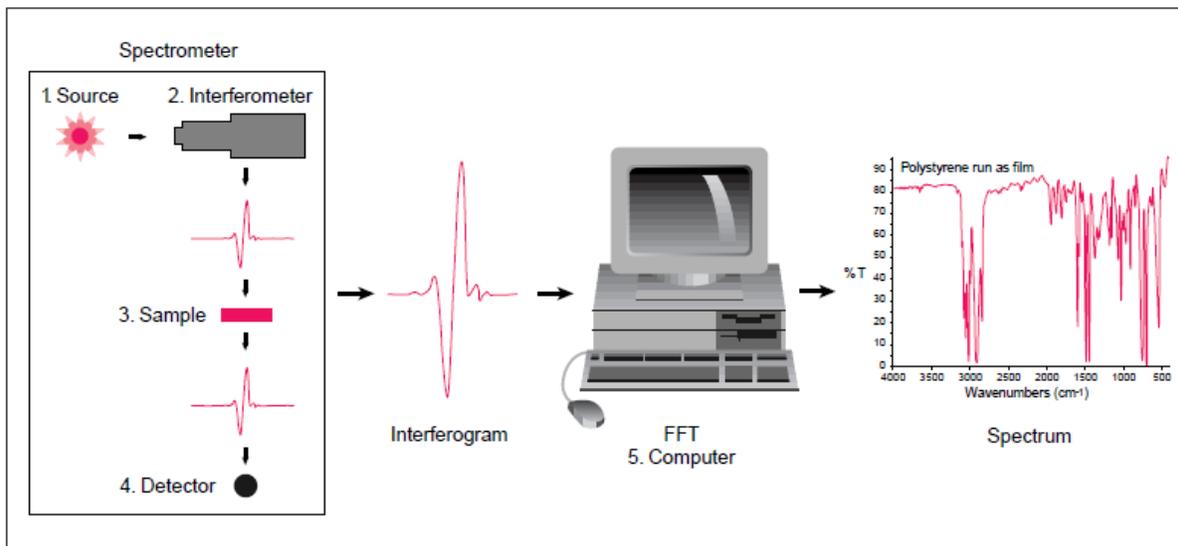
Figure 2.6: Simplified layout of a FTIR spectrometer sample analysis [8].

In a Michelson interferometer adapted for FTIR, Figure 2.7, light from the polychromatic infrared source, approximately a black-body radiator, is collimated and directed to a beam splitter. Ideally 50% of the light is reflected towards the fixed mirror and 50% is transmitted towards the moving mirror. Light is reflected from the two mirrors back to the beam splitter and (ideally) 50% of the original light passes into the sample compartment. Then, the light is focused on the sample [9].
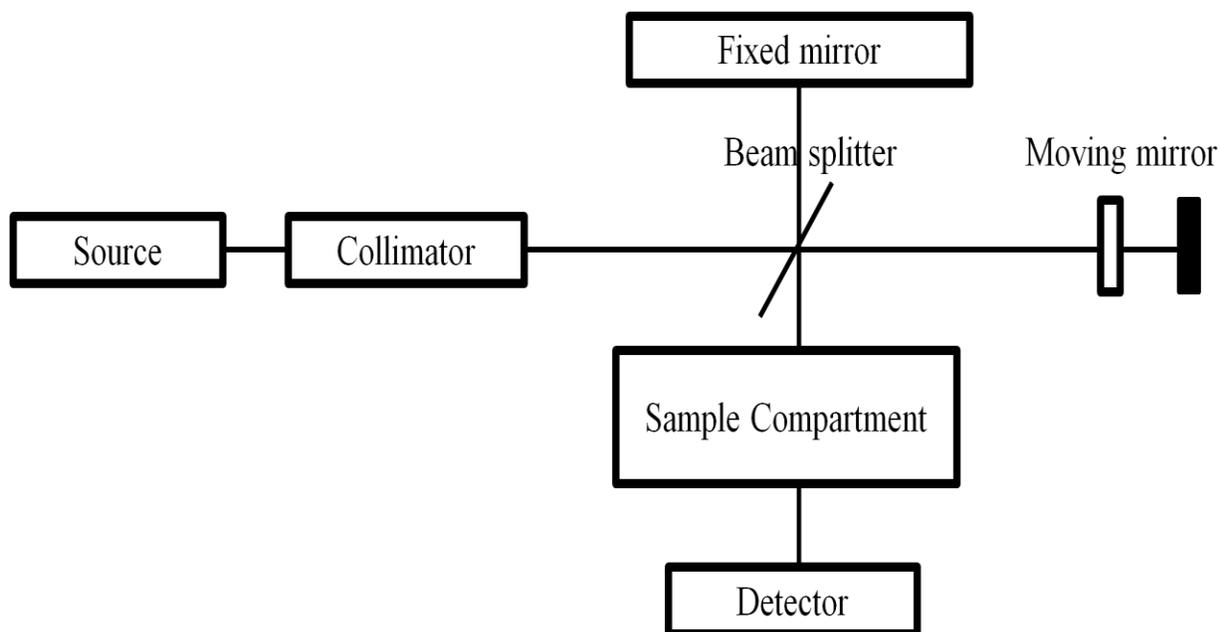
Figure 2.7: Schematic diagram of a Michelson interferometer configured for FTIR [9].

On leaving the sample compartment the light is refocused onto the detector. The difference in optical path length between the two arms to the interferometer is known as the retardation. An interferogram is obtained by varying the retardation and recording the signal from the detector for various values of the retardation. The form of the interferogram when no sample is present depends on factors such as the variation of source intensity and splitter efficiency with wavelength. This results in a maximum at zero retardation, when there are a constructive interference at all wavelengths, followed by series of "wiggles". The position of zero retardation is determined accurately by finding the point of maximum intensity in the interferogram. When a sample is present, the background interferogram is modulated by the presence of absorption bands in the sample [9]. The Perkin Elmer Spectrum 100 FTIR spectrometer, shown in figure 2.8 was used in this study.
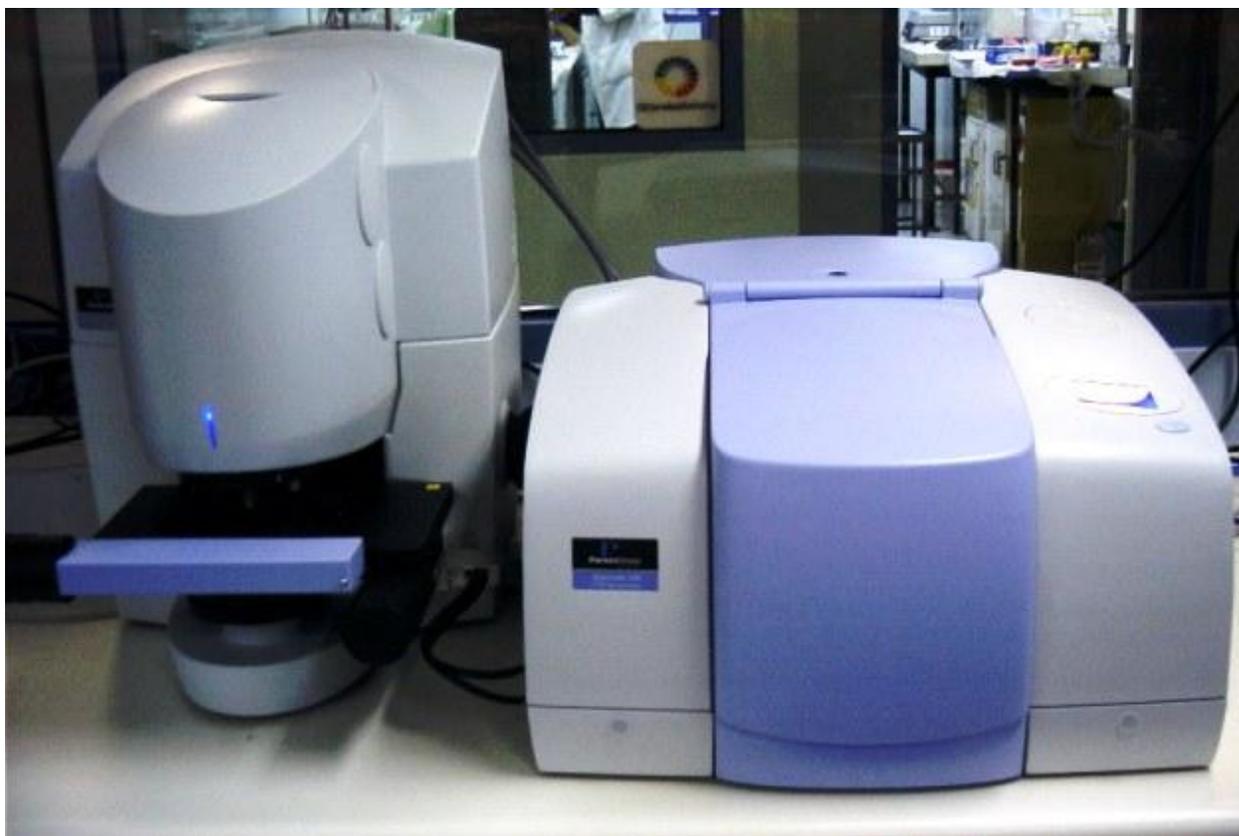
Figure 2.8: Perkin Elmer Spectrum 100 FTIR spectrometer [10].

2.2.4. X-ray photoelectron spectroscopy (XPS)

X-ray photoelectron spectroscopy, also known as electron spectroscopy for chemical analysis (ESCA), is a widely used surface technique to obtain chemical information at surfaces of various materials. The XPS process involves the ejection of an electron (photoelectron) in vacuum from the K level of an atom by an energetic incident x-ray photon. Photoelectrons are collected and analyzed to produce a spectrum of emission intensity versus electron binding energy. In general, the binding energies of the photoelectrons are characteristic of the element from which they are emitted [11].

The logical components of an XPS instrument are shown in figure 2.9. X-rays illuminate an area of a sample causing electrons to be ejected with a range of energies

and directions. The electron optics, which may be a set of electrostatic and/or magnetic lens units, collect a proportion of these emitted electrons defined by those rays that can be transferred through the apertures and focused onto the analyzer entrance slit. Electrostatic fields within the hemispherical analyzer (HSA) are established to only allow electrons of a given energy (the so called Pass Energy PE) to arrive at the detector slits and onto the detectors themselves.
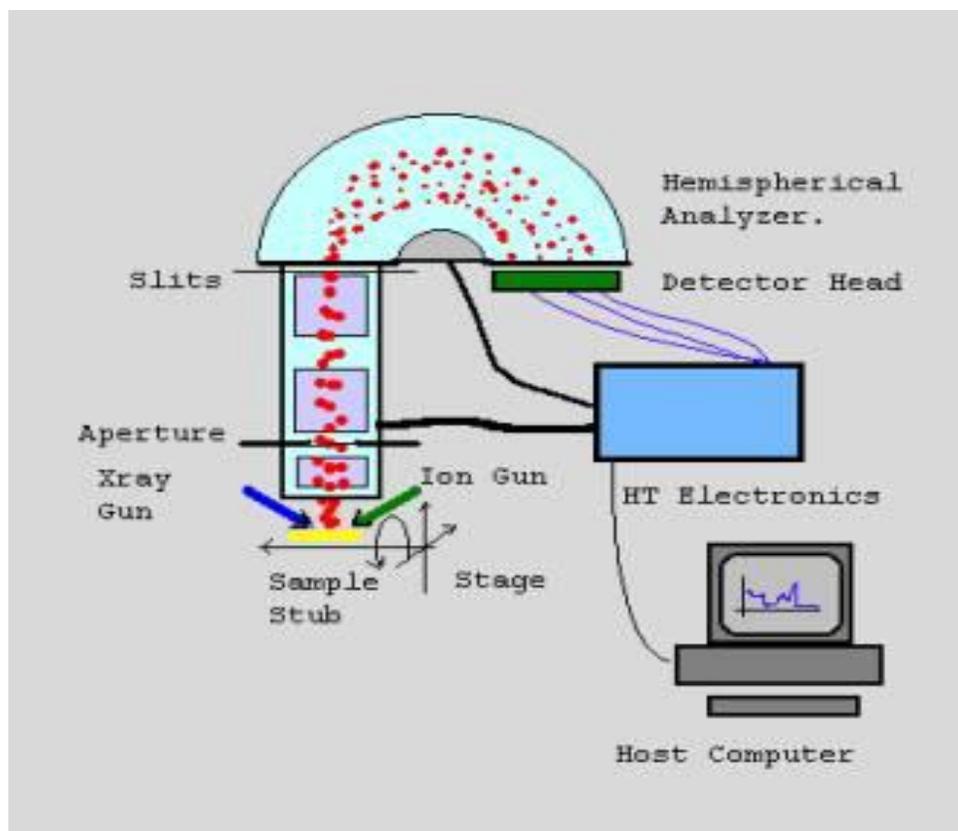
Figure 2.9: Logical layout for an XPS Instrument [12].

Electrons of a specific initial kinetic energy are measured by setting voltages for the lens system that both focus onto the entrance slit the electrons of the required initial energy and retards their velocity so that their kinetic energy after passing through the transfer lenses matches the pass energy of the hemispherical analyzer. To record a spectrum over a range of initial excitation energies it is necessary to scan the voltages applied to these transfer lenses and the prescription for these lens voltages is known as the set of lens functions. These lens functions are typically stored in some configuration file used by the acquisition system.

The efficiency with which electrons are sampled by a spectrometer is very dependent on these lens functions and without properly tuned lens functions the performance of an instrument can be severely impaired. Even with a well-tuned system the collection efficiency varies across the many operating modes and it is necessary to characterize an instrument using a corresponding transmission function for each of the lens modes and energy resolutions [12].

The XPS spectrometer used in this study was the PHI 5000 Versaprobe, shown in figure 2.10, from the University of the Free State, Department of Physics (Bloemfontein).

Figure 2.10: PHI 5400 Versaprobe scanning x-ray photoelectron spectrometer.

2.2.5. Photoluminescence spectroscopy (Helium-cadmium laser)

The Helium-Cadmium (He-Cd) laser is one of a class of gas lasers using helium in conjunction with a metal which vaporizes at a relatively low temperature. A typical construction for the He-

Cd laser is in the form of a tube, terminated by two Brewster's angle windows, with two laser mirrors mounted separately from the tube. The tube filled with helium, also has a reservoir containing the Cd and a heater to vaporize the metal. The reservoir is raised to a high enough temperature (~250 ^{o}C) to produce the desired vapor of Cd atoms in the tube. He-Cd lasers can give output powers of 50 100 mW and it can produce a high quality beam at 442 nm (violet-blue) and/or 325 nm (UV) depending on the optics. In this study a 325 nm He-Cd laser was used to investigate the photoluminescent properties of the phosphors. This was conducted by directing the laser beam on to a sample by using lenses and mirrors, followed by the chopper that was used to ensure that the light beam is sent in packets as illustrated in figure 2.11. To ensure that only the light beam from the sample is sent through the photomultiplier tube detector, the glass GG 385 was used to block the laser beam [13]. The He-Cd laser system, shown in figure 2.12 used in this study was from Nelson Mandela Metropolitan University (NMMU) in Port Elizabeth. A schematic drawing of the He-Cd laser equipment for photoluminescence is shown in figure 2.12.
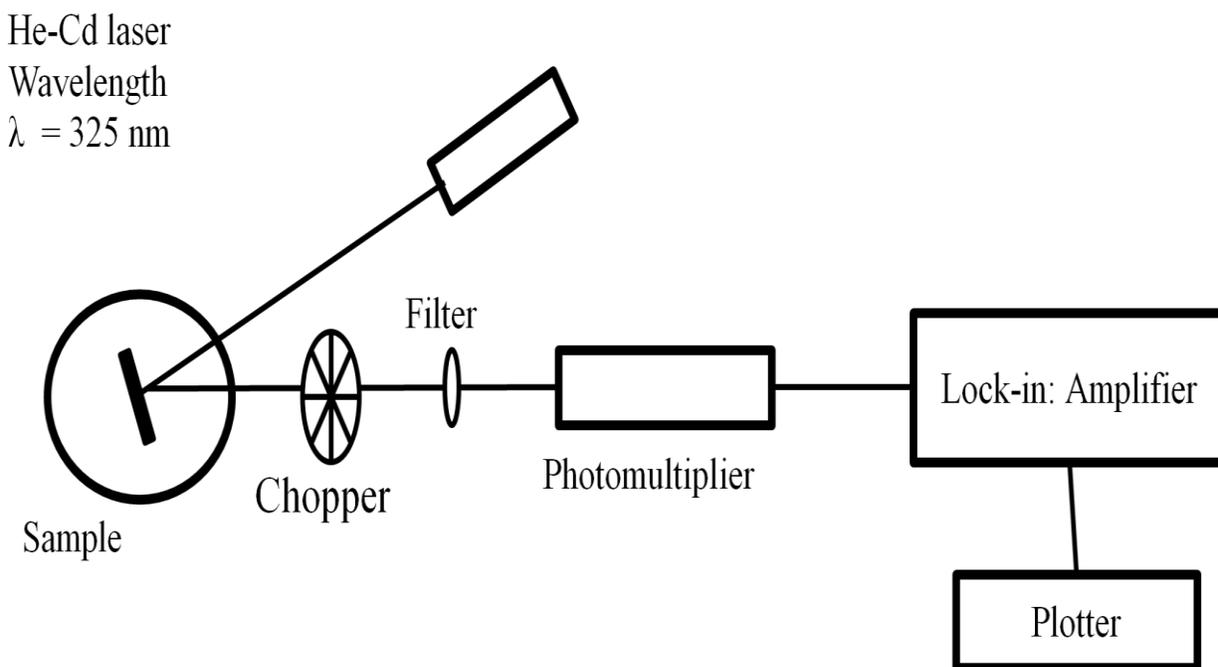
Figure 2.11: A schematic drawing of the He-Cd laser equipment for photoluminescence.

Figure 2.12: He-Cd laser (325 nm) photoluminescent system used to investigate the luminescent properties of the phosphors.

2.2.6. Fluorescence spectrophotometry

Fluorescence spectrophotometry is used to measure the fluorescence or phosphorescence emitted by a substance when exposed to ultraviolet, visible or other electromagnetic radiation. Measurement of the fluorescence intensity can be made by using the fluorescence spectrometer, which consists of a radiation source, monochromator, sample holders and fluorescence detection system [1] as shown in figure 2.14.

Fluorescence is measured using an excitation source placed at 90° to the emission detector Excitation radiation is provided by a xenon flash lamp. The Xenon flash lamp flashes up to 80

times per second and has a pulse width of approximately 2 to 3 microseconds. The Schwartzchild collector mirrors collect the light energy from the Xenon Flash Lamp module. This light is then focused through a lens onto the excitation entry slit. This light passes through an excitation monochromter and into the sample. The resulting fluorescence passes through an emission monochromter and is detected by a photomultiplier. Both monochrometers are Czerny–Turner type, with a dispersion grating (30 x 35 mm, 1200 lines/mm), an accuracy of ± 1.0 nm, and a wavelength repeatability of ± 0.2 nm. Rotation of the grating within each monochrometer allows wavelength selection [13]. Figure 2.13, shows the simplified schematic diagram of the fluorescence spectrophotometer.

In this study a Cary Eclipse Fluorescence Spectrophotometer (shown in figure 2.15) coupled with monochromatized xenon lamp was used to collect the fluorescence and decay data in air at room temperature.
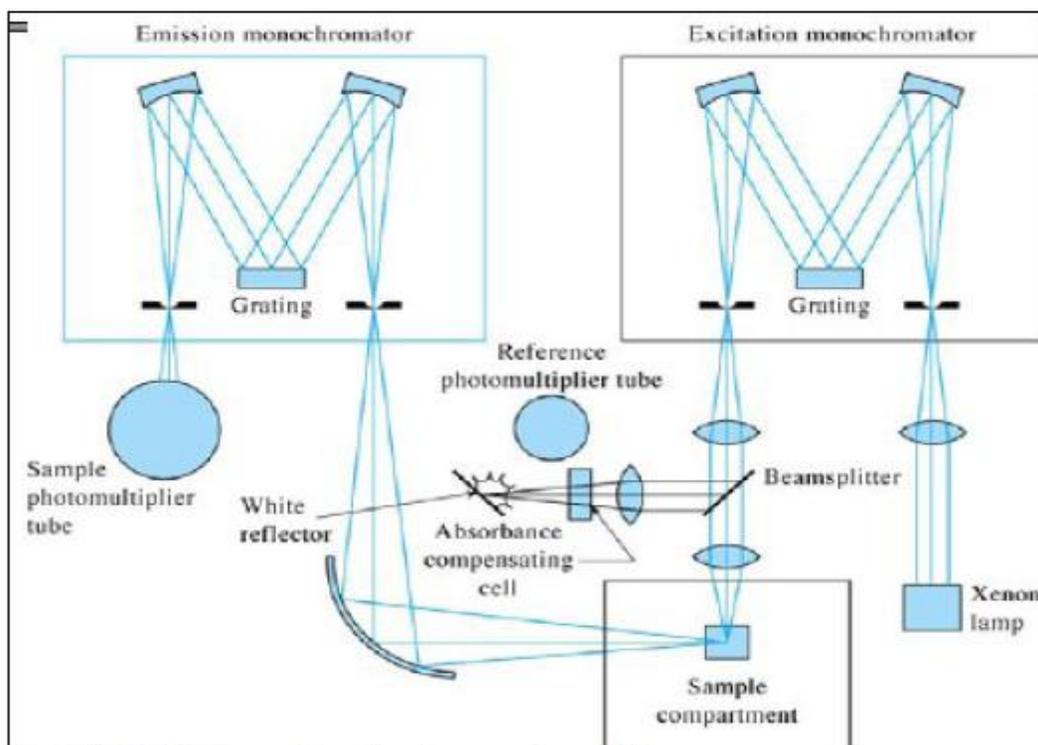
Figure 2.13: Generalized schematic diagram of fluorescence spectrometer instrumentation.
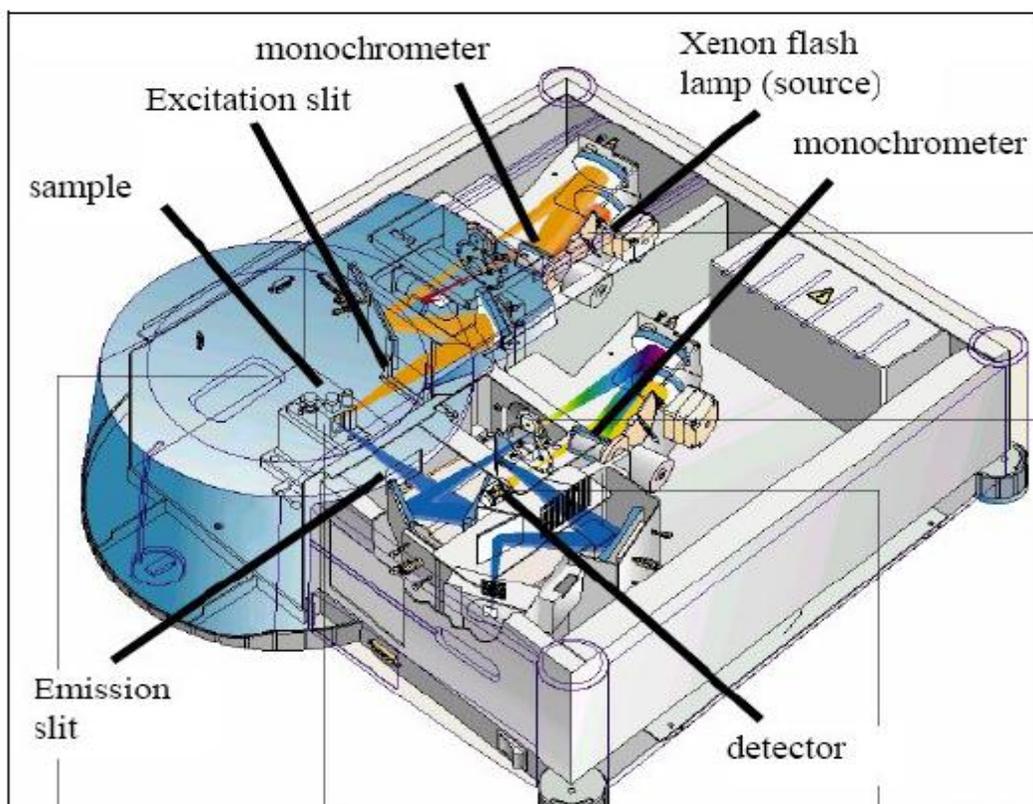
Figure 2.14: Schematic representation of the Cary Eclipse Fluorescence Spectrophotometer.

Figure 2.15: Cary Eclipse fluorescence spectrophotometer.

2.2.7. Thermoluminescence spectroscopy (TL)

Thermoluminescence is the thermally stimulated emission of light from an insulator or a semiconductor following the previous absorption of energy from ionizing radiation. The thermoluminescence process can be understood in terms of the band structure model of insulators. In a pure insulator there are two relevant energy bands: (i) an almost completely filled valence band and (ii) an almost empty conduction band. The two energy bands are separated by a forbidden gap, which means that between these two bands there are no electronic energy levels. Transitions of electrons between the valence band and the conduction band are allowed and they produce "free" electrons in the conduction band and "free" holes in the valence band. The energy difference between the two bands is denoted by the band-gap energy Eg [14]. The block diagram of the experimental setup of thermoluminescence (TL) is shown in figure 2.16. Thermoluminescence Reader (Integral-Pc Based) Nucleonix TL 1009I shown in figure 2.17 from University of the Free State, QwaQwa Campus was used in this study.
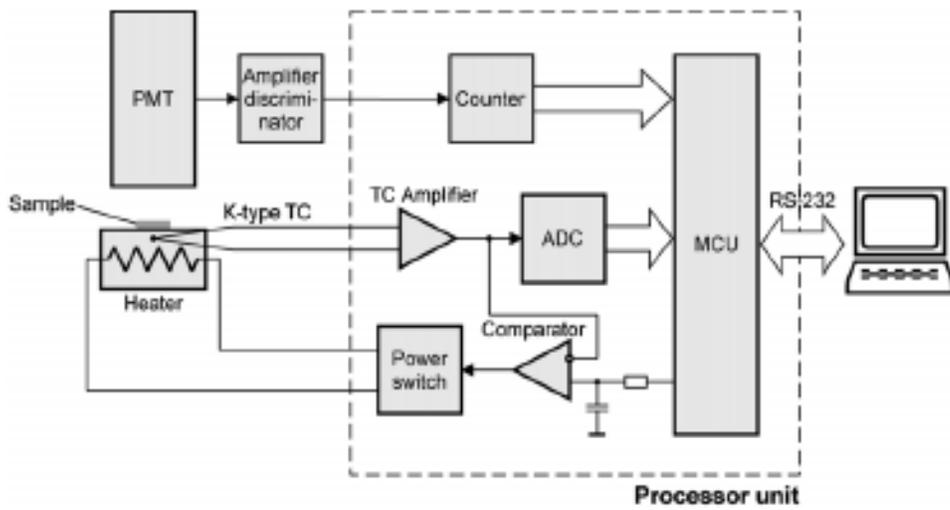
Figure 2.16: Block diagram of the experimental setup of TL [15].

Figure 2.17: Thermoluminescence Reader (Integral-Pc Based) Nucleonix TL 1009.

References

[1] B.M Mothudi, O. M Ntwaeaborwa and H. C Swart, PhD. Dissertation, University of the Free State, South Africa, (2009)

[2] O.M Ntwaeaborwa, R. E Kroon and H. C Swart, PhD. Dissertation, University of the Free State, South Africa, (2006)

[3] http://www.eserc.stonybrook.edu/ProjectJava/Bragg/ [17 Oct 2011]

[4] http://en.wikipedia.org/wiki/Bragg's_law [17 Oct 2011]

[5] http://serc.carleton.edu/research_education/geochemsheets/techniques/SEM.html [15 Sep 2011]

[6] http://www.purdue.edu/rem/rs/sem.htm [15 Sep 2011]

[7] http://www.siliconfareast.com/FTIR.htm [14 Sep 2011]

[8] http://mmrc.caltech.edu/FTIR/FTIRintro.pdf [14 Sep 2011]

[9] http://en.wikipedia.org/wiki/Fourier_transform_infrared_spectroscopy [20 Sep 2011]

[10] http://minyos.its.rmit.edu.au/~rcmfa/FTIR/images/spotlight.JPG [20 Sep 2011]

[11] J.J Dolo, F. B Dejene, O. M Ntwaeaborwa and H. C Swart, PhD. Dissertation, University of the Free State, South Africa, (2011)

[12] http://www.casaxps.com/help_manual/XPSInformation/XPSInstr.htm [14 Sep 2011]

[13] M.S Dhlamini, J. J Terblans and H. C Swart, PhD. Dissertation, University of the Free State, South Africa, (2008)

[14] http://www.wlu.ca/documents/25789/Cary_Eclipse.pdf [15 Sep 2011]

[15] http://dissertations.ub.rug.nl/FILES/faculties/science/2008/h.j.van.es/02-c2.pdf [14 Sep 2011]

CHAPTER 3

SYNTHESIS AND CHARACTERIZATION OF BaAl$_2$O$_4$:Eu^{2+} CO-DOPED WITH DIFFERENT RARE EARTH IONS

3.1: Introduction

Today, trivalent rare earths (RE) are used extensively to prepare luminescent materials (phosphors) that can be excited using any kind of energy as the excitation source. These materials are prepared by incorporating the Re^{3+} ions as dopants in different host matrices [1]. Example of such host matrices are the one represented by the general formula MAl$_2$O$_4$ (M= Ba^{2+}, Sr^{2+}, Ca^{2+}, or Mg^{2+}), which are widely used as host for Eu^{2+}-RE to prepare long afterglow (persistence luminescent) phosphors for a variety of applications in lighting.

Although extensive studies have been conducted in such materials, barium aluminate (BaAl$_2$O$_4$) co-doped with Eu^{2+} and other rare-earths (such as Dy^{3+}) has been studied only infrequently even though it shows persistence luminescence. The reason may be due to the rather complicated structural chemistry of the MAl$_2$O$_4$ host as well as the considerable size mismatch between the Ba^{2+} metal ion and the light emitting dopant (Eu^{2+}) ion. This is known to affect the luminescence efficiency of the Eu^{2+} doped BaAl$_2$O$_4$ when compared to other metal ions such as Ca^{2+} and Sr^{2+} [2].

3.2: Experimental procedure

The powder samples of Ba$_{0.96}$Al$_2$O$_4$:Eu^{2+}$_{0.02}$;RE$_{0.02}$ (RE = Dy^{3+}, Nd^{3+}, Gd^{3+}, Sm^{3+},Ce^{3+}, Er^{3+}, Pr^{3+} and Tb^{3+}) were synthesized using the combustion method. The following precursors: barium

nitrate [$Ba(NO_3)_3.4H_2O$], aluminium nitrate [$Al(NO_3)_2.9H_2O$], europium nitrate [$Eu(NO_3)_3.H_2O$], separately, with dysprosium nitrate [$Dy(NO_3)_3.5H_2O$], neodymium nitrate [$Nd(NO_3)_3.5H_2O$], gadolinium nitrate [$Gd(NO_3)_3.6H_2O$], samarium nitrate [$Sm(NO_3)_3.H_2O$], cerium nitrate [$CeN_3O_9.6H_2O$], erbium nitrate [$Er(NO_3)_3.5H_2O$], praseodymium nitrate [$Pr(NO_3)_3.6H_2O$], terbium nitrate [$Tb(NO_3)_3.H_2O$] and urea [$CO(NH_2)_2$], all in analytical purity, were weighed according to their stoichiometry. The precursors for each phosphor powder were mixed and milled in a mortar using pestle, and a thick white paste was formed from water of crystallization present on metal nitrates.

The paste from each mixture was then heated in a muffle furnace at an initiating combustion temperature of 600^oC. The paste melted under wet dehydration, and finally decomposed with the evolution of gases (oxides of nitrogen and ammonia). The mixture frothed and swelled, forming the foam that ruptured with a flame and glowed to incandescence. The entire combustion process was complete in less than 5 minutes. The voluminous combustion ashes of the powder samples of the $Ba_{0.96}Al_2O_4:Eu^{2+}_{0.02};RE_{0.02}$ (RE = Dy^{3+}, Nd^{3+}, Gd^{3+}, Sm^{3+}, Ce^{3+}, Er^{3+}, Pr^{3+} and Tb^{3+}) were ground into fine powders using the pestle and mortar. The powders were post annealed at 1000^oC for 3 hours in a muffle furnace.
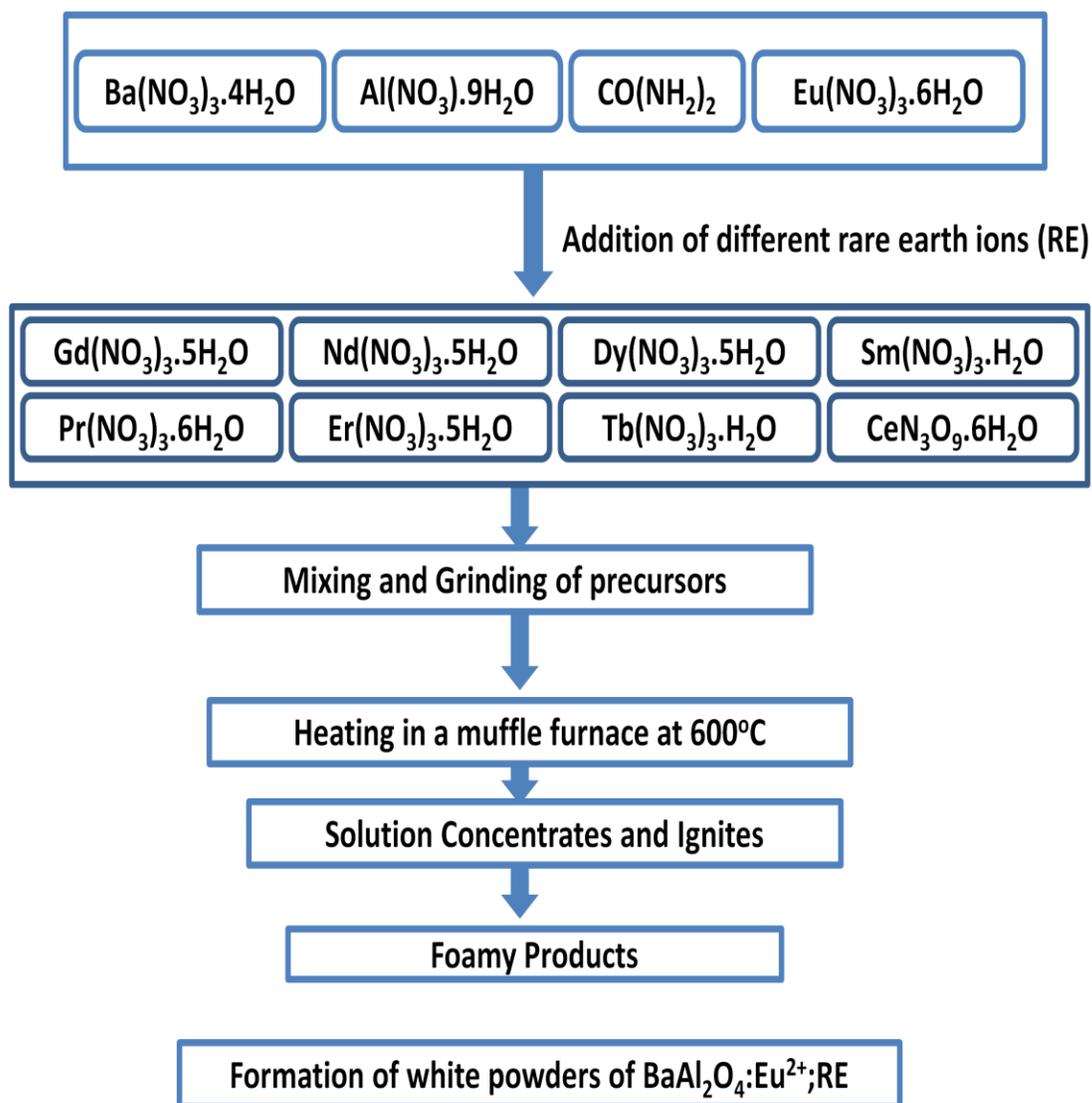
Figure 3.1: Flow chart for the preparation of $Ba_{0.96}Al_2O_4:Eu^{2+}_{0.02};RE_{0.02}$ (RE = Dy^{3+}, Nd^{3+}, Gd^{3+}, Sm^{3+}, Ce^{3+}, Er^{3+}, Pr^{3+} and Tb^{3+}) prepared at 600°C.

3.3: Results and discussion

3.3.1: Morphology and structure

The X-ray diffraction patterns of $Ba_{0.96}Al_2O_4:Eu^{2+}_{0.02};RE_{0.02}$ (RE = Dy^{3+}, Nd^{3+}, Gd^{3+}, Sm^{3+}, Ce^{3+}, Er^{3+}, Pr^{3+} and Tb^{3+}) prepared at the initiating temperature of 600^oC are shown in figure 3.2 and the annealed samples are shown in figure 3.3. The as-prepared samples showed the main diffraction peaks of the hexagonal structure of $BaAl_2O_4$, but there are additional peaks present (labeled with asterisk), which may be attributed to unreacted $Ba(NO_3)_2$ precursors or other impurity phases [3].
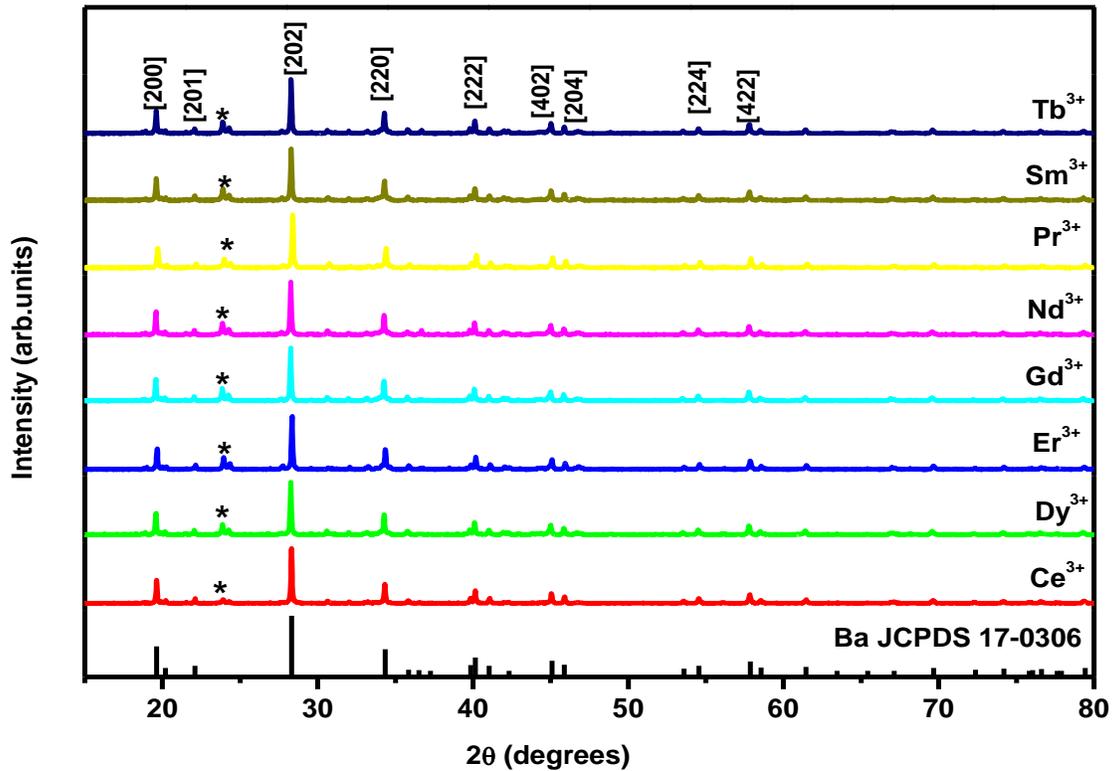
Figure 3.2: XRD patterns of the phosphor powders of: $Ba_{0.96}Al_2O_4:Eu^{2+}_{0.02};Re^{3+}_{0.02}$ (RE = Dy^{3+}, Nd^{3+}, Gd^{3+}, Sm^{3+}, Ce^{3+}, Er^{3+}, Pr^{3+} and Tb^{3+}) at an initiating temperature of 600^oC.

The results show improvements in crystallinity and phase for the post-annealed phosphor samples and the main diffraction peaks index well with the card file (JCPDS: 17-0306). The XRD data clearly shows that the small concentration of co-dopants does not affect the crystal structure of the host. Qui et al [4] also stated that the small amount of doped rare earth ions has virtually no effect on the phase structure. The crystal sizes for the as-prepared phosphor samples were calculated using the Debye-Scherer's equation: $D = \dfrac{0.9\lambda}{\beta \cos\theta}$, where D = diameter of crystal particle, β = broadening of diffraction line measured at half its maximum intensity in radians, θ is the Bragg angle and λ is the x-ray wavelength [5]. The results shown in table 3.1 where calculated using $Ba_{0.96}Al_2O_4:Eu^{2+}_{0.02};Nd^{3+}_{0.02}$ phosphor powder. The average crystal size for the phosphor powder was found to be 104 nm.
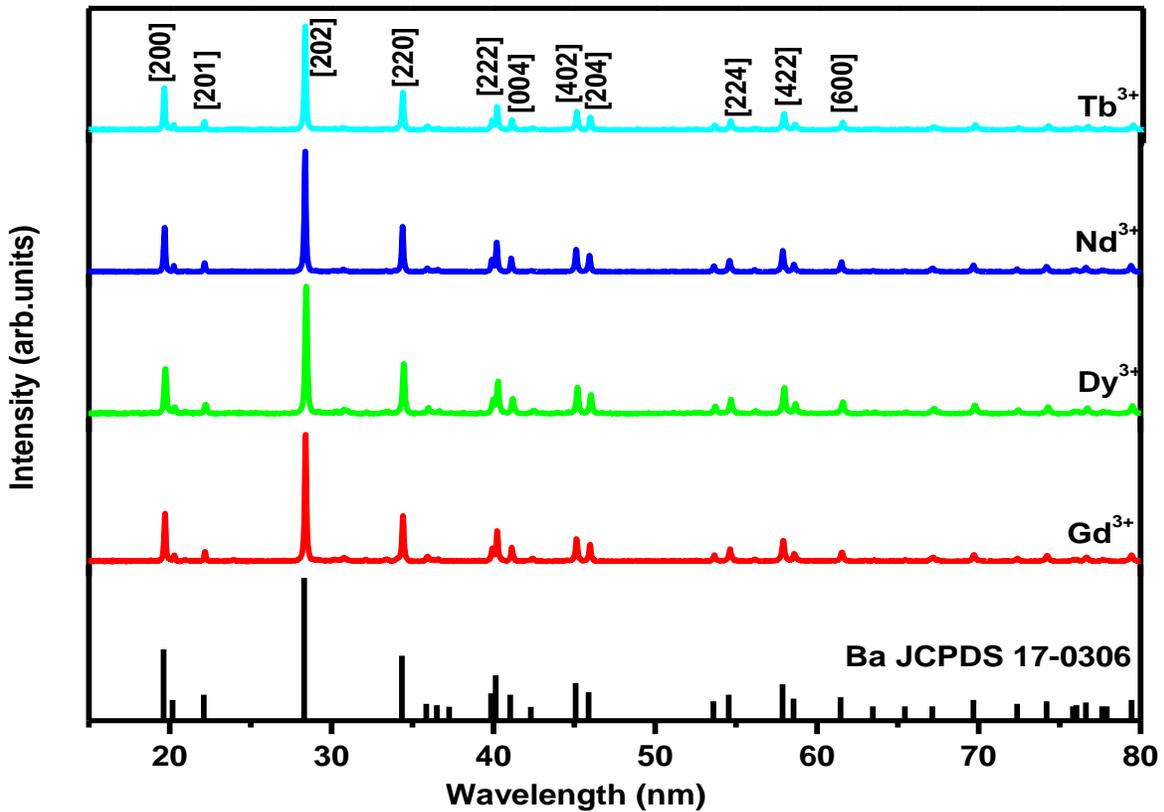
Figure 3.3: $Ba_{0.96}Al_2O_4:Eu^{2+}_{0.02};Re^{3+}_{0.02}$ (RE = Dy^{3+}, Nd^{3+}, Gd^{3+}, and Tb^{3+}) annealed at 1000°C for 3 hours.

Table 3.1: Calculated average crystal size for $Ba_{0.96}Al_2O_4:Eu^{2+}_{0.02};Nd^{3+}_{0.02}$ phosphor powder.

Peak	2θ (degrees)	FWHM (β)	D (nm)
[202]	28.264	0.0784	101
[220]	34.275	0.0795	100
[201]	22.052	0.0659	121
[200]	19.578	0.0706	104
[222]	40.100	0.0831	96

D(average) = 104 nm
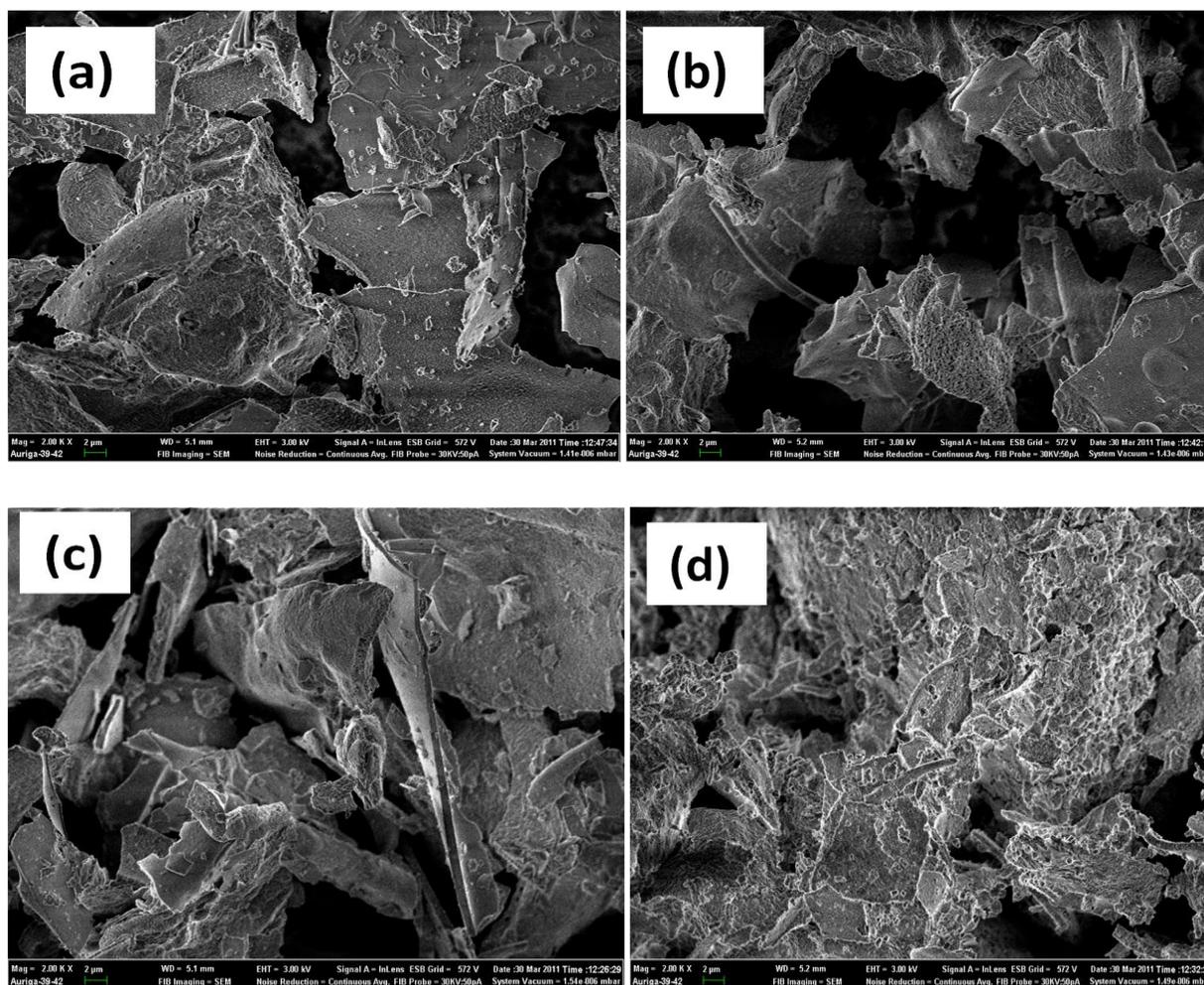
Figure 3.4: SEM images of: $Ba_{0.96}Al_2O_4:Eu^{2+}_{0.02};Dy^{3+}_{0.02}$ (a) as-prepared , (b) annealed at 1000°C and $Ba_{0.96}Al_2O_4:Eu^{2+}_{0.02};Nd^{3+}$ (d) as-prepared , (d) annealed at 1000°C.

Scanning Electron Microscopy (SEM) study was carried out to investigate the surface morphology and the crystallite size of the synthesized phosphor powders. Figure 3.4 shows the SEM micrographs of $Ba_{0.96}Al_2O_4:Eu^{2+}_{0.02};Dy^{3+}_{0.02}$ prepared at 600°C (a) and annealed at 1000°C for 3 hours (b), and $Ba_{0.96}Al_2O_4:Eu^{2+}_{0.02};Nd^{3+}_{0.02}$ prepared at 600°C (c) and annealed at 1000°C for 3 hours (d). The SEM images of the phosphor samples show particles with an inherent nature of combustion morphology, i.e. agglomerated irregular plate-like particles. There are noticeable voids and pores on the surface resulting from escaping gases during the combustion process.
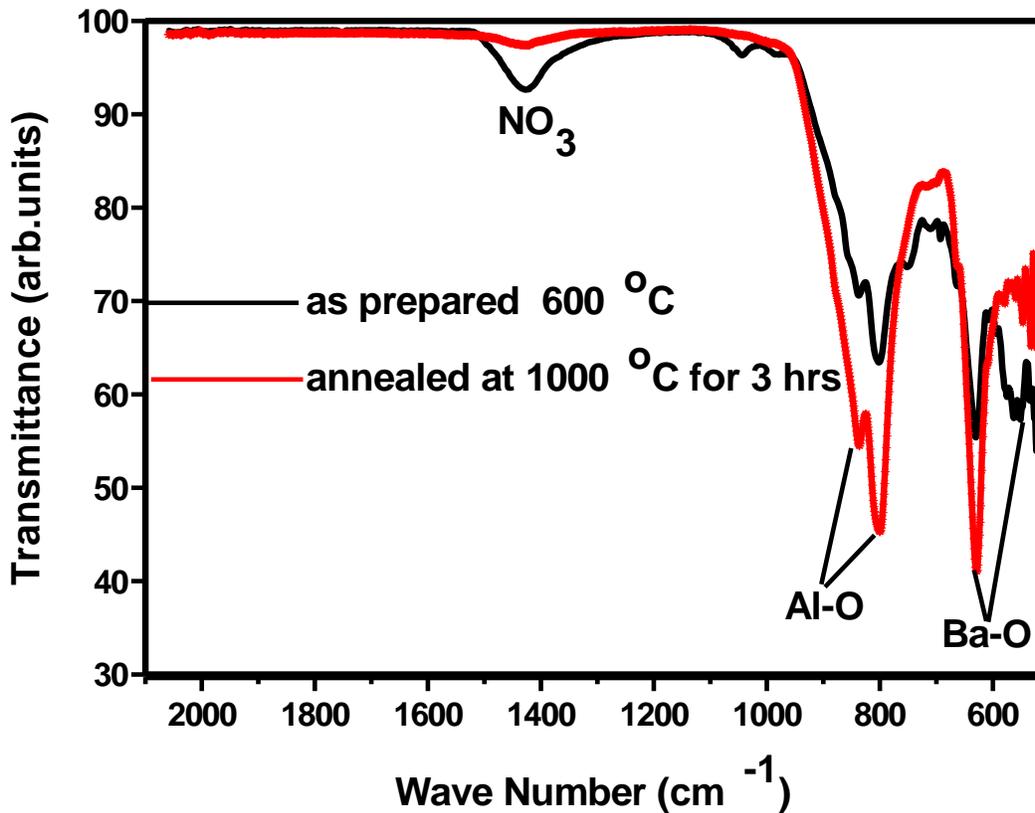
Figure 3.5: FTIR spectra of $Ba_{0.96}Al_2O_4:Eu^{2+}_{0.02};Dy^{3+}_{0.02}$ prepared at 600°C and annealed at 1000°C for 3 hours.

Figure 3.5 shows the FT-IR spectra of $Ba_{0.96}Al_2O_4:Eu^{2+}_{0.02};Dy^{3+}_{0.02}$ prepared at 600°C and annealed at 1000°C for 3 hours [6]. The absorption bands at 1430 cm^{-1} shown in some of the

samples correspond to the NO_3, which confirms the presence of some of the starting materials such as metal nitrates [$(BaNO_3)_3.4H_2O$)], which did not decompose completely during the reaction. This band is prominent in the phosphor powder prepared at 600°C, after annealing the sample at 1000°C for 3 hours the band seems to decrease. The same results were reported by Stefani et al. [11], for $BaAl_2O_4$:Eu^{2+};Dy^{3+} phosphor samples prepared by solid state reaction. The metal oxygen stretching modes in the range of 500-1000 cm^{-1} as shown in figure 3.4 can be associated with vibrations of Al-O, Ba-O and Ba-O-Al bonds [7]. The FT-IR results for the phosphor sample prepared at 600°C confirm the observations found from the X-ray diffraction patterns in figure 3.2 shows that the heating temperature of 600°C is definitely too low to decompose $(BaNO_3)_2$. In this study the samples annealed at a higher temperature (1000°C) show the fully developed and intense bands which confirm the formation of the $BaAl_2O_4$ phase.

3.3.2: Luminescence studies
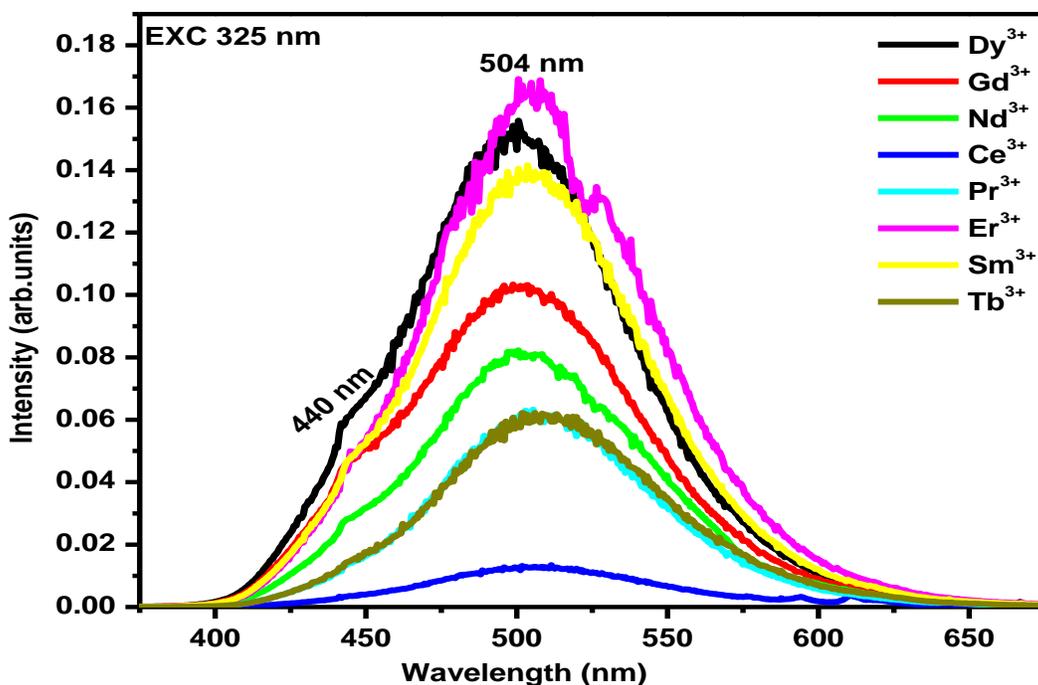
Figure 3.6: Emission spectra of $Ba_{0.96}Al_2O_4$:$Eu^{2+}_{0.02}$;$Re^{3+}_{0.02}$ (RE = Dy^{3+}, Nd^{3+}, Gd^{3+}, Sm^{3+}, Ce^{3+}, Er^{3+}, Pr^{3+} and Tb^{3+}) phosphor powders at an initiating temperature of 600°C.

The PL emission spectra of $Ba_{0.96}Al_2O_4:Eu^{2+}_{0.02};RE_{0.02}$ (RE = Dy^{3+}, Nd^{3+}, Gd^{3+}, Sm^{3+}, Ce^{3+}, Er^{3+}, Pr^{3+} and Tb^{3+}) phosphor powders prepared at an initiating temperature of 600^oC by combustion method are shown in figure 3.6. All the samples were excited by a 325 nm He-Cd laser. The highest intensity was observed from $BaAl_2O_4:Eu^{2+}$ co-doped with Er^{3+} and the least intensity was observed from Ce^{3+} co-doped sample. The phosphor samples show the broad emission band with a maximum at ~504 nm and a shoulder at 440 nm in other samples. This blue-green emissions observed in $BaAl_2O_4:Eu^{2+}$ co-doped phosphors powders are due to the $4f^5 5d^1$-$4f^7$ transitions of Eu^{2+}.
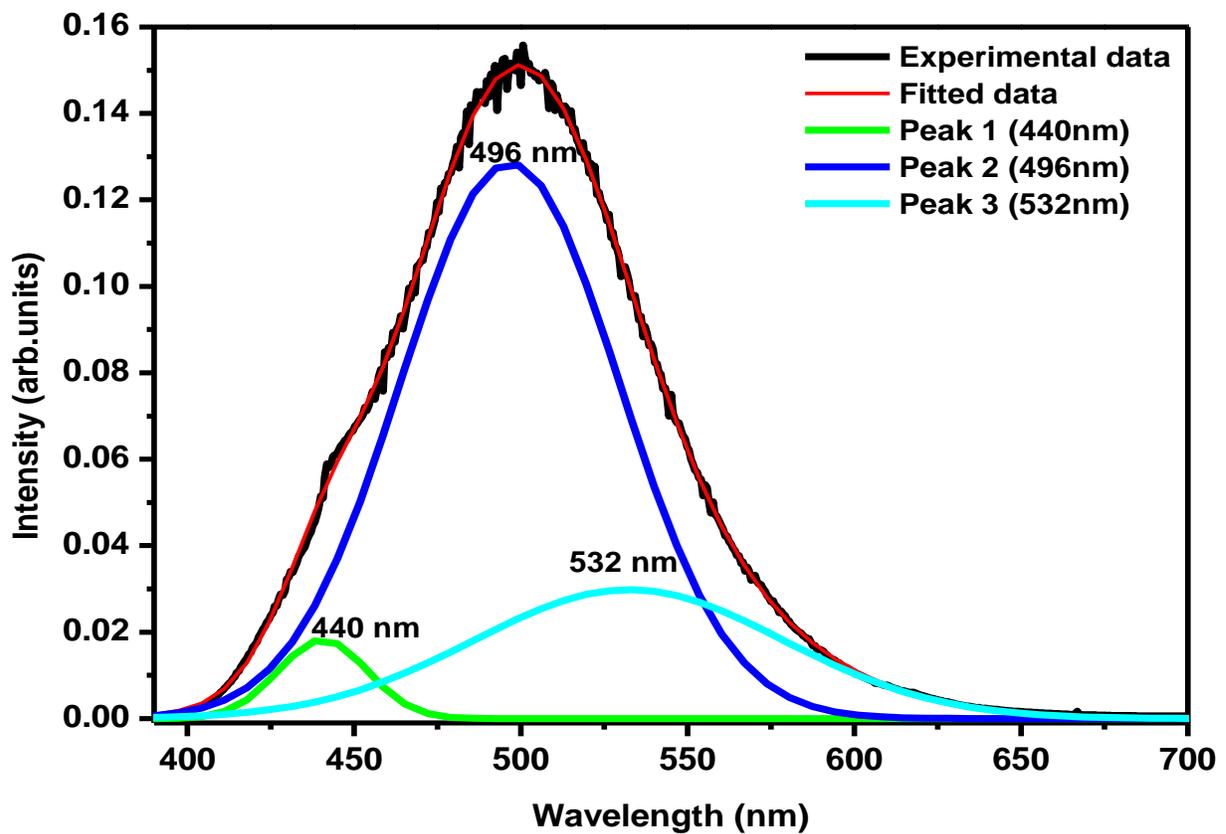
Figure 3.7: A Gaussian Fit for the emission spectra of the $Ba_{0.96}Al_2O_4:Eu^{2+}_{0.02};Dy^{3+}_{0.02}$ phosphor powder at an initiating temperature of 600^oC.

Stefani et al. [2] prepared $BaAl_2O_4:Eu^{2+};Dy^{3+}$ by solid state reaction, and reported that the two maxima peaks observed at 435 nm and 504 nm were due to the transitions from the lowest ^2D of the excited state to the excited state $4f^6 5d^1$ configuration to the ground $^8S_{7/2}$ level in the $4f^7$ configuration of the Eu^{2+}. These two peaks might be coming from the two Ba^{2+} sites in the

BaAl$_2$O$_4$ structure. Peng et al. [8], reported that these two different barium sites Ba(1) and Ba(2) are positioned on 6c and 2a sites coordinated by nine oxygen ions with average Ba-O distances of 2.97Å for Ba(1) and 2.89 Å for Ba(2), respectively. Ba(1) sites occurs three times more frequently than Ba(2). Figure 3.7 shows a Gaussian Fit for the emission spectra of Ba$_{0.96}$Al$_2$O$_4$:Eu$^{2+}_{0.02}$;Dy$^{3+}_{0.02}$ phosphor powder at an initiating temperature of 600°C. The band was fitted into three peaks at 440 nm, 496 nm and 532 nm. The splitting of 5d-excitation level of Eu^{2+} ion in solid state compounds depends strongly on the strength of crystal field around Eu^{2+} ion. When the crystal environments are analogous, the Eu^{2+} center with shorter Eu^{2+}-O^2 distance will give a longer emission [8]. Therefore from the fitted emission spectra, the 440 nm emission might be from the Eu^{2+} ion on Ba(1) site and the 496 nm and 532 nm from the Eu^{2+} ion on the Ba(2) site. Peng et al. [8] also reported that the assignment of Eu^{2+} on the barium sites can also be explained by means of preferential orientation of d orbitals of Eu^{2+}. The data for the fitted spectrum are shown in table 3.2.

Table 3.2: Fitting parameters of the PL emission spectrum Ba$_{0.96}$Al$_2$O$_4$:Eu$^{2+}_{0.02}$;Dy$^{3+}_{0.02}$ phosphor powder.

Peak	Area	Center (nm)	width	Height
1	0.6145	440	27	0.018289
2	10.552	496	66	0.128440
3	3.4757	532	93	0.029831

Shown in figure 3.8 is the emission spectra of Ba$_{0.96}$Al$_2$O$_4$:Eu$^{2+}_{0.02}$;RE$_{0.02}$ (RE= Dy^{3+}, Nd^{3+}, Gd^{3+}, and Tb^{3+}) phosphor powders annealed at 1000°C for 3 hours. The annealing temperature did not show any effect in the emission peak of the phosphor powders. The phosphor powder shows a broad emission band at 502 nm. The intensity of the Ba$_{0.96}$Al$_2$O$_4$:Eu$^{2+}_{0.02}$;Nd$^{3+}_{0.02}$ phosphor powder was increased after annealing at 1000°C for 3 hours. The blue-green emission observed in most of the phosphors confirms that Eu^{2+} is the emitting centre. Decay curves of Ba$_{0.96}$Al$_2$O$_4$:Eu$^{2+}_{0.02}$;RE$_{0.02}$ (RE = Dy^{3+}, Nd^{3+}, Gd^{3+}, Ce^{3+} and Er^{3+}) phosphor powders prepared at an initiating temperature of 600°C are shown in figure 3.9. The luminescent decay curves were measured after irradiating the phosphor samples with the 325 nm UV light for 2 minutes at room temperature. BaAl$_2$O$_4$:Eu^{2+} co-doped with Nd^{3+} and Dy^{3+} rare earth ions exhibited relatively long

afterglow emission compared to other samples. The afterglow of Nd^{3+} co-doping was, however, longer than that of Dy^{3+} co-doping.
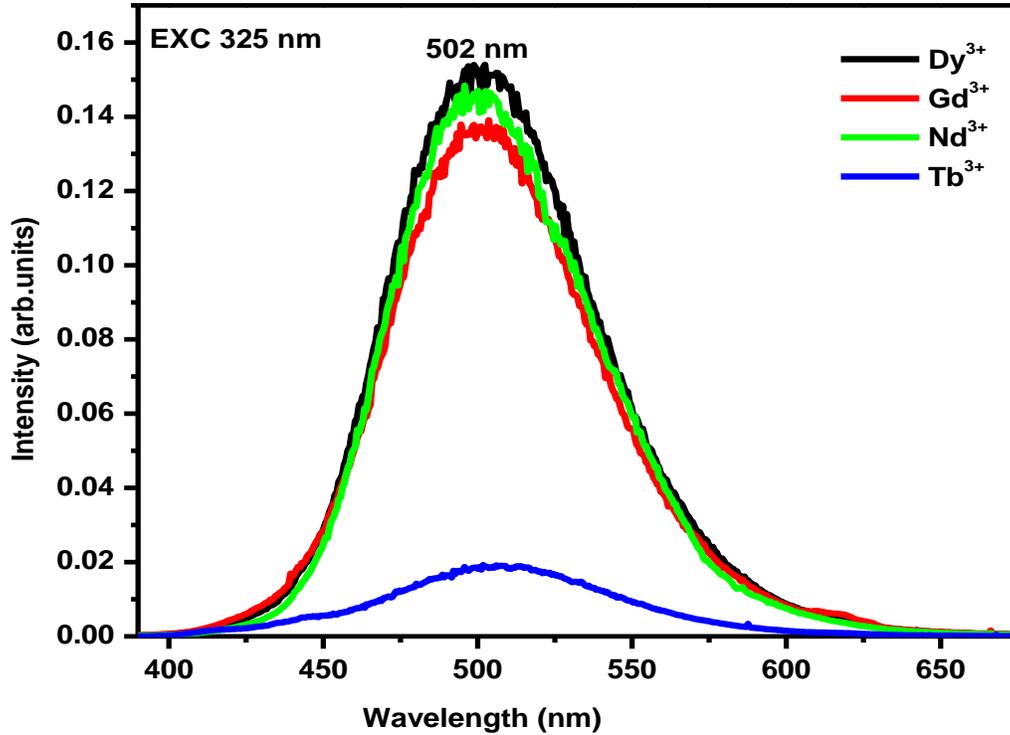
Figure 3.8: Emission spectra of $Ba_{0.96}Al_2O_4:Eu^{2+}_{0.02};RE_{0.02}$ (RE = Dy^{3+}, Nd^{3+}, Gd^{3+}, and Tb^{3+}) phosphor powders annealed at 1000^oC for 3 hours.

The long afterglow of Nd^{3+} and Dy^{3+} co-doping in $MAl_2O_4:Eu^{2+}$ was also observed by Katsumata et al [9]. The decay curves in figure 3.9 were fitted using the third order exponential decay equation:

$$I = A_1 \exp(-{}^t\!/_{\tau_1}) + A_2 \exp(-{}^t\!/_{\tau_2}) + A_3 \exp(-{}^t\!/_{\tau_3}) \tag{1}$$

Where I is the phosphorescence intensity at any time t after switching off the excitation source, A_1, A_2 and A_3 are constants and τ_1, τ_2 and τ_3 are decay times for the exponential components

respectively. Fitted curve of $Ba_{0.96}Al_2O_4:Eu^{2+}_{0.02}$; $Nd^{3+}_{0.02}$ phosphor powders prepared at 600^oC is shown in figure 3.10. The decay parameters for the fitted curves are listed in table 3.3.
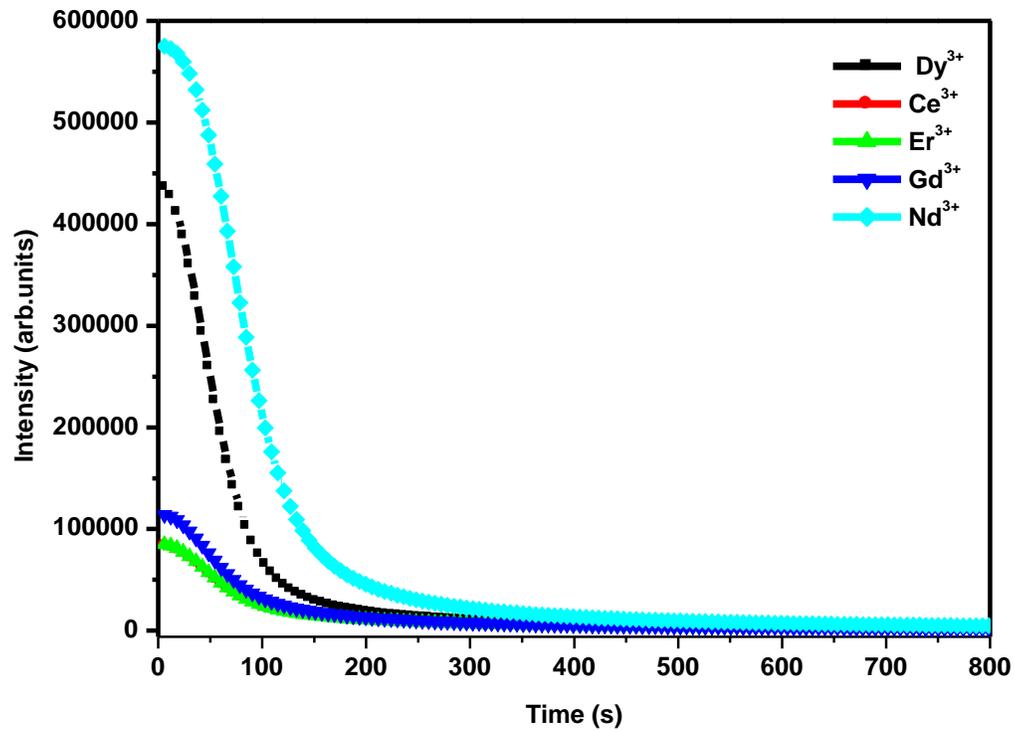
Figure 3.9: Decay curves of $Ba_{0.96}Al_2O_4:Eu^{2+}_{0.02}$; $RE_{0.02}$ phosphor powders prepared at 600^oC.
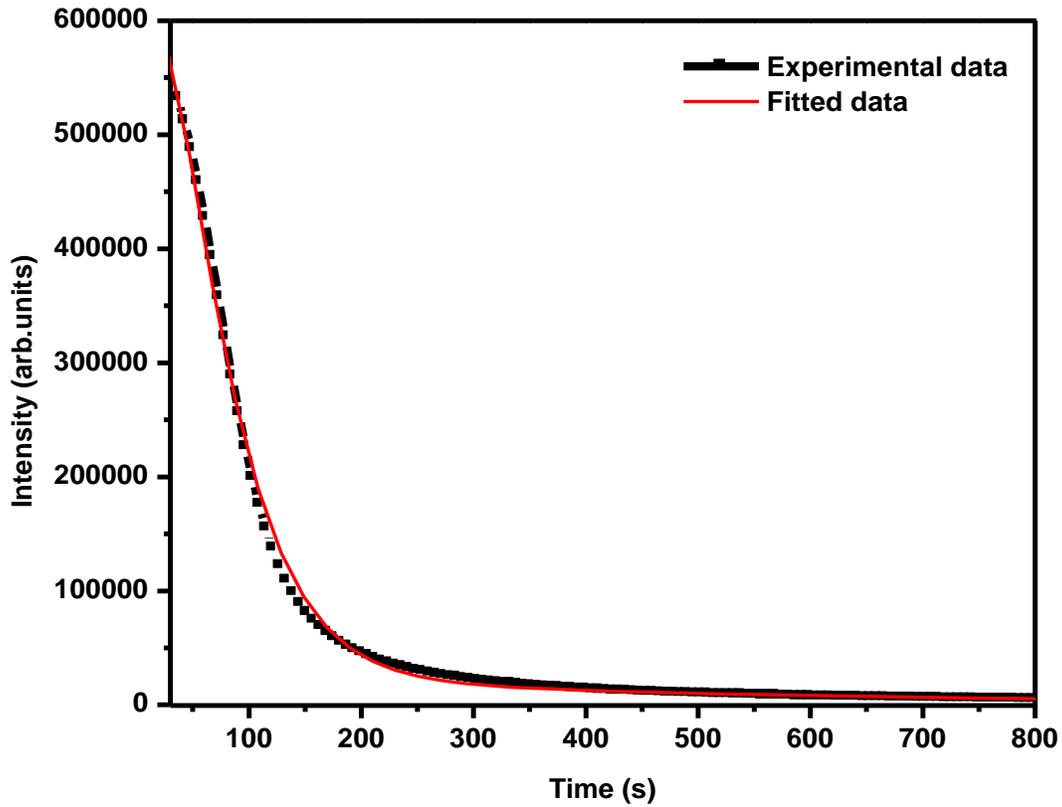
Figure 3.10: Fitted curve of $Ba_{0.96}Al_2O_4$:$Eu^{2+}_{0.02}$; $Nd^{3+}_{0.02}$ phosphor   powders prepared at 600^oC.

Table 3.3: decay constants of $Ba_{0.96}Al_2O_4$:$Eu^{2+}_{0.02}$; $RE_{0.02}$ phosphor powders prepared at 600^oC.

	τ_1 (sec)	τ_2 (sec)	τ_3 (sec)
Dy^{3+}	21 ± 2	30 ± 2	375 ± 20
Nd^{3+}	31 ± 5	43 ± 5	469 ± 65
Gd^{3+}	17 ± 1	43 ± 1	386 ± 9
Ce^{3+}	17 ± 1	43 ± 1	428 ± 9
Er^{3+}	17 ± 1	45 ± 1	427 ± 9

3.3.3: Thermoluminescence studies

In order to further investigate the significant effect of the rare earth (RE) co-doping on the intensity of the persistent luminescence of the $MAl_2O_4:Eu^{2+}$ materials, the measurement of the thermoluminescence glow curves of these materials was carried out. Thermoluminescence glow curves of $Ba_{0.96}Al_2O_4:Eu^{2+}_{0.02}$; $RE_{0.02}$ (RE= Dy^{3+}, Er^{3+}, Ce^{3+}, Gd^{3+} and Nd^{3+}) prepared at an initiating temperature of 600^oC are shown in figure 3.11.
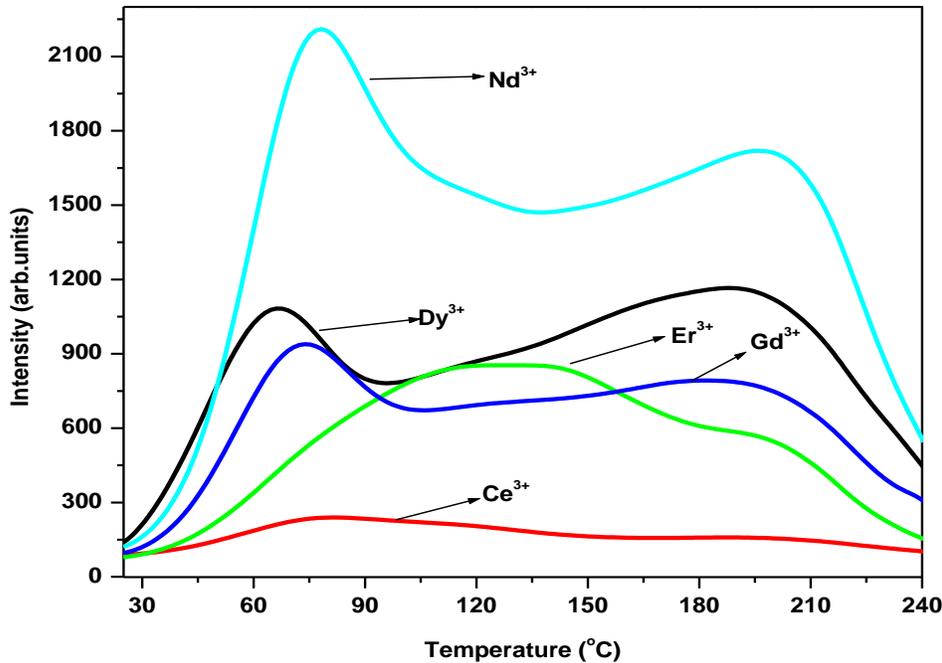
Figure 3.11: Thermoluminescence glow curves of $Ba_{0.96}Al_2O_4:Eu^{2+}_{0.02}$; $RE_{0.02}$ (RE = Dy^{3+}, Er^{3+}, Ce^{3+}, Gd^{3+} and Nd^{3+}) phosphor powders prepared at an initiating temperature of 600^oC.

In case of Nd^{3+}, Gd^{3+} and Dy^{3+}, co-dopant, two main TL peaks were observed at 78^oC and 197^oC, 72^oC and 191^oC, and 66^oC and 193^oC respectively. The thermoluminescence data reveals the presence of two different trapping levels in $Ba_{0.96}Al_2O_4:Eu^{2+}_{0.02}$; $RE_{0.02}$ (RE = Dy^{3+}, Gd^{3+} and Nd^{3+}). Due to the formation of suitable trapping levels, afterglow was observed. In case of Er^{3+}

and Ce^{3+} co-dopants, only one TL peak was observed at $125^{o}C$ and $81^{o}C$ respectively. Note that the decay is primarily attributed to trapping and de-trapping of charge carriers (electrons) captured in various traps formed by incorporated co-dopants. The length of the afterglow (phosphorescence) is proportional to the depth of the traps, i.e. the deeper the trap the longer the phosphorescence. The Nd^{3+} traps measurements by thermoluminescence (TL) spectroscopy were analyzed and the data is shown in figure 3.12. The broad nature of the experimental glow curves observed in the present case may be attributed to the overlap of various peaks having a close distribution of their trap depths and therefore choice of glow curve deconvolution (GCD), typically suitable for quasi-continuous distribution of traps, becomes imperative.
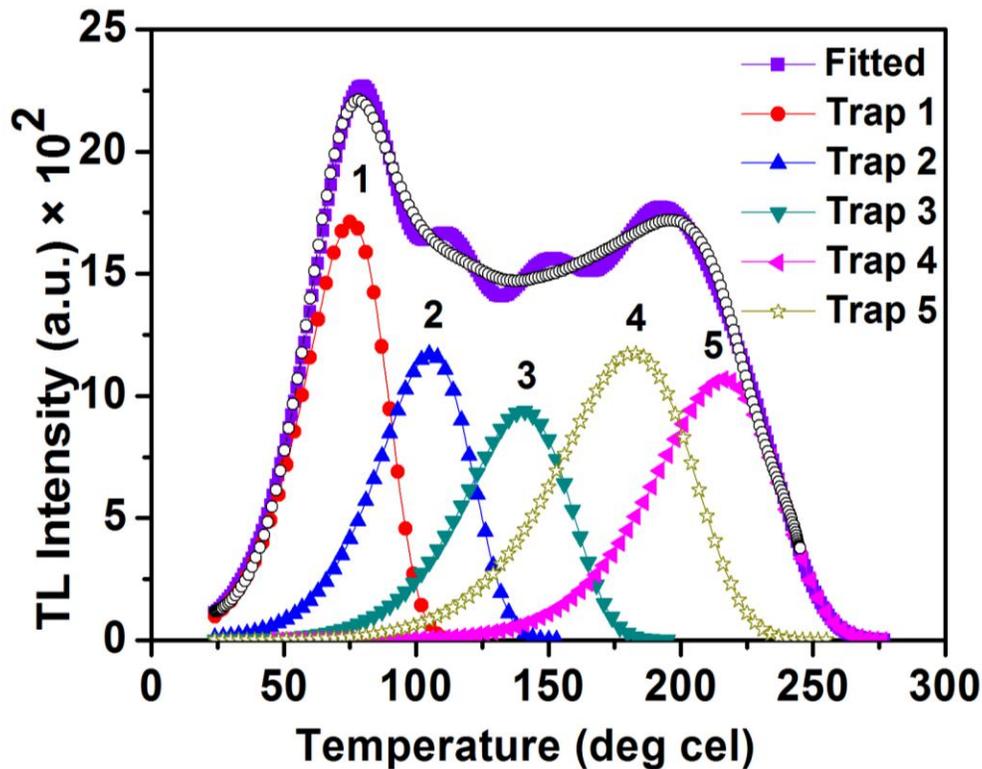
Figure 3.12: Deconvoluted TL glow curve of the as prepared $Ba_{0.96}Al_2O_4:Eu^{2+}{}_{0.02};Nd^{3+}{}_{0.02}$ powder.

The simplest and physically relevance of all GCD functions is the first-order kinetic model which was used to deconvolute the glow peaks of the Nd^{3+} co-doped sample shown in figure 3.12. According to this model, the TL intensity is expressed as:

$$I(T) = I_M \, \exp\left[1 + \frac{E}{kT} \times \frac{T - T_M}{T_M} - \frac{T^2}{T_M^2} \times (1 - \Delta_M) \exp\left(\frac{E}{kT} \times \frac{T - T_M}{T_M}\right) - \Delta_M\right] \qquad (2)$$

Where, $\Delta_M = \dfrac{2kT_M}{E}$, I_M and T_M are the TL intensity and temperature at the glow peak maximum respectively, E is the activation energy (eV), and k is the Boltzmann constant. The trapping parameters computed this way are listed in Table 3.4. The frequency factor (s) of various deconvoluted peaks (as shown in table 3.4) was calculated using the heating rate $\beta = 10$ deg/sec according to equation 3:

$$s = \frac{\beta E}{kT_M^{\ 2}} \exp\left(\frac{E}{kT_M}\right) \qquad (3)$$

Table 3.4: The kinetic parameters of the as prepared $Ba_{0.96}Al_2O_4{:}Eu^{2+}_{\ 0.02}{;}Nd^{3+}_{\ 0.02}$ powder derived using the CGCD procedure.

Trap	Max. Temp. T_m (°C)	Trap Depth E (eV)	Concentration $n_0 \times 10^3$ (cm^{-3})	Frequency factor s (sec^{-1})
Trap 1	74.3	0.65	60.8	1.6×10^9
Trap 2	105.5	0.68	47.5	6.2×10^8
Trap 3	140.4	0.71	43.4	2.1×10^8
Trap 4	182.1	0.68	68.1	1.2×10^7
Trap 5	216.3	0.85	57.8	2.3×10^8

The goodness of fit or figure of merit (FOM) obtained using the relation

$$\sum \frac{\left| TL_{\text{experimental}} - TL_{\text{fit}} \right|}{\sum TL_{\text{fit}}}$$ for the parameters listed in table 2 is 2.2 %. The frequency factor

(in sec^{-1}), which is related to vibrational frequencies of the trapped charge carrier, the effective density of states in the delocalized band and the free carrier thermal velocity, derived for various deconvoluted peaks falls in the range between 10^7-10^9/sec. and is close to the earlier observations [11-12] for aluminate phosphors. The derived lower values of s may be due to the typical localized transitions where a recombination occurs between spatially localized recombination centre and traps without the involvement of transportation bands (conduction or valence band) and its relative probability may then be related to an extent of the wave function overlap between the trap and recombination centre.

3.4: Conclusion

The phosphor powders of $Ba_{0.96}Al_2O_4:Eu^{2+}_{0.02}$; $RE_{0.02}$ (RE = Dy^{3+}, Nd^{3+}, Gd^{3+}, Sm^{3+}, Ce^{3+}, Er^{3+}, Pr^{3+} and Tb^{3+}) were successfully synthesized using the combustion method at an initiating temperature of 600^oC and were annealed at 1000^oC. The XRD results showed that the small amount of doped rare earth ions has virtually no effect on the phase structure. Post-preparation annealing did not affect the general properties of the phosphors. The blueish-green emission associated with the $4f^65d^1$-$4f^7$ transitions Eu^{2+} was observed at ~504 nm from all the samples with the maximum emission observed from the sample co-doped with Er^{3+}. The long afterglow ascribed to trapping and detrapping of charge carriers was observed from Dy^{3+} and Nd^{3+}. The traps of the Nd^{3+} co-doped sample, which exhibited the relatively longer afterglow, follow a quasi-continuous distribution as suggested from TL glow curve analysis.

References

[1] T. Aitasalo, P. Deren, J. Holsa, H. Jungner, J. C. Krupa, M. Lastusaari, J. Legendziewics J. Niittykoski and W. Strek, Journal of Solid State Chemistry **171** 114-122 (2003)

[2] R. Stefani, L.V.C. Rodrigues, C.A.A. Carvalho, M.C.F.C. Felinto, H.F. Brito, M. Lastusaari and J. Holsa, Optical Material **31** 1815-1818 (2009)

[3] B.M. Mothudi, O.M. Ntwaeaborwa, J.R. Botha, and H.C. Swart, Physica B **404** 22 4440-4444

[4] Z. Qui, U. Zhou, M. Lu, A. Zhang and Q. Ma, Acta Materialia **55** 2615 2620 (2007)

[5] B.D. Cullity, Element of x-ray diffraction (2nd edition) p284 (1978)

[6] N. Lakshminarasimhan, U.V. Varadaraju, Materials Research Bulletin **43** 2946-2953 (2008)

[7] S. Angappan, J. Berchmans, C.O. Augustin, Materials Letters **58** 2283-2289 (2004)

[8] M. Peng, G. Hong, Journal of Luminescence **127** 735-740 (2007)

[9] T. Katsumata, S. Toyomane, R. Sakai, S. Komuro, and T. Morikawa, Journal of the American Ceramic Society **89** 932-936 (2006)

[10] J. Holsa, H. Jungner, M. Lastusaari, and J. Niittykoski, Journal of Alloys and compounds **323-324** 326-330 (2001)

[11] S.K. Sharma, S.S. Pitale, M.M. Malik, M.S. Qureshi, and R. N. Dubey, Journal of Alloys and Compounds **482** 468-475 (2009)

[12] S.S. Pitale, S.K. Sharma, R.N. Dubey, M.S. Qureshi, M.M. Malik, Optical Materials **32** 461-468 (2010)

CHAPTER 4

EFFECT OF THE INITIATING TEMPERATURE ON THE STRUCTURAL AND LUMINESCENT PROPERTIES OF BaAl$_2$O$_4$:Eu^{2+};Nd^{3+};Gd^{3+}

4.1: Introduction

The alkaline earth aluminate, MAl$_2$O$_4$ (M= Ca, Sr, Ba) doped with Eu^{2+} are reported to show an intense photoluminescence in blue-green region [1, 2]. When co-doping with the second rare earth ion as a sensitizer, these phosphors exhibit a rapid initial decay from Eu^{2+} ion followed by long persistence. This effect can be explained based on the thermal activation of charge carriers from traps followed by the emission of Eu^{2+} [3]. Many researchers have mainly focused on preparing BaAl$_2$O$_4$:Eu^{2+};Dy^{3+} phosphors using different preparation methods [4, 5, 6]. In this study, BaAl$_2$O$_4$:Eu^{2+};Nd^{3+};Gd^{3+} was prepared using combustion method at different initiating temperatures ranging from 400°C to 1200°C.

4.2: Experimental Procedure

The powder phosphors were prepared by a combustion method at different initiating temperatures ranging from $400^{\circ}C$-$1200^{\circ}C$. The following precursors: Barium nitrate [$Ba(NO_3)_3.4H_2O$], Aluminium nitrate [$Al(NO_3)_2.9H_2O$], Europium nitrate [$Eu(NO_3)_3.6H_2O$], Neodymium nitrate [$Nd(NO_3)_3.5H_2O$], Gadolinium nitrate [$Gd(NO_3)_3.5H_2O$] and Urea [$CO(NH_2)_2$] all in analytical purity were weighed according to their stoichiometry to prepare the phosphor powders. The phosphor powders were prepared by a combustion method as illustrated by the flow chart shown in figure 4.1.
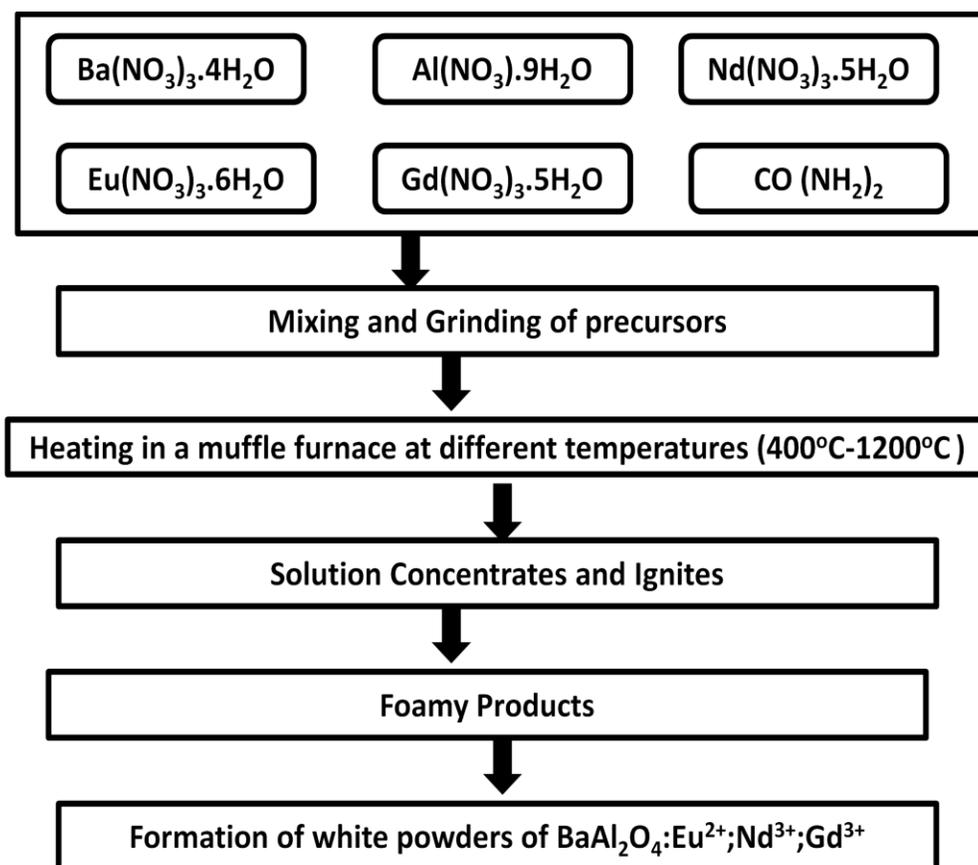
Figure 4.1: Flow chart for the preparation of BaAl$_2$O$_4$:Eu^{2+};Nd^{3+};Gd^{3+} prepared at different initiating temperature of 400°C-1200°C.

4.3: Results and Discussion

4.3.1: Morphology and chemical composition
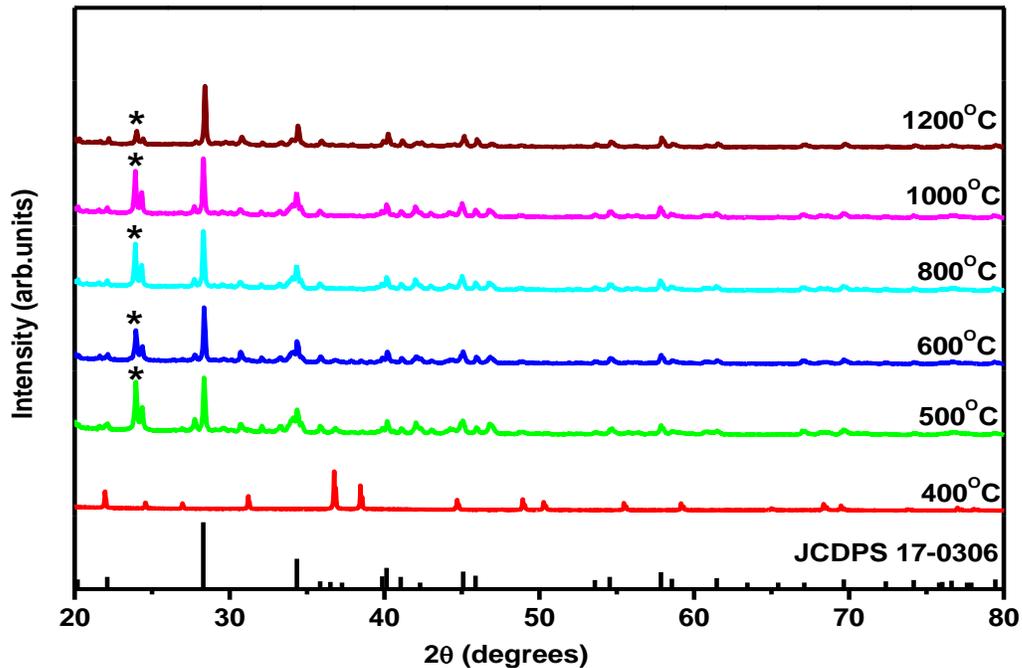
Figure 4.2: X-ray diffraction spectra of BaAl$_2$O$_4$:Eu^{2+};Nd^{3+};Gd^{3+} prepared at different initiating temperature.

Figure 4.2 shows the X-ray diffraction spectra of BaAl$_2$O$_4$:Eu^{2+};Nd^{3+};Gd^{3+} powders prepared at different initiating temperatures by combustion method. It is shown that at low temperature of 400°C, the structure of the phosphor powder correspond to the cubic structure of Ba(NO$_3$)$_2$ according to the JCDPS card file no: 76-1376. With the increase in temperature (500°C-1200°C), the structure of the phosphor samples changes to the hexagonal BaAl$_2$O$_4$ structure with some impurities (marked with an asterisk) and this correspond to the JCDPS card file no: 17-0306. These impurities can be attributed to the unreacted Ba(NO$_3$)$_2$ or other unknown impurity phases [7]. At higher temperature of 1200°C the impurity level seems to decrease as compared to lower temperatures. The crystal size was calculated using the Debye-Scherer's equation.

The average crystal size calculated from $BaAl_2O_4:Eu^{2+};Nd^{3+};Gd^{3+}$ phosphor sample prepared at 1200^oC was found to be 63 nm. The data used for the calculation is shown in table 4.1.

Table 4.1: Calculated average crystal size for from $BaAl_2O_4:Eu^{2+};Nd^{3+};Gd^{3+}$ phosphor sample prepared at 1200^oC.

peak	2θ	FWHM (β)	D (nm)
[202]	28.418	0.136	60
[220]	34.437	0.127	65
[222]	40.259	0.135	63

Average crystal size (D) = 63 nm
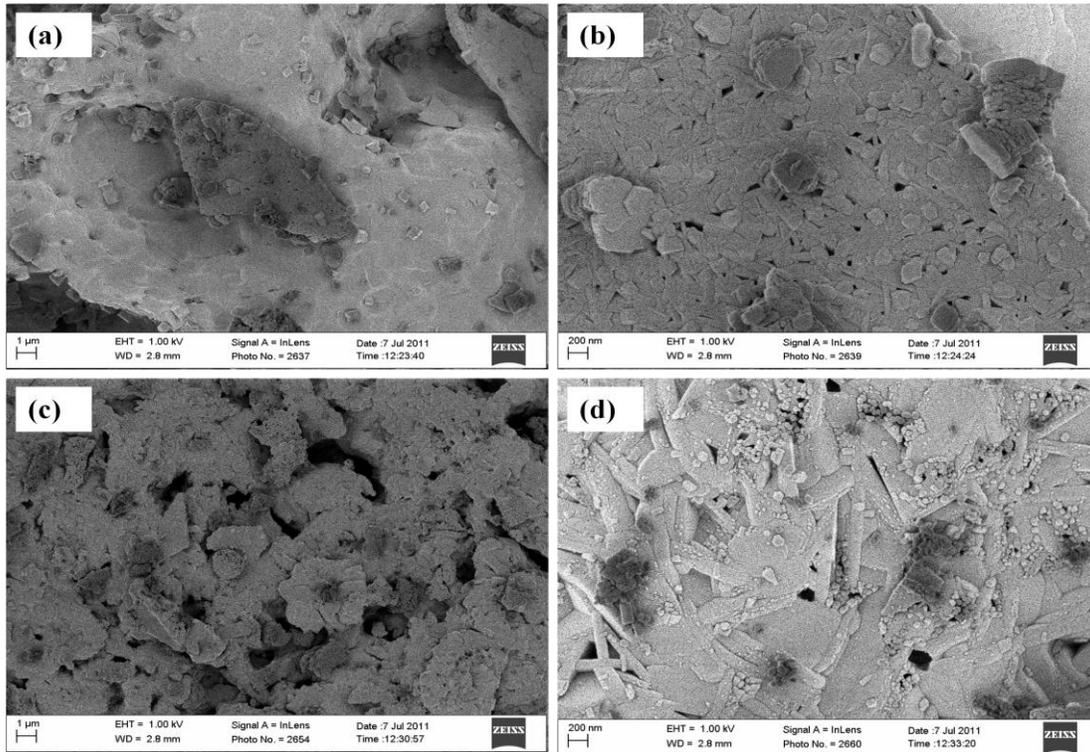
Figure 4.3: SEM images of $BaAl_2O_4:Eu^{2+};Nd^{3+};Gd^{3+}$ prepared at different initiating temperature of (a)-(b) 500^oC and (c)-(d) 1100^oC

The SEM morphologies of $BaAl_2O_4:Eu^{2+};Nd^{3+};Gd^{3+}$ phosphor powders at an initiating temperatures of $500^{\circ}C$ and $1100^{\circ}C$ are shown in figure 4.3. Figure 4.3 (a)-(b) shows the morphology of samples prepared at $500^{\circ}C$ taken at low and high magnification. The surface of the phosphor powder shows some voids and pores and some nano particles on top. Figure 4.3 (c)-(d) also shows the particle morphology of samples prepared at $1100^{\circ}C$ taken at low and high magnification. The surface of the phosphor powder still shows some pores. Figure 4.3.c shows the agglomerated like particles while figure 4.3.d shows the intertwined nano-rod like particles with nano-incrustrations. The voids and pores shown in the surface of the phosphor powders are formed by the escaping of gases during the combustion process and it is said to be an inherent feature of this process [8].
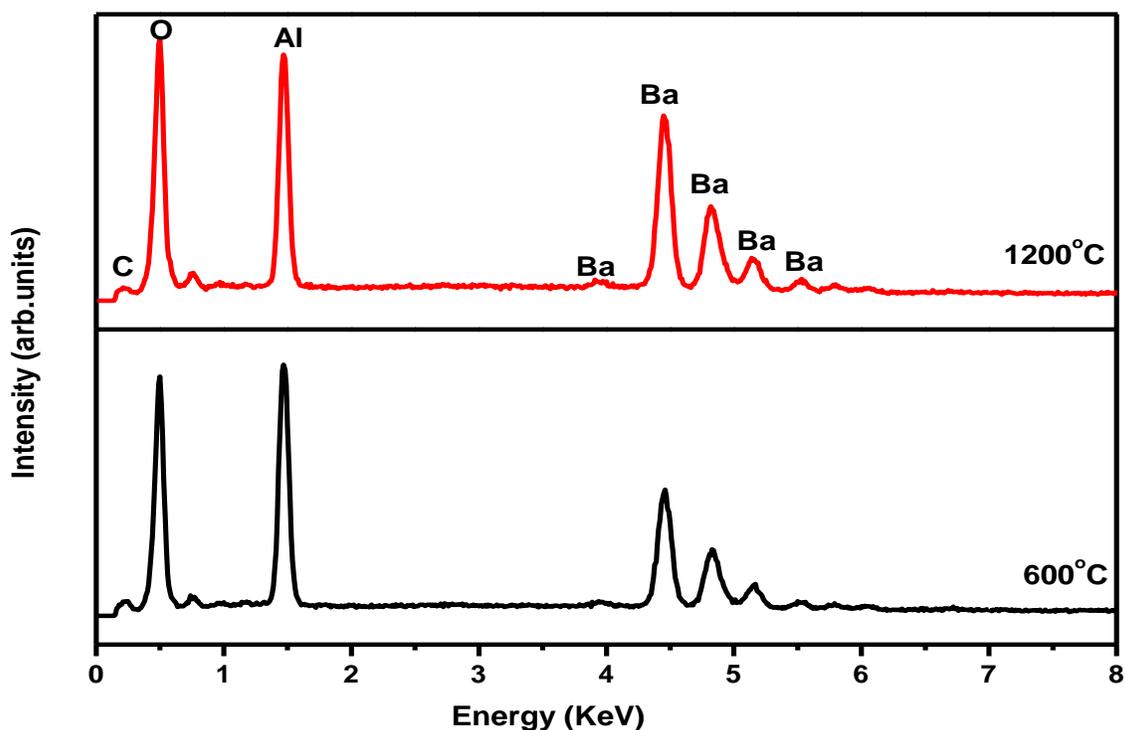
Figure 4.4: EDS spectra of $BaAl_2O_4:Eu^{2+};Nd^{3+};Gd^{3+}$ prepared at an initiating temperature of $600^{\circ}C$ and $1200^{\circ}C$.

Figure 4.4 shows the EDS spectra of $BaAl_2O_4:Eu^{2+};Nd^{3+};Gd^{3+}$ phosphor samples prepared at an initiating temperature of $600^{\circ}C$ and $1200^{\circ}C$, respectively. Most of the elements incorporated in

the phosphor powders are present as shown in the figure 4.4. Eu^{2+}, Nd^{3+} and Gd^{3+} were not detected by EDS since their concentrations were too low.
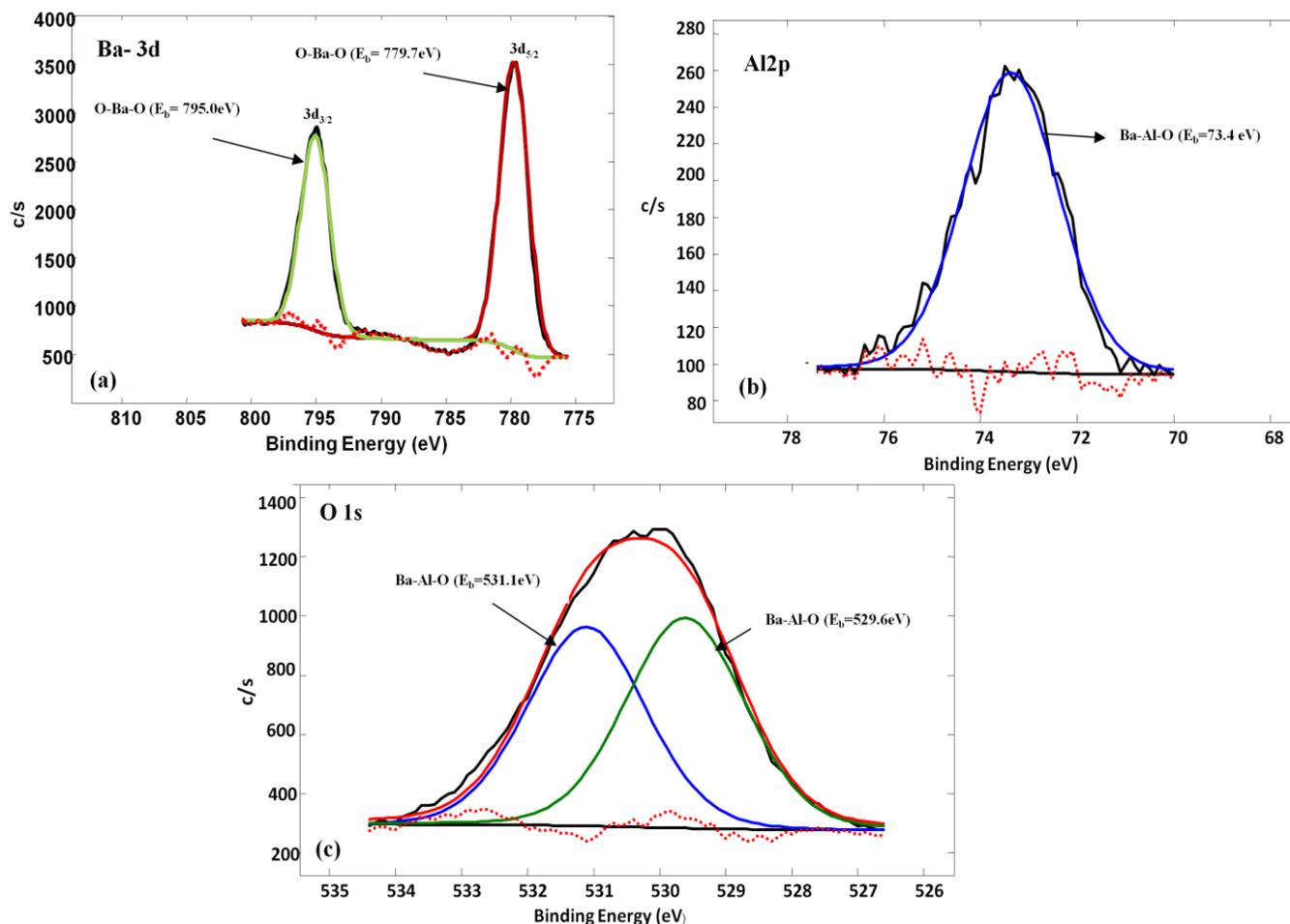
Figure 4.5: Fitted XPS spectra of $BaAl_2O_4:Eu^{2+};Nd^{3+};Gd^{3+}$ prepared at an initiating temperature of 600^oC

Figure 4.5 (a) to (c) shows the X-ray photoelectron spectroscopy (XPS) spectra of $BaAl_2O_4:Eu^{2+};Nd^{3+};Gd^{3+}$ phosphor powder prepared at 600^oC. The XPS 3d spectrum for Ba is shown in figure 4.5 (a) and has two peaks of O-Ba-O bonds for $3d_{3/2}$ and $3d_{5/2}$ existing within the $BaAl_2O_4:Eu^{2+};Nd^{3+};Gd^{3+}$ phosphor powder. The $3d_{3/2}$ and $3d_{5/2}$ peaks were observed at 795 eV and 779 eV, respectively. These two fitted peaks might be from the two Ba^{2+} sites found in $BaAl_2O_4$. Figure 4.5 (b) shows the 2p spectrum for Al. Only one peak was observed and has the

Ba-Al-O bond at 73.4 eV. This could be characteristic of all species in AlO_4 tetrahedra [9]. Li et al, [10], reported the Al2p peak centered at 74.2 eV, indicating the existence of aluminium carboxyl in $TiO_2/BaAl_2O_4:Eu^{2+};Dy^{3+}$ phosphor. Figure 4.5 (c) shows the 1s spectrum for O. The two peaks were observed after fitting the spectrum. These two peaks are from the Ba-Al-O bonds in $BaAl_2O_4$ host at 531.1 eV and 529.6 eV. Zhang et al. [9] reported the binding energy of O1s in $BaAl_2O_4$ to be at 531.3 eV and 529.6 eV. The binding energy at 531.3 eV could be ascribed to the characteristics of Oxygen (O) species in the surface hydroxyl (OH) groups from H_2O molecules absorbed on $BaAl_2O_4$.

4.3.2: Luminescent and decay studies
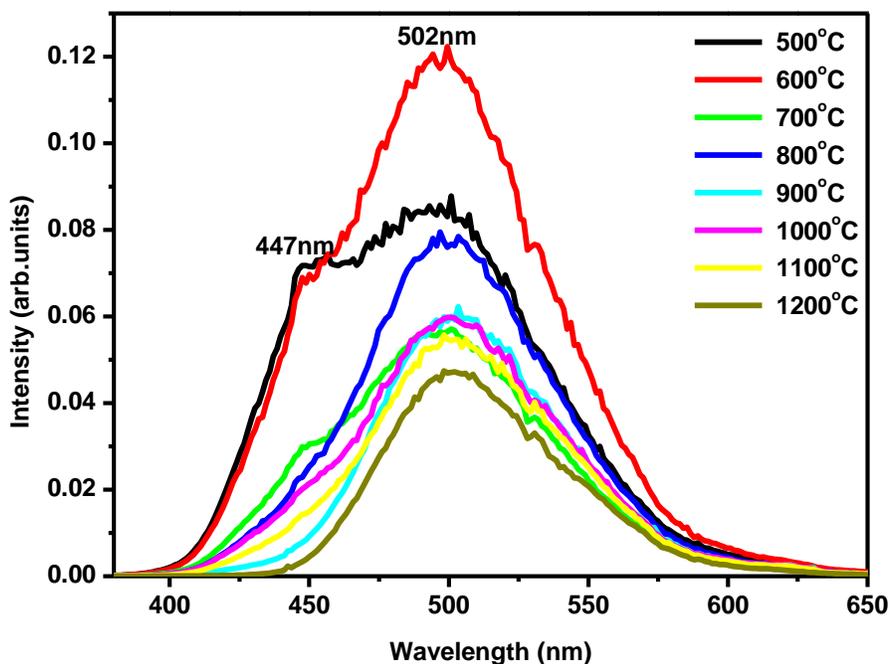
Figure 4.6: PL emission spectra of $BaAl_2O_4:Eu^{2+};Nd^{3+};Gd^{3+}$ prepared at different initiating temperatures

The PL emission spectra of $BaAl_2O_4:Eu^{2+};Nd^{3+};Gd^{3+}$ prepared at different initiating temperatures ranging from 500^oC-1200^oC are shown in figure 4.6. In the case of the phosphor powders prepared at 500^oC-700^oC, two peaks were observed while those prepared at 800^oC-1200^oC only one peak was observed. The main broad emission band was observed at 502 nm and the shoulder at 447 nm. The two maxima peaks observed were due to the transitions from the lowest ^2D of the excited state to the excited state $4f^65d^1$ configuration to the ground $^8S_{7/2}$ level in the $4f^7$ configuration of the Eu^{2+} [11]. Since $BaAl_2O_4$ structure has two Ba^{2+} sites, thus the two emissions observed in the phosphor powders prepared at 500^oC-700^oC correspond to the emission from the two sites. The highest PL emission intensity was observed from the phosphor powder prepared at 600^oC. Figure 4.7 shows the maximum PL intensity versus the initiating temperature for $BaAl_2O_4:Eu^{2+};Nd^{3+};Gd^{3+}$ phosphor powders. These plot shows that the maximum PL intensity was observed for the phosphor powder prepared at 600^oC.
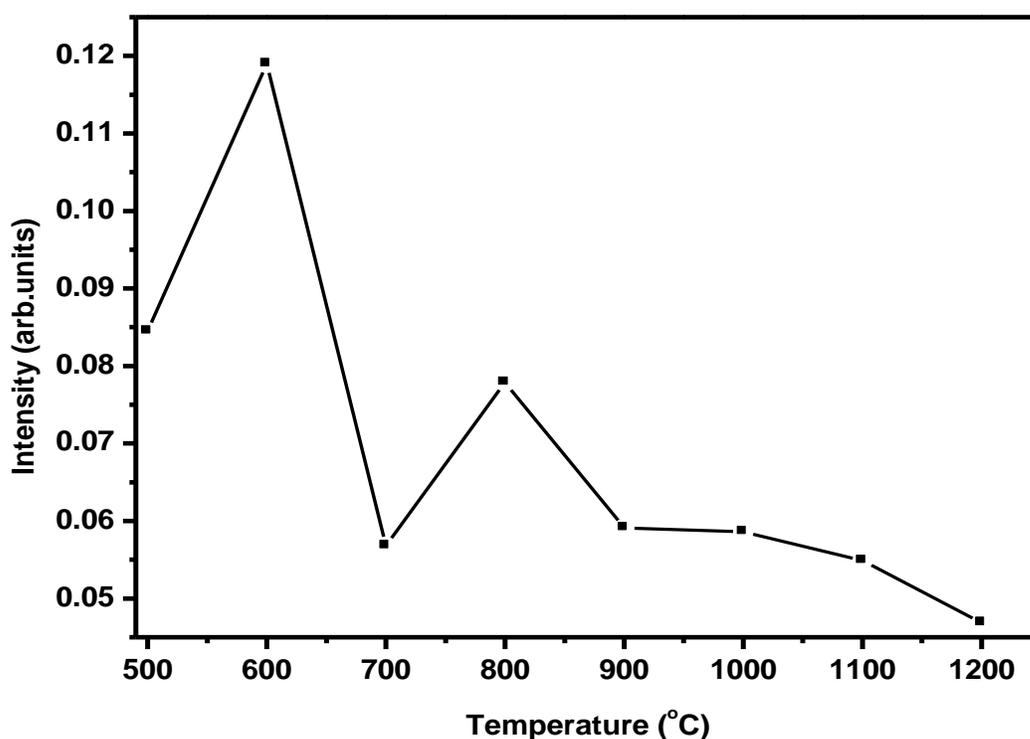
Figure 4.7: Maximum PL intensity versus the initiating temperature for $BaAl_2O_4:Eu^{2+},Nd^{3+},Gd^{3+}$ phosphor powders.
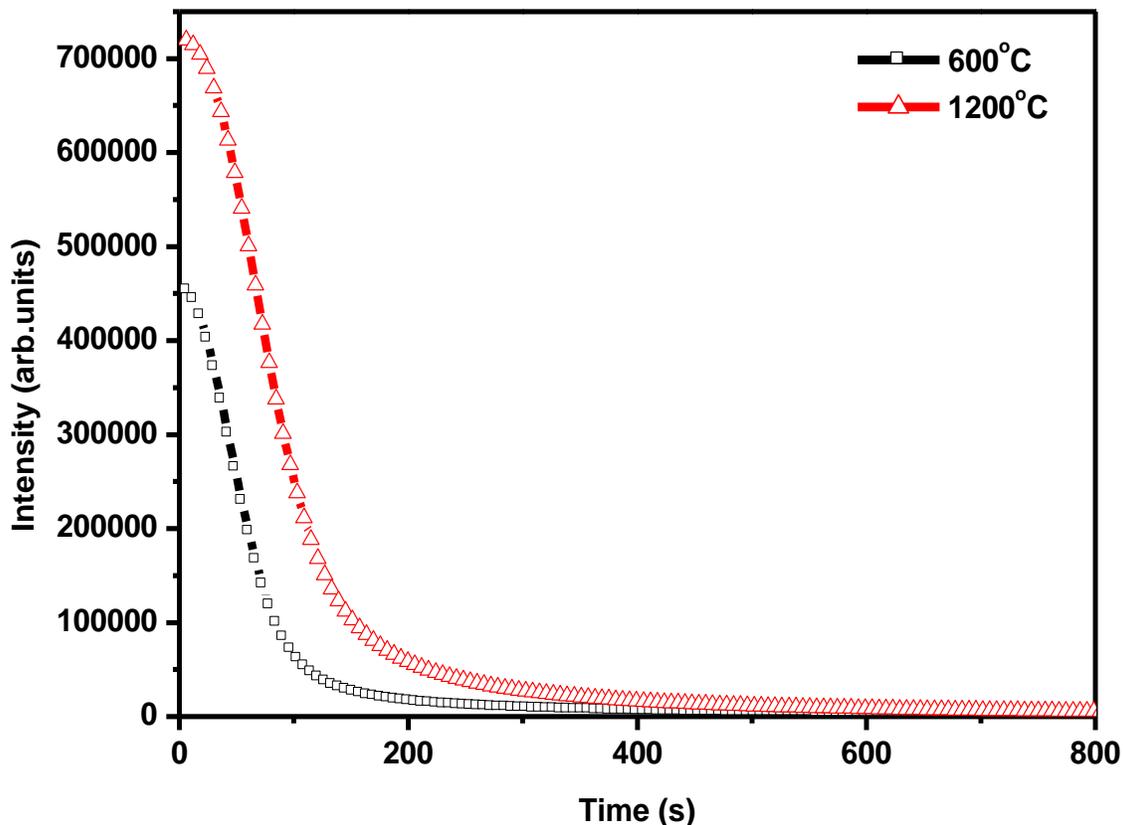
Figure 4.8: Decay curves for BaAl$_2$O$_4$:Eu^{2+};Nd^{3+};Gd^{3+} prepared at an initiating temperature of 600°C and 1200°C.

Figure 4.8 compares the decay characteristics of phosphors prepared at the initiating temperatures of 600°C and 1200°C. The samples were excited for 2 minutes in the darkroom with a 365 nm UV light. After the irradiation source was switched off, both samples first showed rapid decay followed by the long lasting phosphorescence. It is clear from the curves that the rate of decay is comparatively faster in the case of the sample prepared at 600°C compared to that prepared at 1200°C. It is said that the mechanism for the long persistence is due to the trapped-transported-detrapped process [12]. Song et al. [13], prepared SrAl$_2$O$_4$:Eu^{2+};Dy^{3+};Gd^{3+} phosphors by combustion method and reported that Eu^{2+} ions are the luminescent centers and Dy^{3+} and Gd^{3+} work as hole traps. It is therefore most likely that Nd^{3+} and Gd^{3+} are the hole traps and were involved in the trapping-de-trapping of charge carriers which resulted in the long

afterglow of the phosphors investigated in this study. The curves in figure 4.8 were fitted using the third order exponential decay equation:

$$I = A_1 \exp(- t/\tau_1) + A_2 \exp(- t/\tau_2) + A_3 \exp(- t/\tau_3) \tag{1}$$

Where I is the phosphorescence intensity at any time t after switching off the excitation source, A_1, A_2 and A_3 are constants and τ_1, τ_2 and τ_3 are decay times for the exponential components respectively. The decay parameters are listed in table 4.2.

Table 4.2: Decay constants for $BaAl_2O_4:Eu^{2+};Nd^{3+};Gd^{3+}$ phosphors prepared at an initiating temperature of 600^oC and 1200^oC.

Temperature (^oC)	Decay Constants		
	τ_1 (sec)	τ_2 (sec)	τ_3 (sec)
600^oC	21 ± 2	29 ± 2	382 ± 34
1200^oC	30 ± 4	42 ± 4	397 ± 27

4.3.3: Thermoluminescence Studies

Figure 4.9 shows the TL glow curves of $BaAl_2O_4:Eu^{2+}$, Nd^{3+},Gd^{3+} phosphors powders prepared at different temperatures of 600^oC and 1200^oC. The phosphor powders show the main TL glow peaks at $\sim72^oC$ and the less intense TL bands were observed at $\sim170^oC$. These peaks correspond to the deep and shallow traps, respectively [14]. These bands are at a similar position which suggests that the traps responsible for these bands are similar. Katsumata et al. [15] reported that the trapped carries are responsible for the various decay components with different decay times because the recombination between the excited electrons and the trapped holes are greatly influenced by the trap depth. The phosphor powder prepared at 1200^oC shows the optimum TL intensity compared to the one prepared at 600^oC. The glow curve obtained for $BaAl_2O_4:Eu^{2+};Nd^{3+};Gd^{3+}$ phosphors prepared at an initiating temperature of 1200^oC was
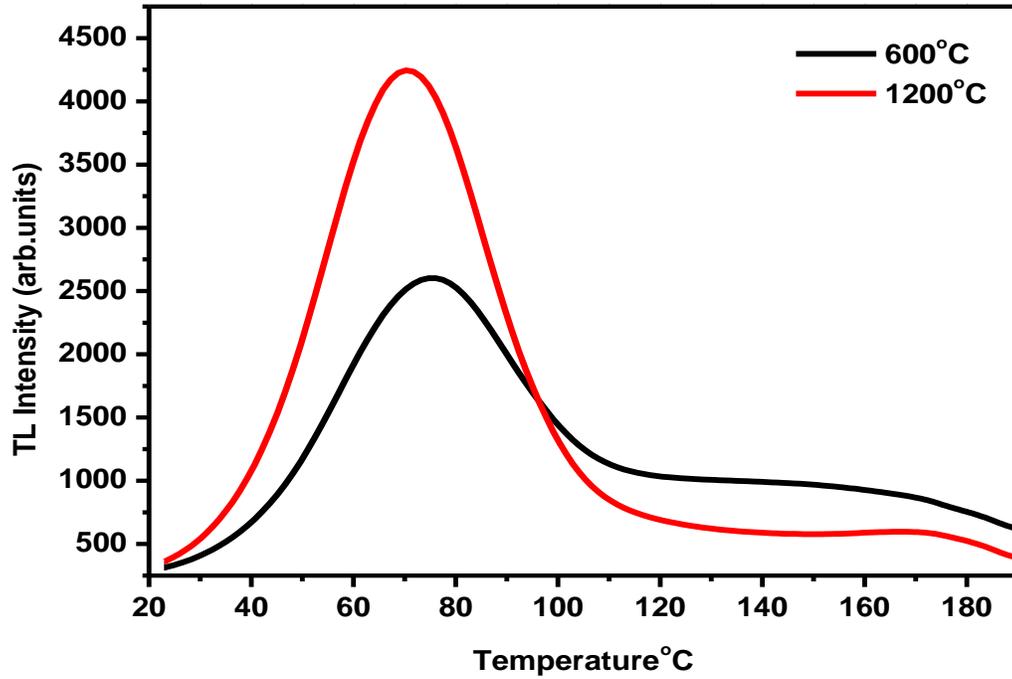
Figure 4.9: TL glow curves for BaAl$_2$O$_4$:Eu^{2+};Nd^{3+};Gd^{3+} prepared at an initiating temperature of 600°C and 1200°C.

deconvoluted into thermal peaks by Gaussian fitting (figure 4.10). The thermal peaks represent the discrete trap levels. Their depth was approximated using the second order kinetic model equation [16]:

$$E = 3.54 \left(\frac{kT_m^2}{\omega} \right) - 2kT_m \qquad (2)$$

Where E is the trap depth of the measured in eV, $k = 1.38 \times 10^{-23}$ m^2 kg s^{-2} K^{-1} is Boltzmann's constant, T_m is the temperature corresponding to the maxima of a thermal peak, and ω is the FWHM (full width at half maximum) of a thermal peak. The approximated depths are listed in table 4.3.
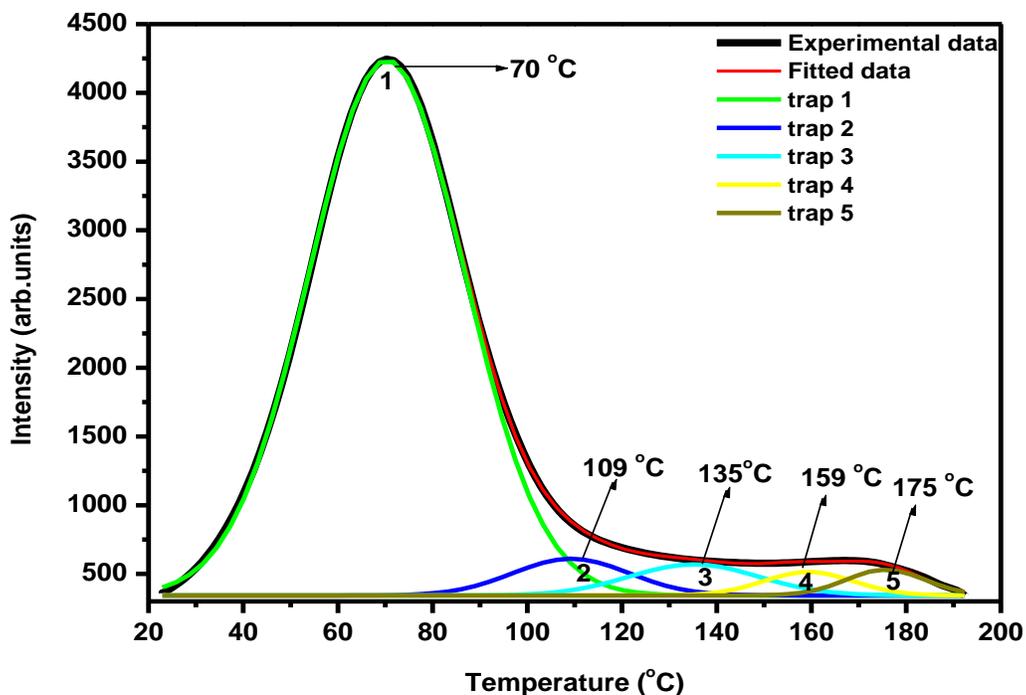
Figure 4.10: Fitted TL glow curve of BaAl$_2$O$_4$:Eu^{2+};Nd^{3+};Gd^{3+} prepared at an initiating temperature 1200°C.

Table 4.3: TL parameters of BaAl$_2$O$_4$:Eu^{2+};Nd^{3+};Gd^{3+} prepared at an initiating temperature 1200°C.

Trap	Tm (^{o}C)	FWHM (^{o}C)	E (eV)
1	70	32	0.05
2	109	25	0.08
3	135	27	0.09
4	159	19	0.11
5	175	17	0.20

4.4: Conclusion

The phosphor powders $BaAl_2O_4:Eu^{2+};Nd^{3+};Gd^{3+}$ were successfully prepared at different initiating temperatures of 400^oC-1200^oC using combustion method. The X-ray diffraction spectra show the hexagonal structure of $BaAl_2O_4$ at temperature range of 500^oC -1200^oC. SEM studies show the different particle morphologies of phosphor powders with the increase in temperature. The broad blue-green emission was observed at 502 nm. This emission can be attributed to the $4f^65d^1$-$4f^7$ transitions of the Eu^{2+} ions. The phosphorescence decay curves were obtained by irradiating the samples with a 365 UV light. The samples prepared at 600^oC and 1200^oC show the main TL glow peaks at around 72^oC. These bands are at a similar position which suggests that the traps responsible for these bands are similar. The rate of decay seems to be faster in phosphor sample prepared at 600^oC than the one prepared at 1200^oC. The hole trapped-transported-detrapped process will lead to the long afterglow properties of the phosphors. The long afterglow observed in this study can be attributed to the traps created by Nd^{3+} and Gd^{3+} ions.

References

[1] H. Ryu and K.S. Bartwals, Journal of Physic D: Applied Physics. **41** 235404-235407 (2008)

[2] X. Yu, C. Zhou, X. He, Z. Peng and S. Yang, Materials Letters **58** 1084-1091 (2004)

[3] T. Peng, L. Huajun, H. Yang and C. Yan, Materials Chemistry and Physics **85** 68-72 (2004)

[4] Y. L. Lui, X. M. Tang, X. D. Chen, B. F. Lei and D. X. Feng, Chinese Chemical Letters **10** 709-712 (1999)

[5] H. Ryu, B.K. Singh and K.S. Bartwals, Physica B **403** 126-130 (2008)

[6] R.Sakai, T. Katsumata, S. Komuro and T. Morikawa, Journal of Luminescence **85** 149-154 (1999)

[7] S. Feilong and Z. Junwu, Journal of rare earth, **29** 326-329 (2011)

[8] V. Singh, R.P.S. Chakradhar, J.L. Rao and D. Kim, Journal of Luminescence **128** 394-402 (2008)

[9] L. Zhang, L. Wang and Y. Zhu, Advanced Functional Material **17** 3781-3790 (2007)

[10] S. Li, W. Wang, Y. Chen, L. Zhang, J. Guo and M. Gong, Catalysis Communications **10** 1048-1051 (2009)

[11] R. Sefani, L.V.C Rodrigues, C.A.A Carvalho, M.C.F.C Felinto, H.F Brito, M. Lastusaari and J. Holsa, Optical Materials **31** 1815-1818 (2009)

[12] H. Ryu and K.S. Bartwal, Reasearch Letters in Materials Science, **2007** 23643- 23647 (2007)

[13] H. Song, D. Chen, W. Tang and Y. Peng, Displays **20** 41-44 (2008)

[14] T. Aitasalo, J. Holsa, H. Jungner, J. Krupa, M. Lastusaari, J. Legendziewics and J. Niittykoski, Radiation Measurements **38** 727-730 (2004)

[15] T. Katsumata, S. Toyomane, R. Sakai, S. Komuro and T. Morikawa, Journal of the American Ceramic Society **89** 932-936 (2006)

[16] R. Chen, Journal of Applied Physics **40** 570-585 (1969)

CHAPTER 5

SYNTHESIS AND PHOTOLUMINESCENCE STUDIES OF $(Ba_{1-x}Sr_x)Al_2O_4:Eu^{2+};Nd^{3+}$ PREPARED BY COMBUSTION METHOD

5.1: Introduction

Long afterglow phosphor is a special type of luminescent materials that store energy under proper excitation and after the excitation source is switched off, releases the conserved energy by means of visible light, observable in darken surroundings for several hours [1]. The demand for developing efficient luminescent materials such as rare-earth doped aluminate powders has attracted more attention for possible photonic applications [2].The phosphorescence properties of alkaline earth aluminate can be attributed to the presence of rare earth ions in its crystal structure.

The $SrAl_2O_4:Eu^{2+};Dy^{3+}$ crystal and $BaAl_2O_4:Eu^{2+};Dy^{3+}$ crystal have been considered as useful blue and green phosphors respectively owing to their long-duration phosphorescence characteristics. A mechanism for long-duration phosphorescence from Eu^{2+} ions in these aluminates has been proposed based on the hole trapping because of the Dy^{3+} and/or Nd^{3+} ions doped as auxillary activators. In the long–duration phosphors, energy levels of traps generated by auxillary activators, Nd or Dy, have suitable depth of release trapped holes thermally [3]. To enhance the long afterglow of $BaAl_2O_4$, an attempt has been made in this study. Ba was substituted by Sr to form $(BaSr)Al_2O_4$ host. The effects of Ba and Sr concentrations on the long afterglow properties were investigated.

5.2: Experimental Procedure

The powder phosphors of $(Ba_{1-x}Sr_x)Al_2O_4;Eu^{2+};Nd^{3+}$ (x = 0, 0.4, 0.5, 0.6 and 1) were prepared by combustion method at an initiating combustion temperature of 500^oC. The following precursors: Barium nitrate $(Ba(NO_3)_3.4H_2O)$, Strontium nitrate $[Sr(NO_3)_3.4H_2O]$, Aluminate nitrate $[Al(NO_3).9H_2O]$, Neodymium nitrate $[Nd(NO_3)_3.5H_2O]$, Europium nitrate $[Eu(NO_3)_3.6H_2O]$ and urea $[CO(NH_2)_2]$ all in purity were weighed according to their stoichiometry. The phosphor preparations are shown as illustrated by the flow chart in figure 5.1.
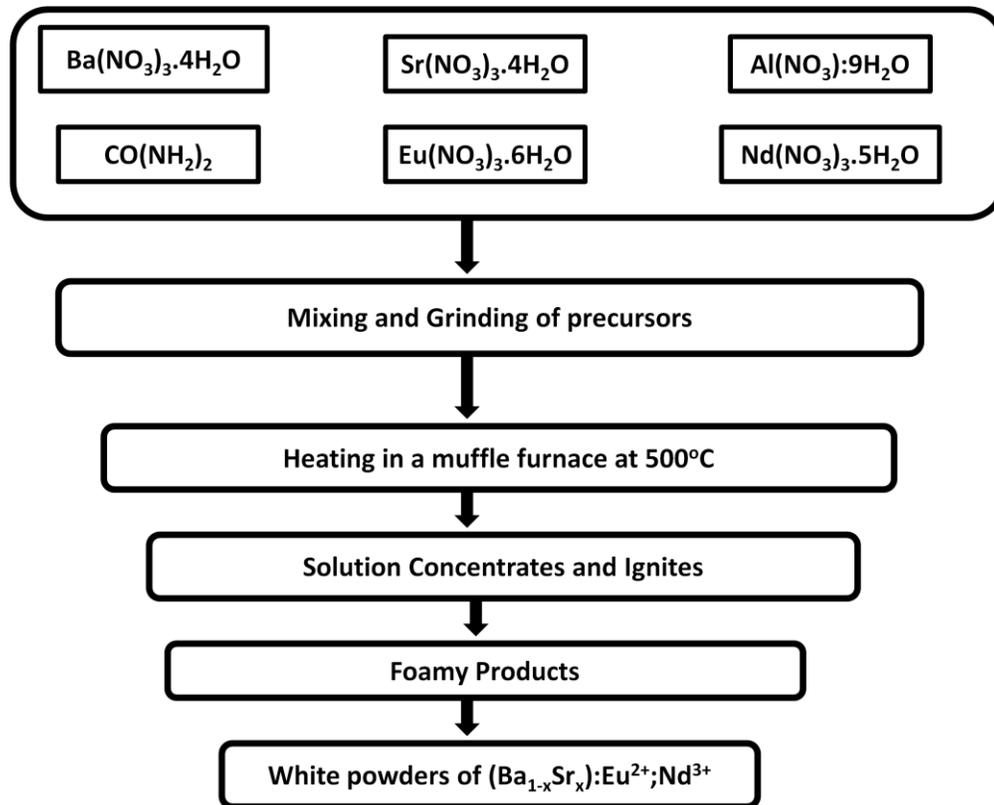
Figure 5.1: Flow chart for the preparation of $(Ba_{1-x}Sr_x)Al_2O_4:Eu^{2+};Nd^{3+}$ (x = 0, 0.4, 0.5, 0.6 and 1.0) phosphor powders using combustion method.

5.3: Results and discussion

5.3.1: Structural properties

Figure 5.2 shows the XRD patterns for a series of $BaAl_2O_4$:Eu^{2+};Nd^{3+} with (x = 0, 0.4, 0.5, 0.6 and 1.0) prepared at an initiating temperature of 500^oC. The X-ray diffraction patterns for x = 0 shows the hexagonal phase for $BaAl_2O_4$ according to the card file (JCPDS: 17-0703) and the one for x = 1 shows the monoclinic phase for $SrAl_2O_4$ according to the card file (JCPDS: 74-0794). Even though the main peaks of $BaAl_2O_4$ and $SrAl_2O_4$ are shown, there are other diffraction peaks present that may be attributed to other impurities or unreacted $Ba(NO_3)_2$ and $Sr(NO_3)_2$ precursors [4]. The presence of other phases or some of the precursors can be attributed to the fact that the combustion wave is not uniform and a portion of the precursors did not react completely during the combustion process [4]. The X-ray diffraction patterns for the phosphor powders with the compositions of x = 0.4, 0.5 and 0.6 shows the mixed composition of $BaAl_2O_4$ and $SrAl_2O_4$ structures.
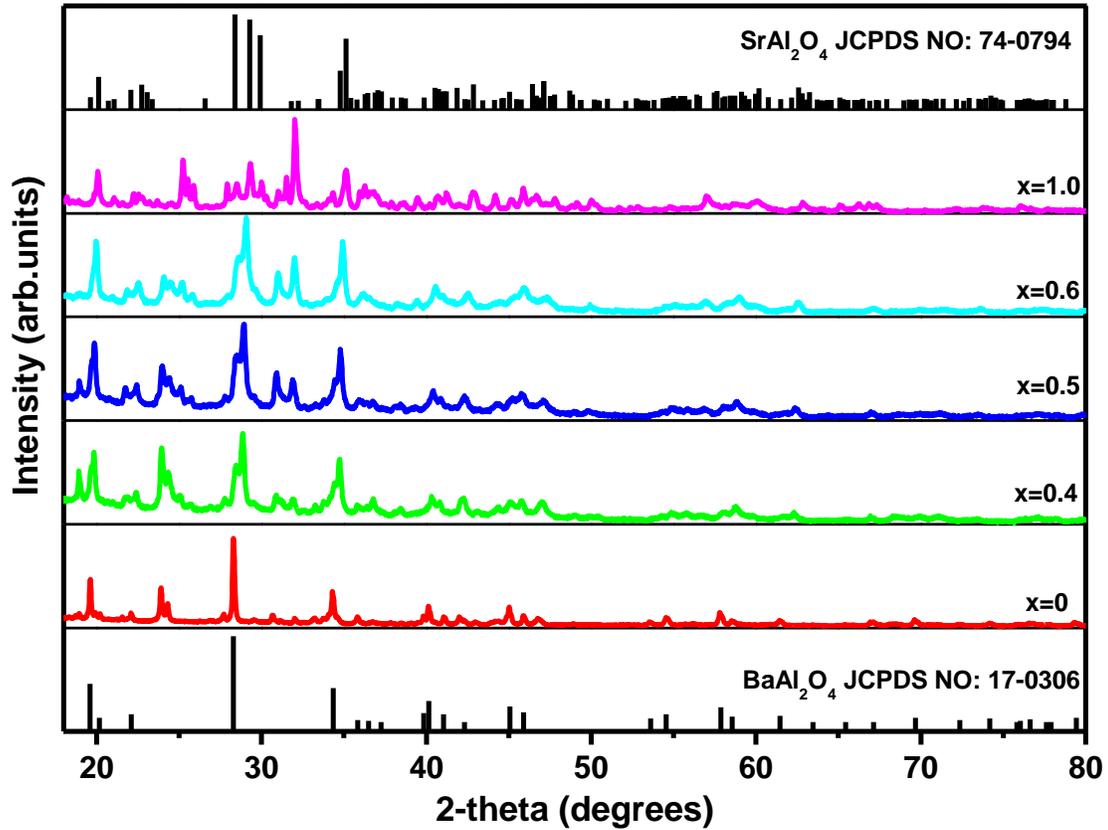
Figure 5.2: XRD patterns of phosphor powders of $(Ba_{1-x}Sr_x)Al_2O_4:Eu^{2+};Nd^{3+}$ as-prepared at initiating temperature of 500^oC.

The FT-IR spectra of the as-prepared $(Ba_{1-x}Sr_x)Al_2O_4:Eu^{2+};Nd^{3+}$ phosphors with composition of $x = 0$, 0.5 and 1 at the initiating temperature of 500^oC are shown in figure 5.3. The NO_3 band observed at 1454 cm^{-1} in all samples can be attributed to the presence of the nitrates. This NO_3 band observed in the FT-IR sprectra agree with the X-ray diffraction spectra that there are unreacted $Ba(NO_3)_2$ and $Sr(NO_3)_2$ precursors. The bands between 1000-500 cm^{-1} correspond to Al-O bonds in aluminates oxides [5]. The sample with composition $x = 0$ shows more intense peaks compared to those with composition of $x = 0.5$ and $x = 1$.
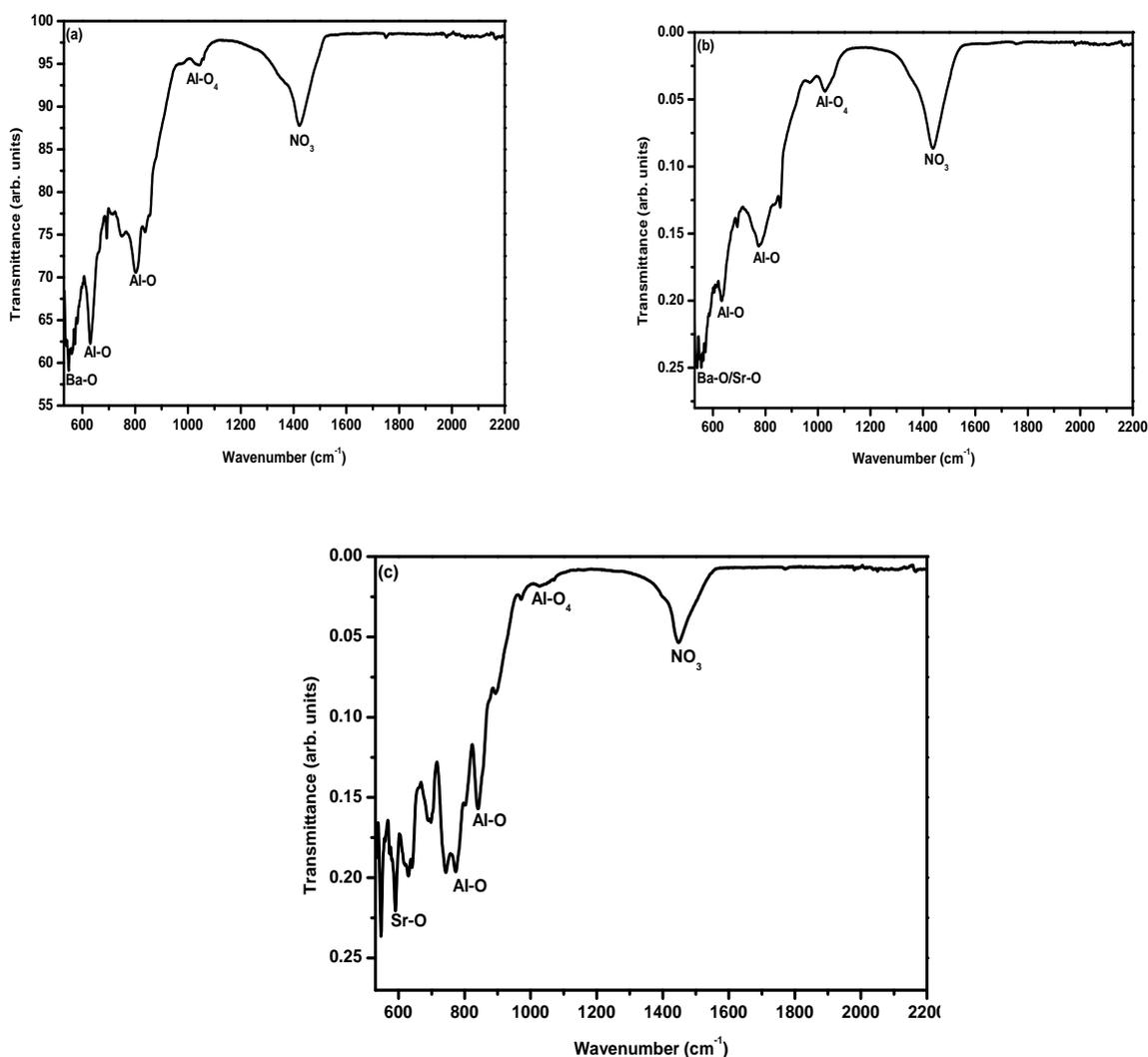
Figure 5.3: FTIR spectra of $(Ba_{1-x}Sr_x)Al_2O_4:Eu^{2+};Nd^{3+}$ phosphor samples for (a) x = 0, (b) x = 0.5 and (c) x = 1 prepared at an initiating temperature of 500°C.

SEM study was carried out to investigate the surface morphogy of the synthesized phosphor samples of $(Ba_{1-x}Sr_x)Al_2O_4:Eu^{2+};Nd^{3+}$. Figure 5.4 (a)-(c) shows the SEM morphologies of the as-prepared $(Ba_{1-x}Sr_x)Al_2O_4:Eu^{2+};Nd^{3+}$ phosphors with composition x = 1, x = 0.5 and x = 0 at an initiating temperature of 500°C. Figure 5.4 (a) shows the spherical particles of $SrAl_2O_4:Eu^{2+};Nd^{3+}$ (x = 1). Figure 5.4 (b) clearly shows the mixture of nano-rods and spherical

particles for the compostion x = 0.5. The morphology of the compostion x = 0, shown in figure 5.4 (c), shows nano-rod like particles of pure $BaAl_2O_4$:Eu^{2+};Nd^{3+}.
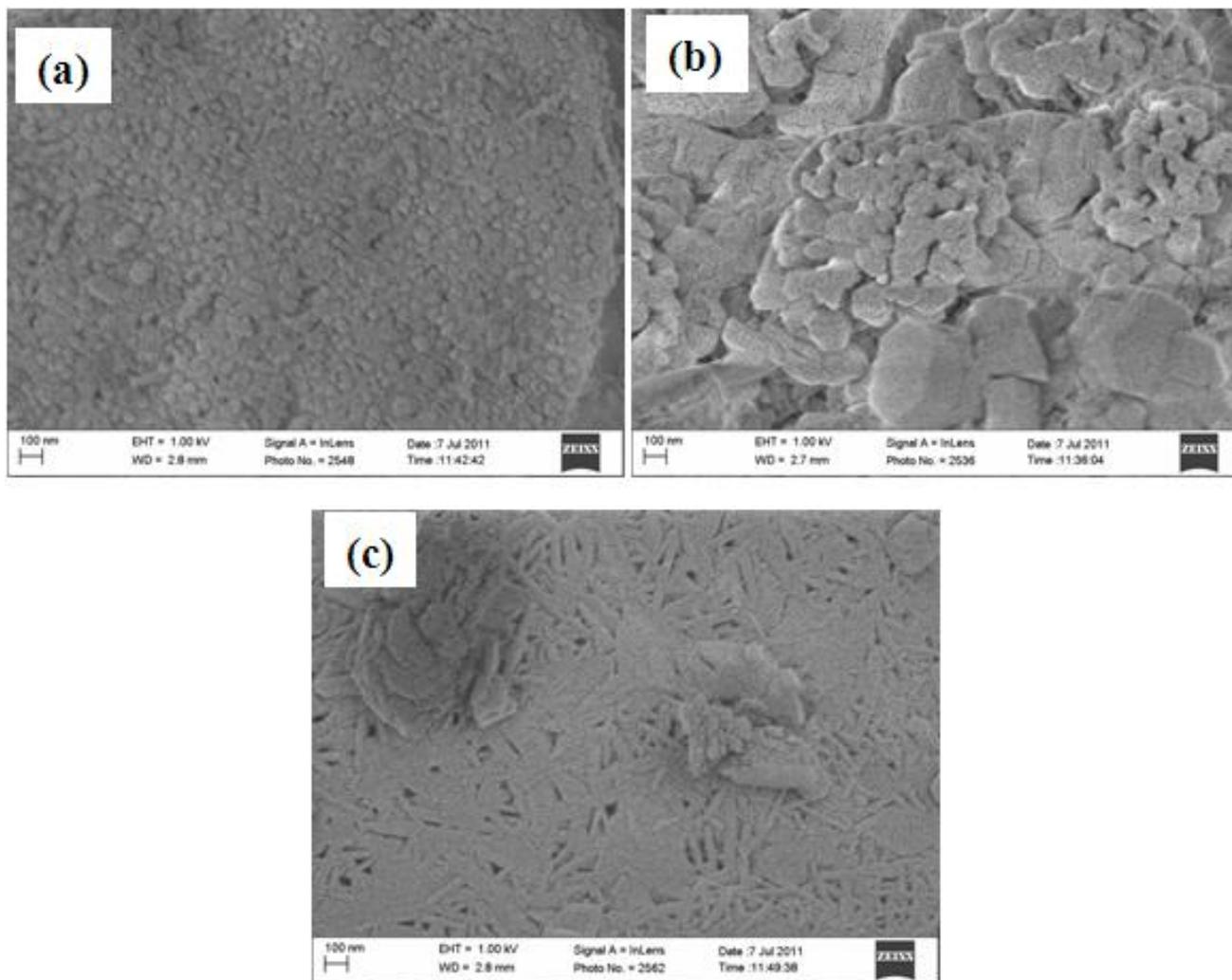
Figure 5.4: SEM images of $(Ba_{1-x}Sr_x)Al_2O_4$:Eu^{2+};Nd^{3+} phosphor samples for (a) x = 1, (b) x = 0.5 and (c) x = 0 prepared at an initiating temperature of 500°C.

5.3.2: Luminescence and decay studies

Figure 5.5 shows the PL emission spectra of $(Ba_{1-x}Sr_x)Al_2O_4$:Eu^{2+};Nd^{3+}phosphors powder with the composition of x = 0, 0.4, 0.5, 0.6 and 1. All the samples were excited using a 325 nm He-

Cd laser. The broad emission spectra observed in all the samples can be attributed to the transition between the ground ($^8S_{7/2}(4f^7)$) and the excited ($4f^65d^1$) energy states of Eu^{2+} ions in the host structure of $(Ba_{1-x}Sr_x)Al_2O_4$. Figure 5.5(a)-(b) show $(Ba_{1-x}Sr_x)Al_2O_4:Eu^{2+};Nd^{3+}$ (x = 0) and $(Ba_{1-x}Sr_x)Al_2O_4:Eu^{2+};Nd^{3+}$ (x = 1) with blue-green to bright green emission with peaks at 505 nm and 520 nm respectively. The gradual replacement of Ba^{2+} by Sr^{2+} (increasing the value of x) shows the green shift in the emissions peaks.
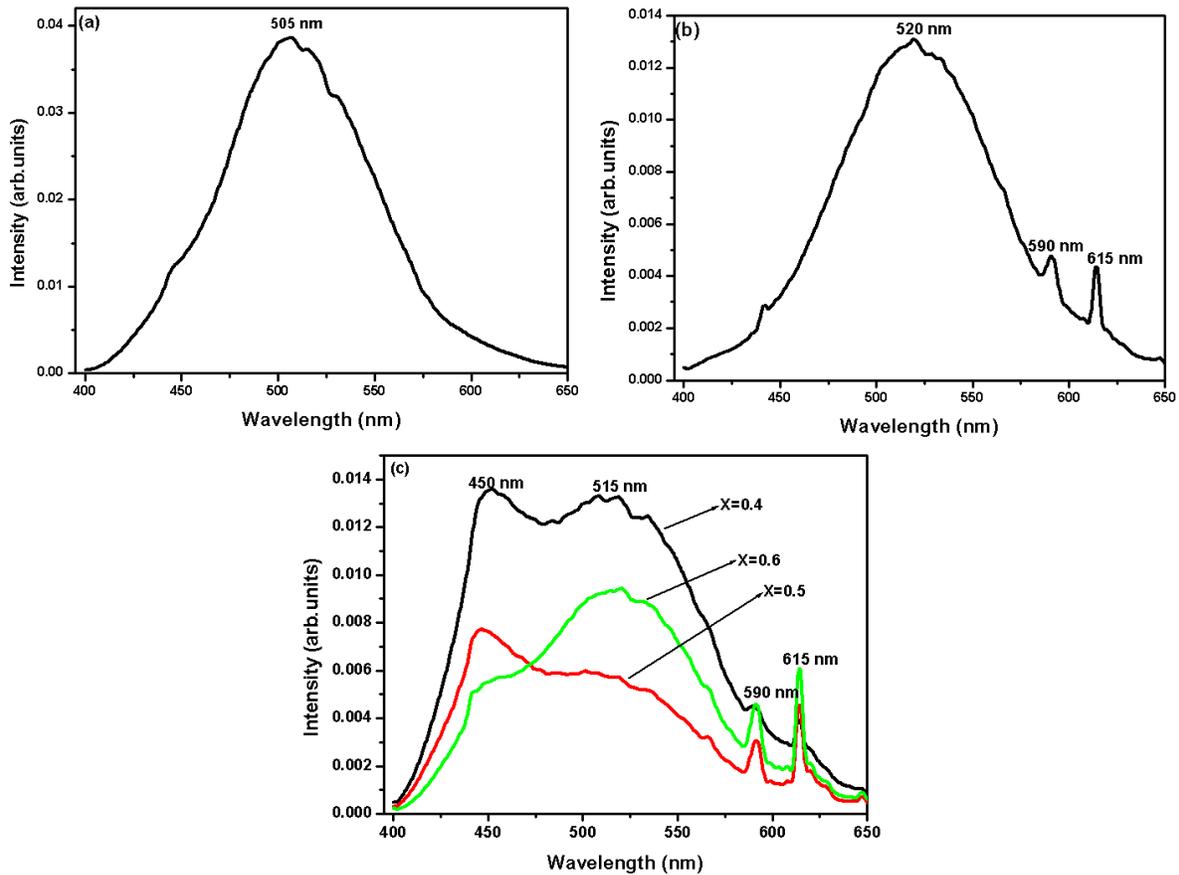
Figure 5.5: Emission spectra of as prepared phosphor samples of $(Ba_{1-x}Sr_x)Al_2O_4:Eu^{2+};Nd^{3+}$ at 500^0C for, (a) x = 0, (b) x = 1 and (c) x = 0.4, x = 0.5 and x = 0.6.

Figure 5.5(c) clearly illustrates the influence of the crystal field strength of the Eu^{2+} ions, which determines the peak positions on the emission spectra. The intensity of crystal field is said to be inversely proportional to the distance from the coordinate groups to the central cation. When the Sr^{2+} is replaced with Ba^{2+} the intensity of crystal field is strengthened because of the smaller

radius of Sr^{2+}, which leads to the shift of the emission band [6]. The observed additional peaks at 590 nm and 615 nm in $(Ba_{1-x}Sr_x)Al_2O_4:Eu^{2+};Nd^{3+}$ with the compositions x = 0.4, 0.5, 0.6 and 1 are attributed to the unreacted Eu^{3+} in the host lattice.
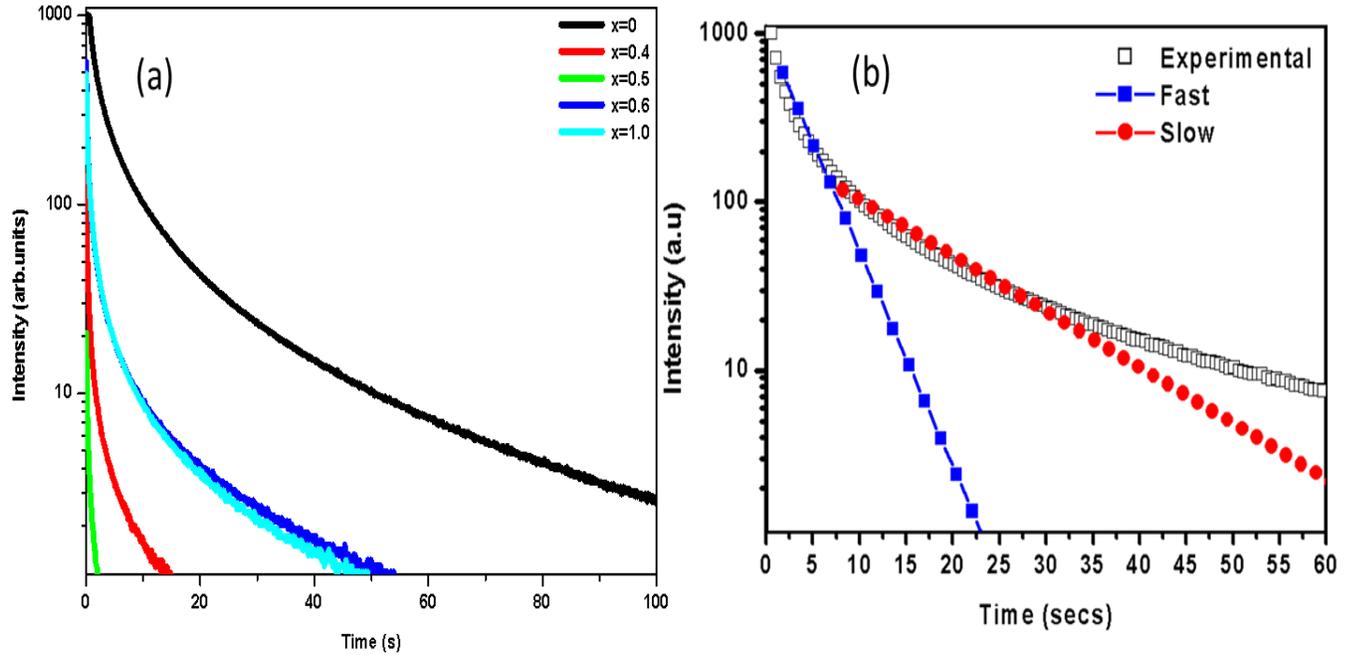
Figure 5.6: (a) Decay curves of $(Ba_{1-x}Sr_x)Al_2O_4:Eu^{2+};Nd^{3+}$ phosphor samples prepared at an initiating temperature of 500°C, (b) Semilogarithmic graph of the as prepared $(Ba_{1-x}Sr_x)Al_2O_2:Eu^{2+};Nd^{3+}$ phosphor powder for x = 0.

Decay curves of $(Ba_{1-x}Sr_x)Al_2O_4:Eu^{2+};Nd^{3+}$ samples is shown in figure 5.6. The phosphor powder with (x = 0) exhibited relatively longer afterglow compared to the phosphor samples of (x = 1) and the mixed compositions (x = 0.5) as shown in figure 5.6 (a). The long afterglow of Nd^{3+} co-doping in $MAl_2O_4:Eu^{2+}$ was also observed by Katsumata et.al [3]. The decay curves were fitted using the second exponential decay equation:

$$I = A_1 exp\left(-\frac{t}{\tau_1}\right) + A_2 exp\left(-\frac{t}{\tau_2}\right) \qquad (1)$$

Where I is the phosphorescence intensity at any time t after switching off the excitation source, A_1 and A_2 are constants and τ_1 and τ_2 are decay times for the exponential components respectively [7]. The decay constants of the fitted curves are listed in table 5.1. The decay data for x = 0 plotted in figure 5.6(b) show that, in agreement with equation (1), the decay is characterized by two components, namely the fast and the slow components for which the decay constants were found to be 3 ± 0.04 and 13 ± 0.10 seconds respectively. Chen et al. [8] reported that the carriers trapped at different trapping level are responsible for the various decay components, because the recombination between the excited electron and trapped hole is influenced greatly by the trap depth.

Table 5.1: Decay constants for $(Ba_{1-x}Sr_x)Al_2O_4{:}Eu^{2+}{;}Nd^{3+}$ phosphor samples with the composition x = 0, 0.4, 0.5, 0.6 and 1.

Compositions	Decay constants	
	τ_1 (sec)	τ_2 (sec)
x = 0	1.82 ± 0.021	14.19 ± 0.260
x = 0.4	0.13 ± 0.002	2.20 ± 0.046
x = 0.5	0.12 ± 0.002	1.72 ± 0.046
x= 0.6	0.17 ± 0.003	2.96 ± 0.034
x= 1.0	0.21 ± 0.003	3.28 ± 0.060

5.4: Conclusion

The phosphor samples of $(Ba_{1-x}Sr_x)Al_2O_4{:}Eu^{2+}{;}Nd^{3+}$ with the composition x = 0, 0.4, 0.5, 0.6 and 1.0 were successfully synthesized by combustion method at an initiating temperature of 500^oC. The X-ray diffraction patterns showed the hexagonal structure of $BaAl_2O_4$ and monoclinic structure of $SrAl_2O_4$ at the compositions x = 0 and x = 1 respectively. The FT-IR

spectra showed that the phosphor sample with the composition x = 0 is more intense compared to the compositions of x = 0.5 and x = 1. SEM investigations indicate the change in surface morphology for different compositions. The blue-green to bright-green emission was observed in the emission spectra when the composition moves from $BaAl_2O_4$ to $SrAl_2O_4$. The emission intensity was high for the composition of x = 0. The long persistence was observed for $(Ba_{1-x}Sr_x)Al_2O_4:Eu^{2+};Nd^{3+}$ with the composition x = 0.

References

[1] C. Fu, Y. Hu, Y. Wang, H. Wu, X. Wang, Journal of Alloys and Compounds, **502** 423–428 (2010)

[2] X.Y. Chen, C. Ma, S. Ping Bao, Solid State Sciences **12** 857–863 (2010)

[3] T. Katsumata, S. Toyomane, R. Saraki, S. Komuro, and T. Morikawa, Journal of the American Ceramic Society **89** 932-936 (2006)

[4] B.M. Mothudi, O.M. Ntwaeaborwa, J.R. Botha, H.C. Swart, Physica B **404** 22 4440-4444 (2009)

[5] A. A. Da Silva, A. de Souza Goncalves, M.R. Davolos, Journal of Sol-Gel Science and Technology **49** 101–105 (2009)

[6] T. Xiaoming, L. Yuanhong, L. Yuzhu, H. Yunsheng, H. Huaqiang, Z. Weidong, Journal of Rare Earths **27** 54-58 (2009)

[7] B. Faridnia, M.M.K. Motlagh and A. Maghsoudipour, Pigment and Resin Technology **36** 216-223 (2007)

[8] R. Chen, Y. Wang, Y. Hu, Z, Hu and C. Liu, Journal of Luminescence **128** 1180-1184 (2008)

CHAPTER 6

Effects of Ba^{2+} and Zn^{2+} concentrations on the structure and luminescent properties of (Ba$_{1-x}$Zn$_x$)Al$_2$O$_4$:Eu^{2+};Nd^{3+}

6.1: Introduction

Many attempts have been made to enhance the luminescence properties of alkaline earth aluminates phosphors. Jung et al. [1] enhanced the emission intensity of SrAl$_2$O$_4$:Eu^{2+};B^{3+} phosphor by substituting the Sr^{2+} with the Zn^{2+} ions. In this chapter, the emission intensity of BaAl$_2$O$_4$:Eu^{2+};Nd^{3+} was enhanced by substituting the Ba with different concentrations of Zn to form (Ba$_{1-x}$Zn$_x$)Al$_2$O$_4$:Eu^{2+};Nd^{3+} phosphor. The phosphor powders were prepared by combustion method at 500°C. The structural properties and luminescence studies of these phosphors were investigated by X-ray Diffraction (XRD), Scanning Electron Microscopy (SEM) and a 325 nm He-Cd laser.

6.2: Experimental Procedure

The following precursors: Barium nitrate [Ba(NO$_3$)$_3$.4H$_2$O] and Aluminium nitrate [Al(NO$_3$)$_2$.9H$_2$O], Europium nitrate [Eu(NO$_3$)$_3$.6H$_2$O], Neodymium nitrate [Nd(NO$_3$)$_3$.5H$_2$O], Zinc nitrate [N$_2$O$_6$Zn.6H$_2$O] and Urea [CO(NH$_2$)$_2$)] were used to prepare the phosphor powders of (Ba$_{1-x}$Zn$_x$)Al$_2$O$_4$:Eu^{2+};Nd^{3+} with the compositions (x = 0, 0.2, 0.4, 0.5, 0.6, 0.8 and 1). The phosphor powders were prepared by a combustion method at an initiating temperature of 500°C as shown by the flow chart in figure 6.1.
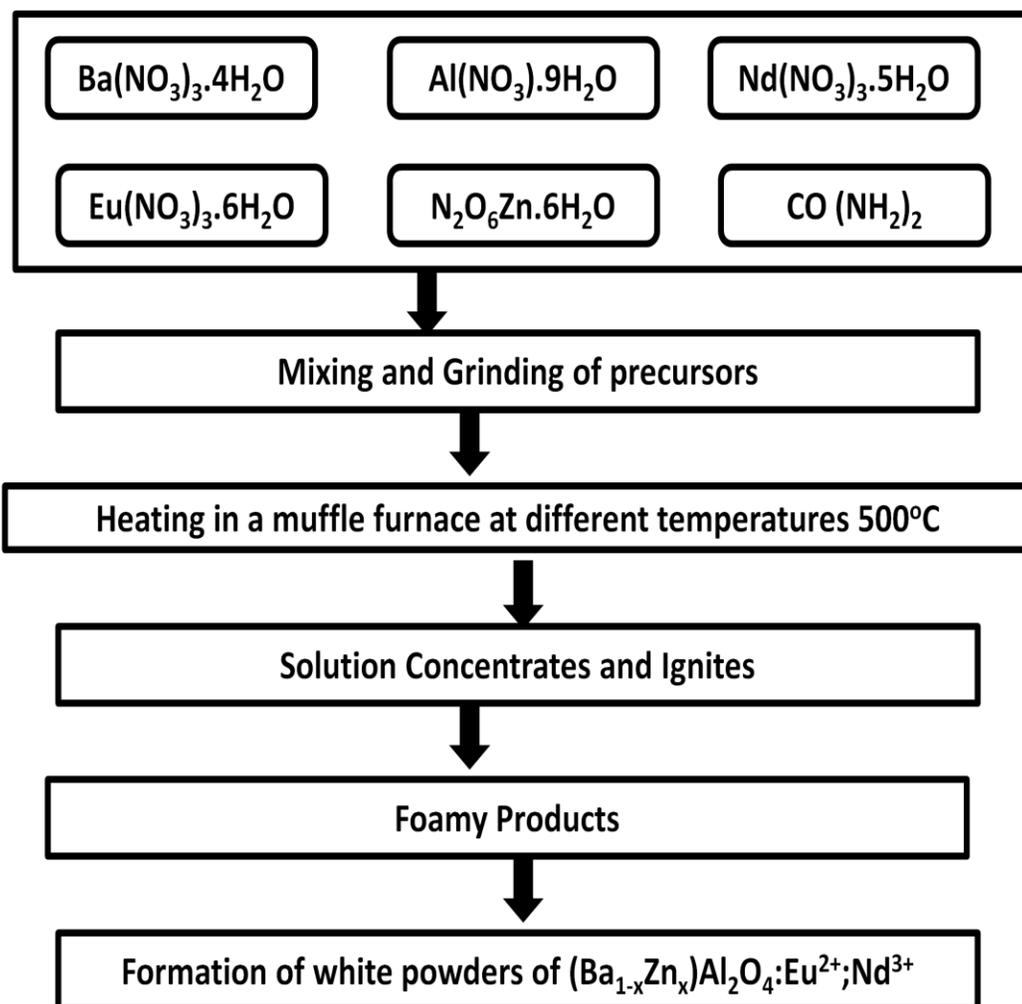
Figure 6.1: Flow chart for the preparation of $(Ba_{1-x}Zn_x)Al_2O_4:Eu^{2+};Nd^{3+}$ (x = 0, 0.2, 0.4, 0.5, 0.6, 0.8 and 1) prepared at an initiating temperature of 500^oC.

6.3: Results and discussion

6.3.1: Structural properties
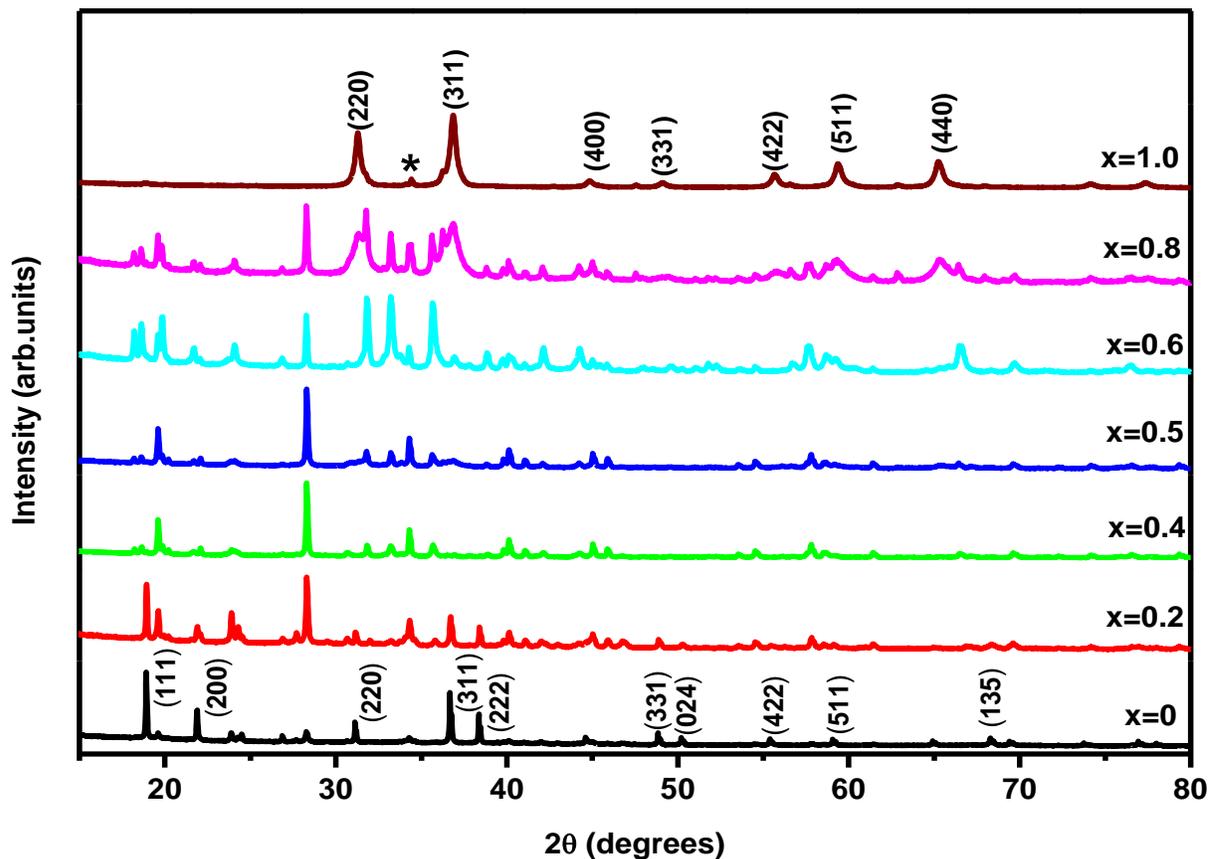
Figure 6.2: XRD patterns of $(Ba_{1-x}Zn_x)Al_2O_4:Eu^{2+};Nd^{3+}$ with the composition of x = 0, 0.2, 0.4, 0.5, 0.6, 0.8 and 1 prepared at an initiating temperature of 500^oC.

The X-ray diffraction patterns of $(Ba_{1-x}Zn_x)Al_2O_4:Eu^{2+};Nd^{3+}$ phosphor powders with the compositions x = 0, 0.2, 0.4, 0.5, 0.6, 0.8 and 1 prepared at an initiating temperature of 500^oC are shown in figure 6.2. The XRD at x = 0 shows that the spectrum correspond to the cubic structure of $Ba(NO_3)_2$ according to the JCPDS card file 76-1376. The $BaAl_2O_4$ parent structure was not formed since 500^oC temperature is too low for the precursors to react completely. The X-ray diffraction pattern at x = 1 clearly correspond to the cubic spinel structure of zinc aluminate

according to the JCPDS card file 05-0669. Even though the major peaks correspond to the $ZnAl_2O_4$ structure, there are some additional peaks marked with an asterisk which might be attributed to the ZnO impurities. These ZnO impurities were also reported by Barros et al [2]. The same results of a cubic structure of $ZnAl_2O_4$ were obtained by Chen et al, after preparing the $ZnAl_2O_4:Eu^{2+}$ using carbon nanospheres as hard templates [3]. In this study, it can be reported that the Nd^{3+} co-doping does not have any effect on the crystallinity of the phosphor powders. The particle sizes for the phosphor samples were calculated using the Debye-Scherer's equation [4]. The results shown in table 6.1 were calculated using $(Ba_{1-x}Zn_x)Al_2O_4:Eu^{2+};Nd^{3+}$ with $x = 1$ phosphor powder. The average crystal size for the phosphor powder was found to be 25 nm.

Table 6.1: Calculated average crystal size for $(Ba_{1-x}Zn_x)Al_2O_4:Eu^{2+};Nd^{3+}$ (x=1) phosphor powder

Peak	2θ (degrees)	FWHM (β)	D (nm)
[311]	36.858	0.33346	25
[220]	31.293	0.32383	26
[511]	59.392	0.35990	25
[440]	65.277	0.39469	24

D(average) = 25 nm

XRD for the $(Ba_{1-x}Zn_x)Al_2O_4:Eu^{2+};Nd^{3+}$ with the compositions $x = 0.2, 0.4, 0.5, 0.6$ and 0.8 shows the mixed composition of the two $Ba(NO_3)_2$ and $ZnAl_2O_4$ structures. $BaAl_2O_4$ phase can be formed by increasing the temperature. Figure 6.3 shows the X-ray diffraction pattern of $(Ba_{1-x}Zn_x)Al_2O_4:Eu^{2+};Nd^{3+}$ with the composition of $x = 0$ annealed at $800^{\circ}C$ for 3 hours. This spectrum shows the hexagonal structure of $BaAl_2O_4$ according to the JCPDS 17-0306. This is in agreement with the report of Stefani et al [5]. The average crystal size calculated from the (202), (200), (220), and (222) planes of the annealed $(Ba_{1-x}Zn_x)Al_2O_4:Eu^{2+};Nd^{3+}$ XRD pattern with the composition of $x = 0$ was found to be 51 nm.
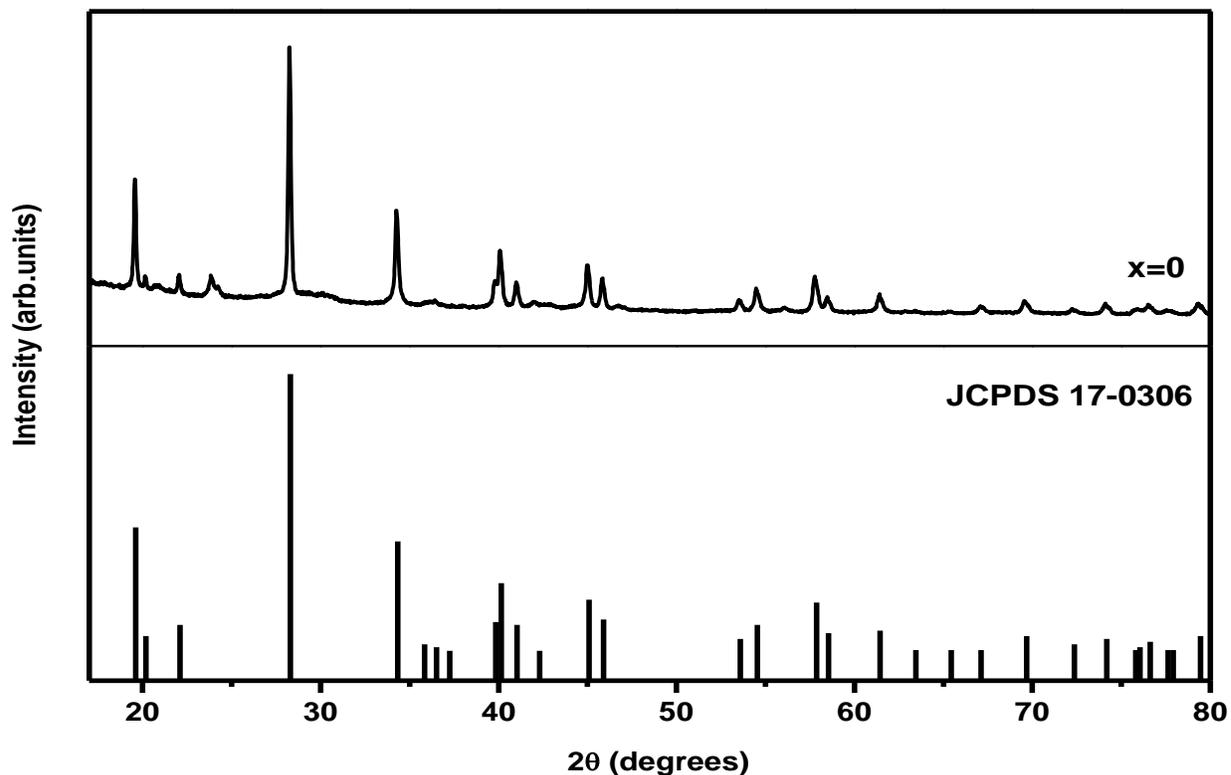
Figure 6.3: XRD patterns of $(Ba_{1-x}Zn_x)Al_2O_4:Eu^{2+};Nd^{3+}$ with the composition of x = 0 annealed at 800^oC for 3 hours.

SEM images of $(Ba_{1-x}Zn_x)Al_2O_4:Eu^{2+};Nd^{3+}$ prepared at an initiating temperature of 500^oC with the compositions x = 0, 0.5 and 1 are shown in figure 6.4. The SEM images were taken at high magnification using the high resolution SEM. The morphology shown in figure 6.3 (a) clearly shows the irregular plate-like particles of $(Ba_{1-x}Zn_x)Al_2O_4:Eu^{2+};Nd^{3+}$ (x = 0). Figure 6.3 (b) shows the nano-rods with a small percentage of nanoparticles and figure 6.3 (c) shows the spheroidal particles of $(Ba_{1-x}Zn_x)Al_2O_4:Eu^{2+};Nd^{3+}$ (x = 1). Different morphologies found in these phosphors are due to difference in Ba and Zn concentrations.
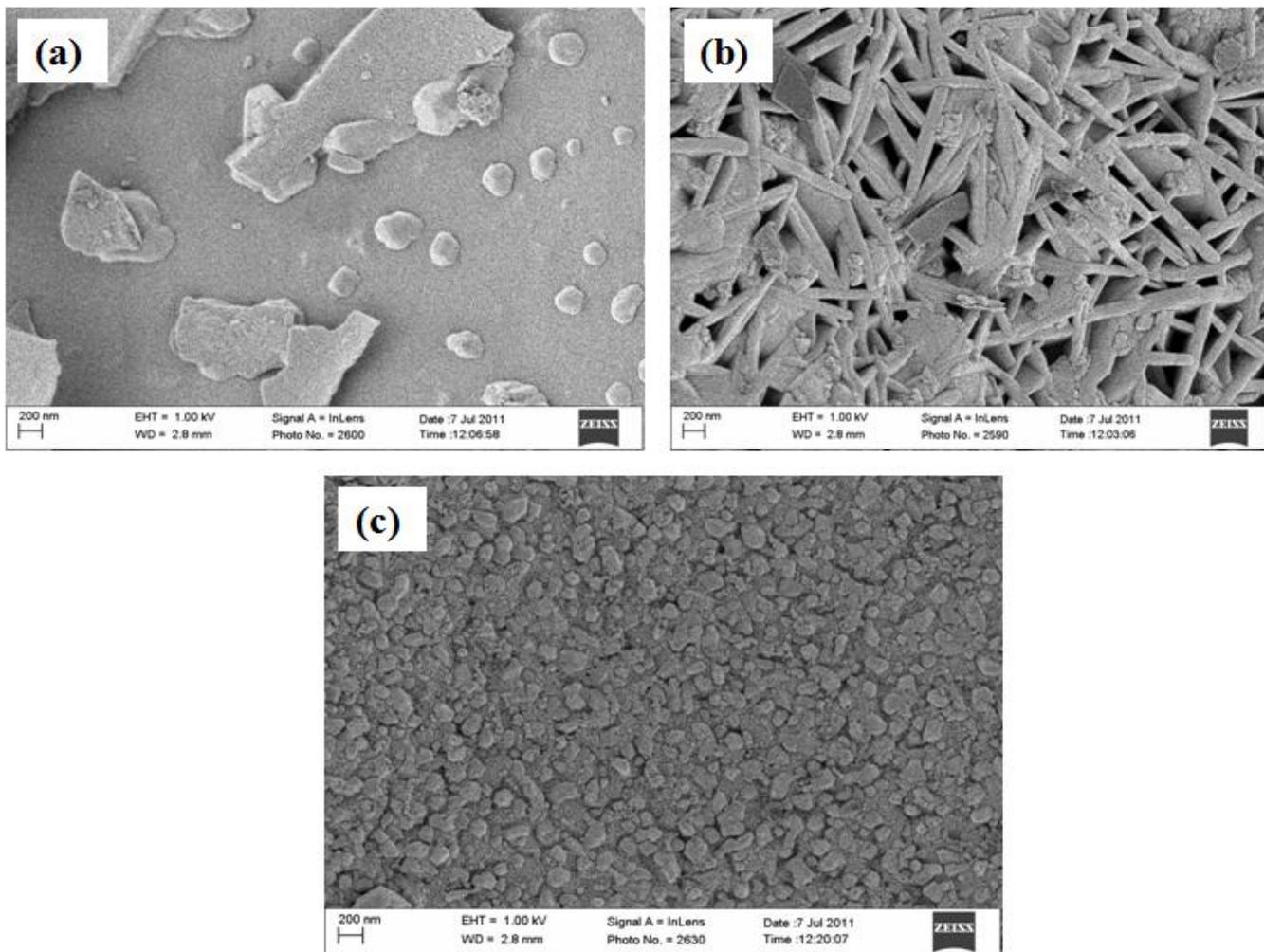
Figure 6.4: High magnification SEM images of $(Ba_{1-x}Zn_x)Al_2O_4:Eu^{2+};Nd^{3+}$ prepared at an initiating temperature of 500^oC with the compositions, (a) x = 0 (b) x = 0.5 and (c) x = 1.

6.3.2: Luminescence and decay studies

Figure 6.5 (a) shows the PL emission spectra of the $(Ba_{1-x}Zn_x)Al_2O_4:Eu^{2+};Nd^{3+}$ phosphor powder with composition x = 0, 0.2, 0.5, 0.6 and 1 prepared at the initiating temperature of 500^oC. All the samples were excited by a 325 nm He-Cd laser at room temperature. The emission of the phosphor powders has the peak at 527 nm, 501 nm, 452 nm and 450 nm, for the compositions x = 0, 0.2, 0.5 and 0.6, respectively. It was reported that broad emission bands from these spectra

are attributed to the typical transitions from the lowest ^2D level of the excited $4f^65d^1$ configuration to the ground $^8S_{7/2}$ level of the $4f^7$ configuration of Eu^{2+} ion [6].
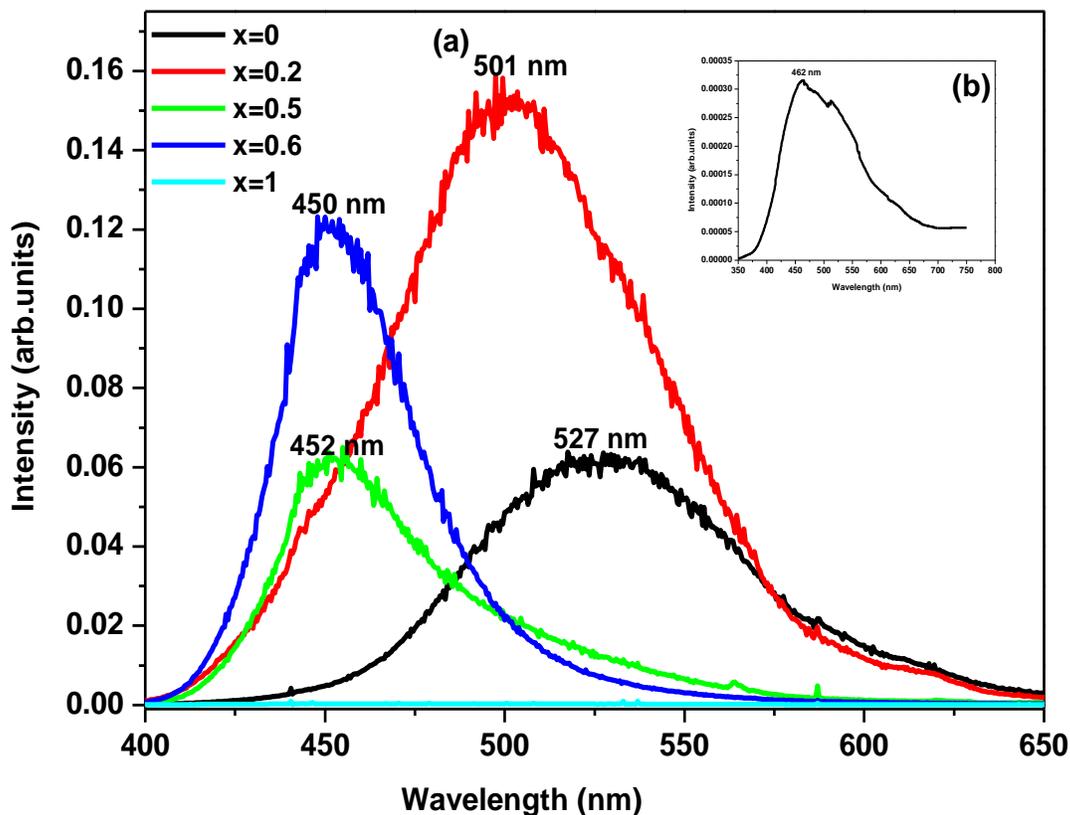
Figure 6.5 (a): PL spectra of $(Ba_{1-x}Zn_x)Al_2O_4:Eu^{2+};Nd^{3+}$ with the composition x = 0, 0.2, 0.5, 0.6 and 1) prepared at an initiating temperature of 500^oC (b) Inset is the PL spectrum of $(Ba_{1-x}Zn_x)Al_2O_4:Eu^{2+};Nd^{3+}$ at x = 1.

Jung et al. [1], reported that the emission of Eu^{2+} is highly dependent on the crystal strength. So the addition of Zn in $BaAl_2O_4$ can change the surroundings of Eu^{2+} and the crystal structure. Then this result to the different emission sites in the material. The highest PL emission intensity was observed for $(Ba_{1-x}Zn_x)Al_2O_4:Eu^{2+};Nd^{3+}$ with x = 0.2. The phosphor powder with the composition x = 1 showed the lowest PL intensity and the spectrum is shown in the inset of figure 6.5 (b).

The decay data were recorded when the powders were excite with a monochromatized Xenon lamp at an excitation of 325 nm. The decay curve of $(Ba_{1-x}Zn_x)Al_2O_4:Eu^{2+};Nd^{3+}$ phosphor powders with the composition of x = 0.2 prepared at an initiating temperature of 500^oC are shown in figure 6.6. The inset (figure 6.5 (b)) shows the decay curves of $Ba_{1-x}Zn_x)Al_2O_4:Eu^{2+};Nd^{3+}$ powders with the compositions x = 0, x = 0.5 and x = 1.
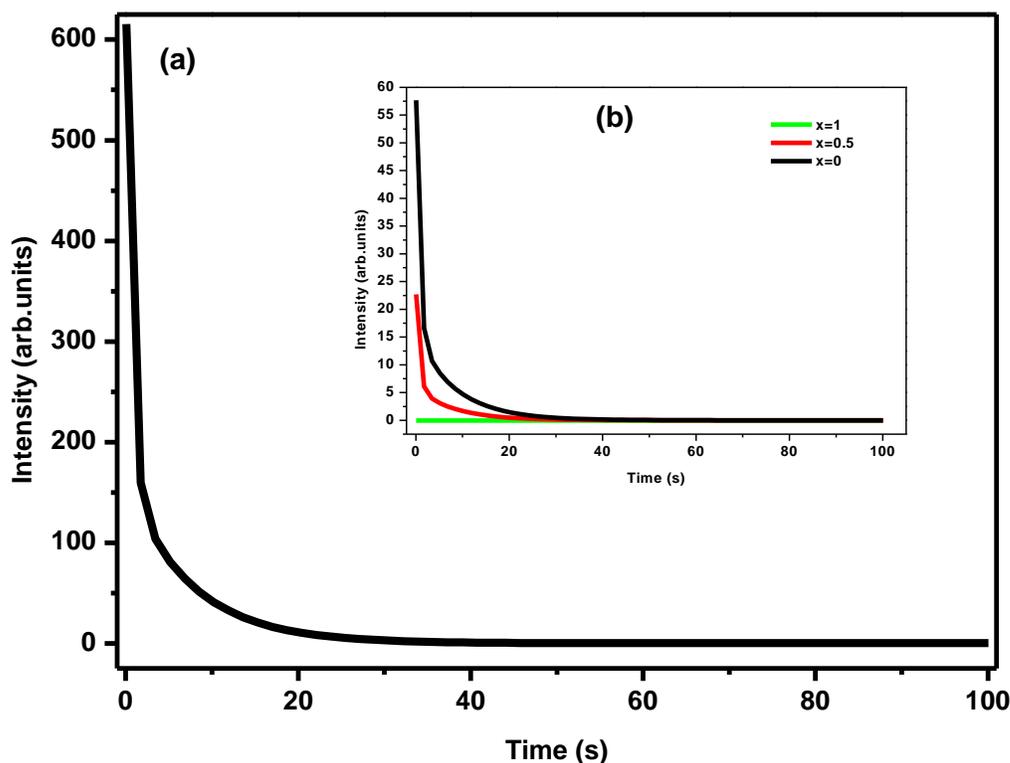
Figure 6.6: (a) Decay curve of $(Ba_{1-x}Zn_x)Al_2O_4:Eu^{2+};Nd^{3+}$ with composition x = 0.2 ,(b) Insert showing the decay curves of $(Ba_{1-x}Zn_x)Al_2O_4:Eu^{2+};Nd^{3+}$ with compositions x = 0, 0.5, and 1 prepared at an initiating temperature of 500^oC.

The long afterglow was observed for the powder with the composition of x = 0.2 compared to other phosphor powders. It has been reported that co-doping with rare earths can increase the persistence of the phosphor. In this case incorporation of the Nd^{3+} ions generates traps in the energy band gap of the host material and this traps act as hole trapping centres near the valence

band and which they can lead to long persistence after the excitation source is switched off [7]. All the phosphor powders were fitted using the second order exponential and the parameters for the fitting data are listed in table 6.2.

Table 6.2: Decay fitting parameters of the phosphor powder

Composition of $(Ba_{1-x}Zn_x)Al_2O_4:Eu^{2+};Nd^{3+}$	Decay constants	
	τ_1 (sec)	τ_2 (sec)
x = 0	0.72 ± 0.01	8.47 ± 1.0
x = 0.2	0.79 ± 0.01	9.44 ± 1.0
x = 0.5	0.67 ± 0.01	8.00 ± 1.0

The equation used for the fitting is as follows:

$$I = A_1 exp\left(-\frac{t}{\tau_1}\right) + A_2 exp\left(-\frac{t}{\tau_2}\right) \qquad (1)$$

where I is the phosphorescence intensity at any time t after switching off the excitation illumination; A_1 and A_2 are constants and τ_1 and τ_2 are decay times for the exponential components respectively [8].

6.4: Conclusion

The phosphor powders of $(Ba_{1-x}Zn_x)Al_2O_4:Eu^{2+};Nd^{3+}$ with compositions of x = 0, 0.2, 0.4, 0.5, 0.6, 0.8 and 1 were successfully synthesized by combustion method at an initiating temperature of 500^oC and were annealed at 800^oC. The X-ray diffraction shows the cubic structures for the compositions of x = 0 and x = 1 at an initiating temperature of 500^oC. After annealing at 800^oC the structure changes to hexagonal for x = 0 composition. The SEM images of the phosphor samples show different kinds of morphologies for the compositions x = 0, 0.5 and 1. The PL emission of the phosphor powder clearly showed a shift from green to blue regions. The highest PL emission and the long afterglow ascribed to trapping and detrapping of charge carriers were observed from $(Ba_{1-x}Zn_x)Al_2O_4:Eu^{2+};Nd^{3+}$ with x = 0.2.

References

[1] K.Y. Jung, H.W. Lee and H. Jung, Chemistry of Materials **18** 2249-2255 (2006)

[2] B.S. Barros, P.S. Melo, R.H.G.A. Kiminami, A.C.F.M. Costa, G.F. de Sa and S. Alves, Journal of Material Science **41** 4744-4748 (2006)

[3] X.Y. Chen, C. Ma, S.P. Bao and Z. Li, Journal of Colloid and Interface Science **346** 8-11 (2010)

[4] B.D. Cullity, Element of x-ray diffraction (2nd edition) p284 (1978)

[5] R. Sefani, L.V.C Rodrigues, C.A.A Carvalho, M.C.F.C Felinto, H.F Brito, M. Lastusaari and J. Holsa, Optical Materials **31** 1815-1818 (2009)

[6] H. Ryu, B.K. Singh and K.S. Bartwal, Physica B **403** 126-130 (2008)

[7] H. Ryu, B.K. Singh and K.S. Bartwal, Journal of Korean Ceramic Society **45** 3 146-149 (2008)

[8] N. Lakshminarasimhan and and U.V. Varadaraju, Materials Research Bulletin **43** 2946-2953 (2008)

CHAPTER 7

Summary and conclusions

Thesis conclusion

Different phosphor powders were successfully synthesized using combustion method. This preparation method was found to be more efficient because the phosphors of high efficiency were obtained at temperatures as low as 500^oC-600^oC in a very short period of time (5 min). Different techniques were used to study the structure, elemental compositions, morphology and the stretching mode frequencies of the phosphor powders. Thermoluminescence, photoluminescence and decay studies were also investigated. The techniques that were used are X-ray diffraction (XRD), scanning electron microcopy (SEM), X-ray energy dispersive spectroscopy (EDS), X-ray Photoelectron Spectroscopy (XPS) and Fourier Transform Infrared Spectroscopy (FT-IR), 325nm He-Cd laser and Varian Cary Eclipse Fluorescence Spectrophotometer coupled with a monochromatized Xenon lamp.

The phosphor powders of $Ba_{0.96}Al_2O_4$:$Eu^{2+}_{0.02}$; $RE_{0.02}$ ($RE = Dy^{3+}$, Nd^{3+}, Gd^{3+}, Sm^{3+}, Ce^{3+}, Er^{3+}, Pr^{3+} and Tb^{3+}) were successfully synthesized using the combustion method at an initiating temperature of 600^oC and were annealed at 1000^oC. The XRD results showed that the small amount of doped rare earth ions have no effects on the phase structure. Post-preparation annealing did not affect the general properties of the phosphors. The blueish-green emission associated with the $4f^65d^1$-$4f^7$ transitions Eu^{2+} was observed at ~ 504 nm from all the samples with the maximum emission observed from the sample co-doped with Er^{3+}. The long afterglow ascribed to trapping and detrapping of charge carriers was observed from Dy^{3+} and Nd^{3+}. The traps of the Nd^{3+} co-doped sample, which exhibited relatively longer afterglow, follow a quasi-continuous distribution as observed from TL glow curves.

The phosphor powders $BaAl_2O_4:Eu^{2+};Nd^{3+};Gd^{3+}$ were successfully prepared at different initiating temperatures of 400^oC-1200^oC. The X-ray diffraction spectra show the hexagonal structure of $BaAl_2O_4$ at a temperature range of 500^oC-1200^oC. SEM studies showed different particle morphologies with the increase in temperature. The broad blue-green emission was observed at 502 nm. This emission can be attributed to the $4f^65d^1$-$4f^7$ transitions of the Eu^{2+} ions. The phosphorescence decay curves were obtained by irradiating the samples with a 365 nm UV light. The samples prepared at 600^oC and 1200^oC show the main TL glow peaks at around 72^oC. These bands are at a similar position which suggests that the traps responsible for these bands are similar. The rate of decay seems to be faster in phosphor sample prepared at 600^oC than the ones prepared at 1200^oC. The trapping and detrapping of charge carriers accounted for the long afterglow properties of the phosphors. The long afterglow observed from these phosphors can be attributed to the traps created by co-doping with Nd^{3+} and Gd^{3+} ions.

The phosphor samples of $(Ba_{1-x}Sr_x)Al_2O_4:Eu^{2+};Nd^{3+}$ with the composition (x = 0, 0.4, 0.5, 0.6 and 1) were synthesized at an initiating temperature of 500^oC. The X-ray diffraction patterns shows that hexagonal structure of $BaAl_2O_4$ and monoclinic structure of $SrAl_2O_4$ at the compositions x = 0 and x = 1 respectively. SEM investigations showed the change in surface morphology for different compositions. The blue-green to bright-green emission was observed in the emission spectra when different ratios of Ba^{2+} to Sr^{2+} were used. The emission intensity was high for the composition of x = 0. The long persistence was observed from $(Ba_{1-x}Sr_x)Al_2O_4:Eu^{2+};Nd^{3+}$ with the composition x = 0.

The phosphor powders of $(Ba_{1-x}Zn_x)Al_2O_4:Eu^{2+};Nd^{3+}$ with compositions (x = 0, 0.2, 0.4, 0.5, 0.6, 0.8 and 1.0) were synthesized at an initiating temperature of 500^oC and were annealed at 800^oC for 3 hrs. The X-ray diffraction shows the cubic structure for the compositions of x = 0 and x = 1, respectively at an initiating temperature of 500^oC. After annealing at 800^oC the structure changes to hexagonal for x = 0 composition. The morphology of the phosphor samples showed different kinds of structure for the compositions x = 0, 0.5 and 1, irregular plate like structures, nano-rods with a small percentage of nanoparticles and spheroidal particles, respectively. The highest PL emission and the long afterglow ascribed to trapping and detrapping of charge carriers were observed from $(Ba_{1-x}Zn_x)Al_2O_4:Eu^{2+};Nd^{3+}$ with x = 0.2.

Publications

- M.A. Lephoto, O.M. Ntwaeaborwa, Shreyas S. Pitale, H.C. Swart, J.R. Botha, B.M. Mothudi, Synthesis and Characterization of $BaAl_2O_4:Eu^{2+}$ co-doped with different rare earth ions, Accepted (2011) & Published by Elsevier B.V. doi:10.1016/j.physb.2011.09.096

- B.M. Mothudi , M.A. Lephoto , O.M. Ntwaeaborwa, J.R. Botha, H.C. Swart, Thermoluminescent and stuctural properties of $BaAl_2O_4:Eu^{2+},Nd^{3+},Gd^{3+}$ phosphors prepared by combustion method, Accepted (2011) & Published by Elsevier B.V. doi:10.1016/j.physb.2011.09.100

Conferences

- M.A. Lephoto, O.M. Ntwaeaborwa, Shreyas S. Pitale, H.C. Swart, J.R. Botha, B.M. Mothudi, Synthesis and Characterization of $BaAl_2O_4:Eu^{2+}$ co-doped with different rare earth ions
4th South African Conference on Photonic Material, hosted by UFS, Kariega Game Reserve, 2 – 6 May 2011

- M.A Lephoto, O.M Ntwaeaborwa, H.C Swart, B.M Mothudi, Synthesis and photoluminescence studies of $(Ba_{1-x}Sr_x)Al_2O_4: Eu^{2+}; Nd^{3+}$ prepared by combustion method
56th Annual Conference of the South African Institute of Physics (SAIP), hosted by UNISA, St Georges Hotel and Convention Centre, Pretoria, 12 – 15 July 2011